2016

Polarization Charge Density in Strained Graphene

Noah Wilson
University of Vermont

Polarization Charge Density in Strained Graphene

A Thesis Presented

by

Noah Wilson

to

The Faculty of the Graduate College

of

The University of Vermont

In Partial Fulfillment of the Requirements
for the Degree of Master of Science
Specializing in Physics
May, 2016

Defense Date: March 21, 2016
Thesis Examinatrion Committee:

Valeri Kotov, Ph.D., Advisor
Frederic Sansoz, Ph.D., Chairperson
Adrian Del Maestro, Ph.D.
Cynthia J. Forehand, Ph.D., Dean of the Graduate College

Abstract

Graphene, the world's first truly two-dimensional material, is unique for having an electronic structure described by an effective Lorentz invariant theory. One important consequence is that the ratio or Coulomb energy to kinetic energy is a constant, depending only on conditions within the lattice rather than on the average charge density as in a typical Galilean invariant material. Given this unusual property, a natural question would be how do phenomena, such as screening of a Coulomb impurity, happen in graphene? Moreover, how does the addition of uniaxial strain enhance or diminish this behavior? Here I discuss our work to calculate the charge density distribution in a lattice of strained graphene under the effect of an external Coulomb impurity.

Graphene can have its band structure significantly altered by the application of uniaxial strain. Two cases are here explored: relatively weak strain at some finite chemical potential, and extreme strain with zero chemical potential. In the first system, the strain induces elliptic Dirac cones, engendering some inherent directionality to graphene's electronic properties that did not exist before. This anisotropy manifests itself in the polarization function, and so too in the screening charge density. A finite chemical potential in this case is necessary for any screening to take place in graphene since, without it, there are no electron states near the Fermi level to polarize. Both in the strained and unstrained case, decaying oscillations known as Friedel oscillations are observed. The result of strain is a multifaceted anisotropy of the charge distribution: the amplitude, frequency, and the position of the first peak in the oscillations are each varied depending on the direction one observes.

In the second system, extreme strain in graphene leads to a merging of Dirac cones, yielding a transition to a new energy spectrum. This band structure is unusual in that it becomes quadratic along the direction of strain while remaining linear along the perpendicular. We evaluate the screening response to a Coulomb impurity in this case at zero chemical potential, and yet long-range distribution tails are still observed. The result is a very exotic charge distribution, in which the radial distribution of charge and the angular distribution are highly coupled, and at various distances, both screening and anti-screening regions are observed around the impurity. The anti-screening regions are local, and the net induced charge density still satisfies the accepted model of screening.

Acknowledgements

I have come to understand that graduate school is nothing if it does not challenge you. Anyone can pick up a textbook and learn what they want how they would like, but it takes people to push awareness to understanding. Of all the people I have had the pleasure to work with, none has challenged me more than my advisor Professor Valeri Kotov, who managed to hold me to a high standard, while also being an unfailingly encouraging teacher of not only how to do physics right, but how to do it well.

Professor Dennis Clougherty, the classes I have taken with you has convinced me even further that physics is an art; there is a poetry to mathematics, and few professors show that as well as you. Professor Adrian Del Maestro, I have never had a professor who could teach physics with such meticulousness and detail without sacrificing intuitiveness. Dr. Luke Donforth, studying theory, it can sometimes be difficult to remember that physics is still something that actually happens in the world around us, and I feel you have helped me remember that.

And thank you to everyone else who have helped me during my studies here: Ben, Nathan, Owen, Lane, and many others, thank you for never leaving me without help when I needed it.

Contents

List of Figures

Chapter 1

Introduction

1.1 A Brief Overview of Graphene

Among the pantheon of applicable materials in the course of human history there are a few which have played a hand in shaping that course. In many ways progress has been measured by the use of materials: stone, bronze, iron, steel; ages of mankind's existence named not for what societies were built, but for what they were built *with*. The world can be mastered by mastering the stuff it is made of. The sophistication and prolificacy of modern material use is staggering. Simple, common, materials used for centuries can be found to have remarkable properties and set to applications never before conceived. An excellent example is graphite; found during 16th century England to be an effective lubricant and was used to line cannon ball molds (as well as marking sheep). Today graphite is still used as, among other things, an industrial lubricant, a common writing implement, a key component of many batteries, and a moderator for nuclear reactors. That last use made graphite of keen scientific interest during the mid-20th century.

In 1947 Canadian physicist Phillip Russel Wallace published a paper on the electronic band structure of graphite[1]. In the process of doing so he relied on calculating the band structure of a single sheet of graphite, coined a century or so earlier as graphene. At the time this was a theoretical tool, a way to simplify and understand the structure of graphite; isolated graphene was thought impossible, and

so generated little further study for nearly sixty years. In 2004, Dr. Andre Geim and Dr. Konstantin Novoselov at the University of Manchester managed to create sheets of graphene using a method of "mechanical exfoliation" or the "Scotch-tape method", for which they won the Nobel Prize in 2010[2]. Several properties of graphene had previously been opined by a number of theorists, but with this advancement it could now be studied experimentally.

Graphene was the first in what is now a class of truly two-dimensional materials; materials whose properites can be fully described without invoking a third dimension. Pragmatically, these are stable materials of single-atom thickness, and so can be used with virtually no cost of space. In the case of graphene, this is far from a limitation. In spite of being one of the thinnest materials ever, it is also one of the strongest, most conductive and least brittle[3]. It boasts a tensile strength much greater than steel, conductivity dwarfing that of copper, and can maintain these properties even while being deformed through strain or torsion. Such properties make graphene something of a "wonder drug" in material science.

One square-meter of graphene has a mass of about 0.77 mg, and could support a roughly 4 kg load without breaking. That kind of specific strength, coupled with its flexibility, is not seen in any other materials, and could make graphene a critical component of anything that must be strong and light such as future air and spacecraft. That same flexibility with an electron mobility ten times that of copper and an opacity of 2.3 % makes graphene an ideal candidate for such technologies as flexible display screens. Other possible applications of graphene are as wide-ranging as supercapacitors and targeted cancer treatment. Before graphene can be mass produced and seriously set to all of these various purposes its myriad properties must be understood, and the basis for understanding the properties of any material lie in understanding the behavior of electrons within it.

1.2 Crystal Structure of Graphene

Graphene is made of carbon. Carbon has six electrons, so in their ground state they comprise the $1s^2 2s^2 2p^2$ energy levels. When a carbon atom forms a covalent bond with another atom, say another carbon atom, or hydrogen or oxygen, the gain in energy is greater than the 4 eV difference in energy between the 2s and 2p levels. So when bonded to another carbon atom, this excited state becomes $1s^2 2s^1 2p^3$, now still with four electrons in the valence shell, but now one in the s-orbital, and three in the p-orbital, one for each axis.

With one electron in each of four energy states, $|2s\rangle$, $|2p_x\rangle$, $|2p_y\rangle$, and $|2p_z\rangle$, there can be a superposition between these states. In particular, a superposition of the $|2s\rangle$ state with one or more of the $|2p\rangle$ states results in sp-hybridization. One possible case is sp^2-hybridization, meaning that the $|2s\rangle$ state hybridizes with two of the $|2p\rangle$ states, typically chosen to be the $|2p_x\rangle$ and $|2p_y\rangle$ states. The result of sp^2-hybridization is three hybridized orbitals separated by 120° oriented in the x-y plane, and an unbonded p-orbital extending out of the plane.

A very common example of sp^2-hybridization in carbon is benzene, a hexagonal ring of carbon atoms where the third hybridized orbital bonds each carbon atom to an atom of hydrogen. The hybridized orbitals form three σ-bonds, and the extra p-orbital forms a single π-bond between each carbon atom and one other atom in the ring. This fact would seem to imply an inequity in the atomic spacing between carbon atoms, that the atoms connected by a σ-bond would have a larger spacing than the π-bonded atoms. This, however, is not the case. Instead the carbon atoms in benzene have exactly the same spacing: a fact explained by Linus Pauling's concept of resonance[4], as a superposition of arrangements in the π-bonds, making them delocalized, having no preferred arrangement. Instead the π-bonds can be thought to delocalize or "smear" across the ring. Graphene is essentially a sheet of benzene rings where each carbon atom is bonded to one of the vertices of another ring, and

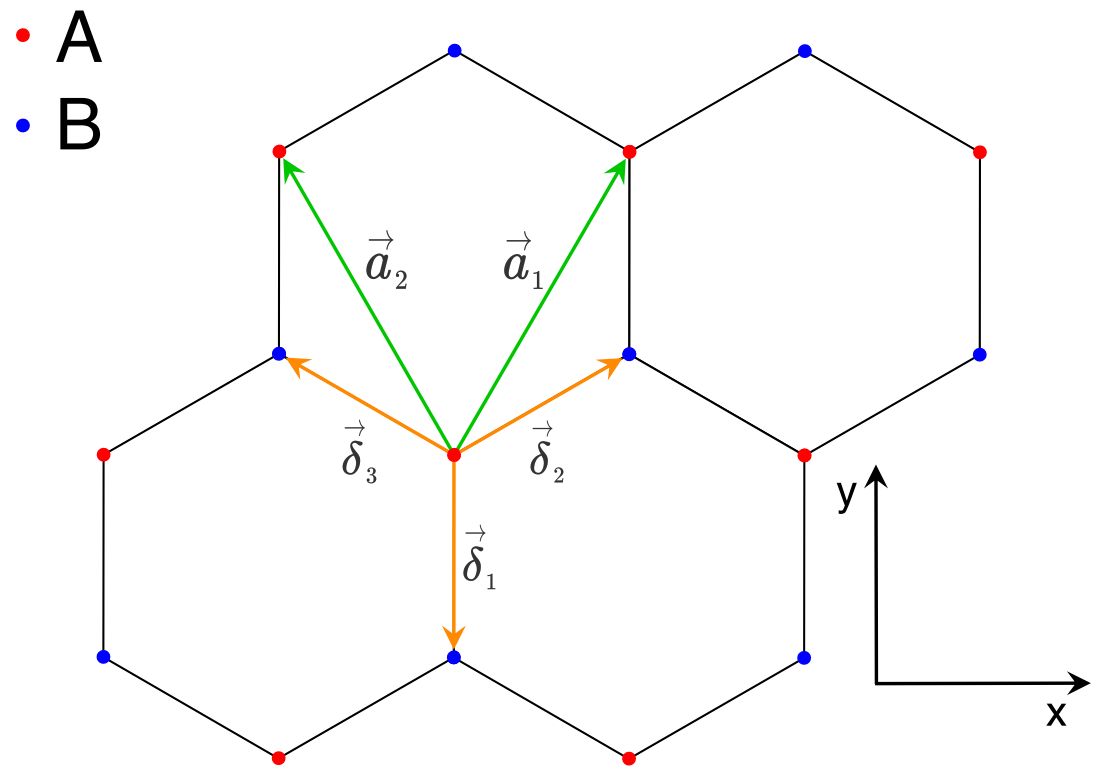

Figure 1.1: Graphene's honeycomb lattice with the A sublattice sites labeled in red, and the B sublattice sides labeled in blue. The NNN lattice vectors $\boldsymbol{a}_1$ and $\boldsymbol{a}_2$ are labeled in green, and the NN lattice vectors $\boldsymbol{\delta}_i$ labeled in orange. The y-direction points along the crystallographic armchair direction, while the x-direction points along the zig-zag direction. The distance between NN atoms, a, is 0.142 nm, and the distance between NNN atoms is $\sqrt{3}a$=0.24 nm.

so each atom in graphene has covalent σ-bonds with three other carbon atoms. This structure gives graphene its characteristic honeycomb structure.

1.2.1 Real-Space Crystal Structure

Graphene's honeycomb structure is shown in Fig. 1.1. The honeycomb lattice is not a Bravais lattice; it is instead two separate, overlapping hexagonal, or triangular, Bravais lattices labeled the A sublattice and the B sublattice. Graphene, by its structure, is inherently anisotropic centered around each atom. There are thus two inequivalent directions in the lattice designated armchair and zig-zag, so named

because of the pattern atoms along those directions form when connected by straight lines. The armchair and zig-zag directions are defined along the y and x directions respectively for the purposes of calculations. Lattice vectors $\boldsymbol{a}_1$ and $\boldsymbol{a}_2$ connect atoms within the same sublattice, which are next-nearest-neighbor (NNN) atoms. Vectors $\boldsymbol{\delta}_i$ where $i = 1, 2, 3$ connect atoms of the A sublattice to their nearest-neighbor (NN) atoms of the B sublattice. The NNN lattice vectors (which will be henceforth referred to simply as the lattice vectors) are given by

$$\boldsymbol{a}_1 = \frac{\sqrt{3}a}{2}(\hat{x} + \sqrt{3}\hat{y}), \qquad \boldsymbol{a}_2 = \frac{\sqrt{3}a}{2}(-\hat{x} + \sqrt{3}\hat{y}), \tag{1.1}$$

where a is the lattice spacing equal to, in graphene, 0.142 nm, however the modulus of these lattice vectors is equal to $\sqrt{3}a$. The NN lattice vectors are

$$\boldsymbol{\delta}_1 = -a\hat{y}, \qquad \boldsymbol{\delta}_2 = \frac{a}{2}(\sqrt{3}\hat{x} + \hat{y}), \qquad \boldsymbol{\delta}_3 = \frac{a}{2}(-\sqrt{3}\hat{x} + \hat{y}). \tag{1.2}$$

There is, of course, a degree of arbitrariness to the way these vectors were defined, in particular there are many equivalent choices of the lattice vectors. Vector $\boldsymbol{a}_2$, for example could have been defined along the x-axis to be $\sqrt{3}a\hat{x}$. In some cases such a vector is considered to be in fact a third lattice vector, $\boldsymbol{a}_3$, and will be, at one point in the derivation of graphene's electronic band structure, referred to. This will become apparent as with the inclusion of this third vector, every NNN atom within a sublattice can be connected by these three vectors and their negatives. A third lattice vector is, however, unnecessary in the construction of the Bravais lattice, and the vectors mirrored across the y-axis have been somewhat arbitrarily chosen as the basis vectors for the lattice. Of equal importance to understanding the electronic structure of graphene is the reciprocal lattice structure, in particular the first Brillouin

zone (1st BZ) shown in Fig. 1.2.

1.2.2 Reciprocal Space and the First Brillouin zone

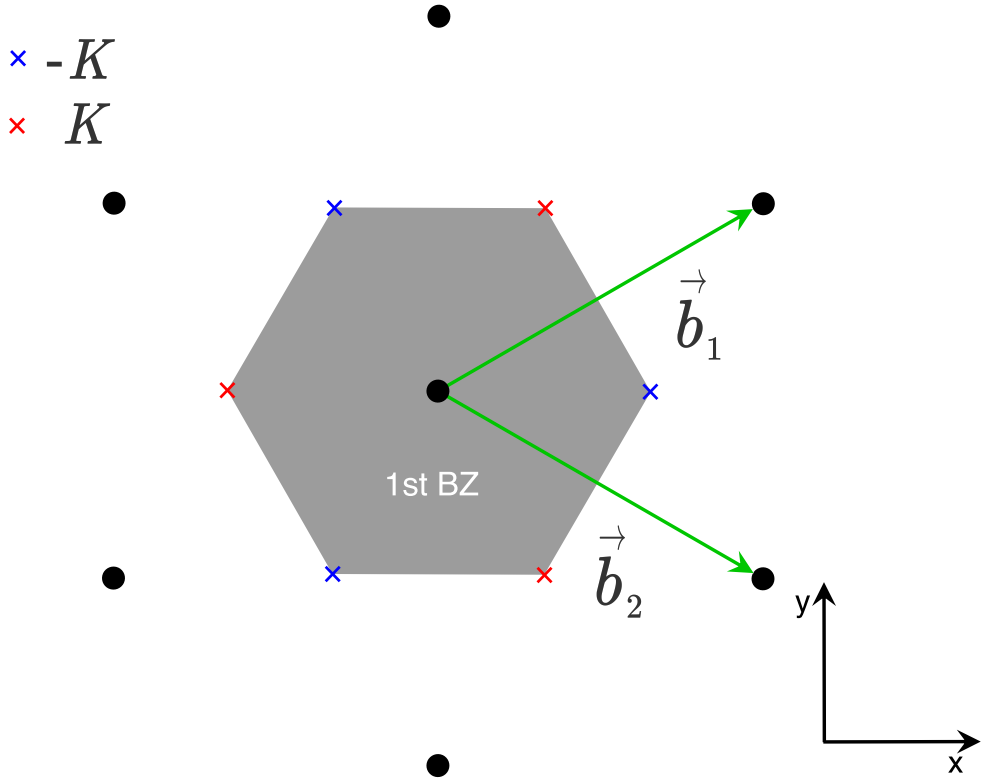

Figure 1.2: The reciprocal lattice of graphene. The black dots are the reciprocal lattice points, with reciprocal lattice vectors $\boldsymbol{b}_1$ and $\boldsymbol{b}_2$ corresponding to the real-space lattice vectors labeled in green. The x and y directions have not been changed from the real space picture. The first Brillouin zone (1st BZ) is shaded in gray. The red and blue "x"s correspond to the two inequivalent corners of the 1st BZ, K and $-K$.

Graphene's reciprocal lattice is defined by the reciprocal lattice vectors

$$\boldsymbol{b}_1 = \frac{2\pi}{\sqrt{3}a}\left(\hat{x} + \frac{1}{\sqrt{3}}\hat{y}\right), \qquad \boldsymbol{b}_2 = \frac{2\pi}{\sqrt{3}a}\left(\hat{x} - \frac{1}{\sqrt{3}}\hat{y}\right), \tag{1.3}$$

where a is once again the real-space distance between NN atoms. The vectors in Eq.

1.3 are directly related to the vectors in Eq. 1.1 by the usual transformation [1] into recirpocal space. Since graphene is two-dimensional there is no $\hat{z}$ component in either $\boldsymbol{a}_1$ or $\boldsymbol{a}_2$, and so for the purposes of calculating the reciprocal space lattice vectors a third vector $\boldsymbol{a}_3$ is defined to be equal to $\hat{z}$.

The corners of the 1st BZ are denoted K and $-K$; these are two opposite and inequivalent corners of the 1st BZ. Their inequivalency is unrelated to the fact that there are two distinct sublattices in real-space. A simple application of geometry reveals the locations of K and $-K$

$$\pm\boldsymbol{K} = \pm\frac{4\pi}{3\sqrt{3}a}\hat{x}. \tag{1.4}$$

The choice of $\pm\boldsymbol{K}$ is similarly arbitrary to the choice of the real-space lattice vectors, but defining $\pm\boldsymbol{K}$ along the x-axis is a natural choice since, as will be shown in the next chapter, the sites of zero-energy excitation for electrons in the lattice happen to be at the same location as the corners of the 1st BZ. Knowing the crystal structure and lattice vectors of graphene is not only of interest for understanding the form of the system, but they become crucial when calculating the electronic band structure.

1.3 A Look Ahead

With a firm understanding of the basic structure and properties of graphene's honeycomb lattice, discussing the specific electronic properties of graphene is now possible. The next chapter will comprise a thorough derivation of graphene's band structure, which takes the form of what are called Dirac cones. This will be followed by an overview of the how electrons screen an external impurity charge in metals. Here will be introduced the Lindhard response function, and the polarization charge density, $n(\boldsymbol{r})$. After doing so, $n(\boldsymbol{r})$ will be calculated in two separate cases: relatively

[1] $\boldsymbol{b}_i = 2\pi\frac{\boldsymbol{a}_j\times\boldsymbol{a}_k}{\boldsymbol{a}_i\cdot(\boldsymbol{a}_j\times\boldsymbol{a}_k)}$ where $\{i,j,k\}$ is some even permutation of {1,2,3}.

weak strain at some finite chemical potential, and extreme strain at zero chemical potential.

In the first case, $n(\boldsymbol{r})$ will exhibit a phenomenon known as Friedel oscillations. The origin of these oscillations will be explained with regard to the generic solution to the polarization response function. The response function will be solved for the specific case of strained graphene, and the integral necessary to calculate $n(\boldsymbol{r})$ will be simplified by the stationary phase approximation, and will otherwise be numerically evaluated. In the second case, extreme strain will mean a merging of Dirac cones resulting in an unique band structure, and $n(\boldsymbol{r})$ will be calculated for this case as well. Through this process the screening response of electrons within graphene undergoing deformation by various degrees of strain will be thoroughly explored.

Chapter 2

Graphene's Unstrained Electronic Band Structure

Graphene's band structure was originally derived by Wallace[1], and the discussion from the following chapter was compiled not only from his paper, but a variety of other sources[5, 6, 7, 8, 9]. As mentioned in Section 1.2, the π-bonds in benzene can be considered delocalized across the ring, and since graphene is essentially a sheet of benzene rings, these π-bonds are spread across the entire sheet. So of the four available electrons in carbon, three are used forming σ-bonds with other carbon atoms, and the fourth creates the π-bond. It is these π electrons that are responsible for the low-energy energy spectrum. At high energies, far beyond the Fermi-level, the σ electrons may also contribute to the electronic properties of graphene, but those will not be considered in either of the two cases being studied. Instead the band structure for π electrons will be calculated for low energies, which will be equivalent to remaining close to the corners of the 1st BZ, beginning from the basis of Bloch's theorem.

2.1 Bloch's Theorem

Bloch's theorem is a statement about solutions to the Schrödinger equation for periodic potentials. These solutions were originally proved by Felix Bloch, but the following discussion was taken primarily from books by Kittel[10], and Ashcroft and Mermin[11]. Graphene, being a crystal, has a periodic structure. This means that the by the potential, $V(\boldsymbol{r})$, is also periodic in the lattice, $V(\boldsymbol{r}) = V(\boldsymbol{r} + \boldsymbol{R})$, where $\boldsymbol{R}$ is a lattice vector defined as some linear combination of the basis vectors of the lattice. The Hamiltonian

$$\mathcal{H}(\boldsymbol{r}) = \frac{\hat{p}^2}{2m} + V(\boldsymbol{r}) \tag{2.1}$$

thus follows the same periodicity, $\mathcal{H}(\boldsymbol{r}) = \mathcal{H}(\boldsymbol{r} + \boldsymbol{R})$. Another way to put this is that the Hamiltonian is invariant under translation by a lattice vector defined by the translation operator $\mathcal{T}_{\boldsymbol{R}}$ defined to act on a function $f(\boldsymbol{r})$ as

$$\mathcal{T}_{\boldsymbol{R}} f(\boldsymbol{r}) = f(\boldsymbol{r} + \boldsymbol{R}). \tag{2.2}$$

Consider $\mathcal{T}_{\boldsymbol{R}}$ acting on the LHS of the energy eigenvalue equation, with an arbitrary wavefunction $\psi(\boldsymbol{r})$

$$\begin{aligned}
\mathcal{T}_{\boldsymbol{R}}\mathcal{H}(\boldsymbol{r})\psi(\boldsymbol{r}) &= \mathcal{H}(\boldsymbol{r} + \boldsymbol{R})\psi(\boldsymbol{r} + \boldsymbol{R}) \\
&= \mathcal{H}(\boldsymbol{r})\psi(\boldsymbol{r} + \boldsymbol{R}) \\
&= \mathcal{H}(\boldsymbol{r})\mathcal{T}_{\boldsymbol{R}}\psi(\boldsymbol{r}) \\
(\mathcal{T}_{\boldsymbol{R}}\mathcal{H} - \mathcal{H}\mathcal{T}_{\boldsymbol{R}})\psi &= 0 \\
\mathcal{T}_{\boldsymbol{R}}\mathcal{H} - \mathcal{H}\mathcal{T}_{\boldsymbol{R}} &= 0 \\
[\mathcal{T}_{\boldsymbol{R}}, \mathcal{H}] &= 0.
\end{aligned} \tag{2.3}$$

By this logic $\mathcal{T}_{\boldsymbol{R}}$ and $\mathcal{H}$ commute and thus share common eigenstates, $\psi(\boldsymbol{r})$, given that the Hamiltonian shares the periodicity of the lattice. This concept is at the heart of Bloch's theorem, and is quite powerful. For a lattice that is translationally invariant one does not need the specific form of the potential, aside from periodicity, in order to know something about the eigenstates for electrons in the lattice. Eigenvalues of $\mathcal{T}_{\boldsymbol{R}}$ satisfy

$$\mathcal{T}_{\boldsymbol{R}}\psi(\boldsymbol{r}) = \lambda\psi(\boldsymbol{r}), \tag{2.4}$$

where λ are eigenvalues of $\mathcal{T}_{\boldsymbol{R}}$. The generic wavefunction, $\psi(\boldsymbol{r})$, does depend on the specific form of the potential, however λ can be explicitly solved by first considering that $\psi(\boldsymbol{r})$ must satisfy the Born-Von Karman boundary condition, which states that for a wavefunction ϕ,

$$\varphi(\boldsymbol{r} + \boldsymbol{R}) = \varphi(\boldsymbol{r}) \tag{2.5}$$

assuming a periodic lattice with vectors $\boldsymbol{R}$. Imposing these boundary conditions together with Eq. 2.4 implies the solution

$$\begin{aligned} \psi(\boldsymbol{r}) &= \lambda\psi(\boldsymbol{r}) \\ \lambda &= 1 \\ \lambda &= e^{i2\pi}. \end{aligned} \tag{2.6}$$

This solution for λ is not as trivial as it may seem, since, for a reciprocal-space vector $\boldsymbol{k}$ corresponding to a real-space vector $\boldsymbol{r}$, it can be shown that $\boldsymbol{k}\cdot\boldsymbol{r} = 2\pi$. The Born-Von Karman condition applies in reciprocal space, with translations by the

reciprocal lattice vector $\boldsymbol{G}$ corresponding to $\boldsymbol{R}$[1], so

$$e^{i\boldsymbol{k}\cdot\boldsymbol{r}} = e^{i(\boldsymbol{k}+\boldsymbol{G})\cdot\boldsymbol{r}}, \tag{2.7}$$

which is only satisfied if $\boldsymbol{r}$ is restricted to be $\boldsymbol{R}$. Thus λ has plane-wave solutions

$$\lambda = e^{i\boldsymbol{k}\cdot\boldsymbol{R}}. \tag{2.8}$$

The reciprocal-space vector $\boldsymbol{k}$ is a real vector known as the wave-vector or quasi-momentum, and is an important quantity in the derivation of graphene's band structure since it will be, in essence, the primary variable in the energy spectrum. Recalling Eqs. 2.2 and 2.5 it can be observed that

$$\psi(\boldsymbol{r}) = e^{i\boldsymbol{k}\cdot\boldsymbol{R}}\psi(\boldsymbol{r}-\boldsymbol{R}). \tag{2.9}$$

Equation 2.9 is the formal statement of Bloch's theorem, which to be exact, assumes only a periodic potential, not necessarily a crystal lattice of atoms. Applying Bloch's theorem to such a lattice allows for more physical inferences to be made. First, the plane-waves are the translational piece of the wavefunction that essentially describes how a particular atom affects the energy eigenstates of electrons throughout the rest of the lattice. The missing piece to the picture is then the wavefunction of electrons within the atom itself, the atomic orbital wavefunction $\phi(\boldsymbol{r})$. So for a crystal lattice the Bloch functions can be written as the product of plane-waves and orbital wavefunctions summed over lattice vectors, so

$$\psi_{\boldsymbol{k}}(\boldsymbol{r}) = \sum_j e^{i\boldsymbol{k}\cdot\boldsymbol{R_j}}\phi(\boldsymbol{r}-\boldsymbol{R}_j), \tag{2.10}$$

where j denotes unique lattice vectors. One final change that must be made to Eq.

[1]Meaning for $\boldsymbol{R} = p\boldsymbol{a}_1 + q\boldsymbol{a}_2$, $\boldsymbol{G} = u\boldsymbol{b}_1 + v\boldsymbol{b}_2$, where $q, p, u, v \in \mathbb{Z}$.

2.10 is to consider more than one atom type in the crystal.

In graphene, Eq. 2.10 would apply well for either sublattice, but not for the honeycomb as a whole. The simplest way to do this would be to think of the total wavefunction as a linear combination of eigenstates for the A sublattice and B sublattice

$$\psi_{\boldsymbol{k}}(\boldsymbol{r}) = A_{\boldsymbol{k}}\psi^A_{\boldsymbol{k}}(\boldsymbol{r}) + B_{\boldsymbol{k}}\psi^B_{\boldsymbol{k}}(\boldsymbol{r}), \tag{2.11}$$

where $A_{\boldsymbol{k}}$ and $B_{\boldsymbol{k}}$ are constants. While graphene may have two nonequivalent sublattices, every atom is carbon, so $\phi(\boldsymbol{r})$ should not differ between them. In fact, the entire eigenstate of one sublattice can be related to another simply through translation by the NN lattice vector $\boldsymbol{\delta}$, so

$$\psi^A_{\boldsymbol{k}}(\boldsymbol{r}) = \psi^B_{\boldsymbol{k}}(\boldsymbol{r} + \boldsymbol{\delta}_i). \tag{2.12}$$

The choice of the index i in Eq. 2.12 is arbitrary and so will be omitted in the future. An atom on the A sublattice will be considered the central atom when deriving the band structure, and so the argument of ψ^A will never be translated by $\boldsymbol{\delta}$ while the argument of ψ^B always will be. The superscripts A and B are, thus, somewhat redundant when including a translation by $\boldsymbol{\delta}$, but they will be maintained throughout the derivation for the purpose of clarity. The Bloch wavefunction for either the A or B sublattice can now be written in the convenient form

$$\psi^{(n)}_{\boldsymbol{k}}(\boldsymbol{r}) = \sum_j e^{i\boldsymbol{k}\cdot\boldsymbol{R}_j}\phi^{(n)}(\boldsymbol{r} + \boldsymbol{\delta} - \boldsymbol{R}_j), \tag{2.13}$$

where the superscript (n) can be either A or B. Eq. 2.13 is the form of the wavefunction for graphene that will be used to derive the electronic band structure in the next section.

2.2 Derivation of Band Structure

Determining the electronic band structure of graphene is simply a matter of diagonalizing the Hamiltonian, Eq. 2.1. As stated in the previous section, the contribution of the σ-electrons to the electronic properties occurs only at higher energies, while the π-electrons dominate the low-energy electronic behavior. Since only the π-electron contributions are being considered, once the Hamiltonian has been diagonalized, the energy eigenvalues will be expanded at low energies, meaning small momenta, resulting in the previously mentioned Dirac cones. To simplify the resulting eigenvalue calculation, the eigenvalues will be calculated in the tight binding approximation.

2.2.1 The Characteristic Equation

Thus the tight biding approach, which treats the potential from other lattice sites only as small perturbations, seems reasonable. The tight binding Hamiltonian may be written

$$\mathcal{H} = \mathcal{H}_0 + \Delta V, \tag{2.14}$$

where $\mathcal{H}_0$ is the unperturbed Hamiltonian very close to an atomic site, and ΔV is the small perturbative potential from other atoms in the lattice. Beginning in some generic Hilbert space, the energy eigenvalue equation is

$$\mathcal{H} \left| \psi_{\boldsymbol{k}}^{(n)} \right\rangle = \epsilon_{\boldsymbol{k}} \left| \psi_{\boldsymbol{k}}^{(n)} \right\rangle, \tag{2.15}$$

The energy eigenvalues $\epsilon_{\boldsymbol{k}}$ are what must ultimately be solved for, and they have been giving the subscript $\boldsymbol{k}$ because the band structure will be a function of quasi-momentum in reciprocal space, and the superscript (n) once again denotes either an

atom in the either the A or B sublattice. Apply Eq. 2.14 to Eq. 2.15,

$$\begin{aligned}(\mathcal{H}_0 + \Delta V)\left|\psi_{\boldsymbol{k}}^{(n)}\right\rangle &= \epsilon_{\boldsymbol{k}}\left|\psi_{\boldsymbol{k}}^{(n)}\right\rangle \\ (\epsilon^{(n)} + \Delta V)\left|\psi_{\boldsymbol{k}}^{(n)}\right\rangle &= \epsilon_{\boldsymbol{k}}\left|\psi_{\boldsymbol{k}}^{(n)}\right\rangle \\ (\epsilon^{(n)} - \epsilon_{\boldsymbol{k}} + \Delta V)\left|\psi_{\boldsymbol{k}}^{(n)}\right\rangle &= 0,\end{aligned} \tag{2.16}$$

where $\epsilon^{(n)}$ is the eigenvalue of $\mathcal{H}_0$, and is, conceptually, the energy of the π-electron around its host atom at the central lattice site. Since all atoms have the same electron configuration (all being unionized carbon) this site energy is a constant for the entire lattice, and thus will only act as a shift in the energy spectrum. Not having any effect on the form of the band structure it will be neglected from this point forward. Acting on Eq. 2.16 from the left with $\left\langle\psi_{\boldsymbol{k}}^{(m)}\right|$, where (m), like (n), denotes either the A or B sublattice,

$$\begin{aligned}\left\langle\psi_{\boldsymbol{k}}^{(m)}\right|(\Delta V - \epsilon_{\boldsymbol{k}})\left|\psi_{\boldsymbol{k}}^{(m)}\right\rangle &= \left\langle\psi_{\boldsymbol{k}}^{(m)}\right|\Delta V\left|\psi_{\boldsymbol{k}}^{(m)}\right\rangle - \epsilon_{\boldsymbol{k}}\left\langle\psi_{\boldsymbol{k}}^{(m)}\middle|\psi_{\boldsymbol{k}}^{(m)}\right\rangle \\ \left\langle\psi_{\boldsymbol{k}}^{(m)}\right|(\Delta V - \epsilon_{\boldsymbol{k}})\left|\psi_{\boldsymbol{k}}^{(m)}\right\rangle &= t_{\boldsymbol{k}}^{mn} - \epsilon_{\boldsymbol{k}} s_{\boldsymbol{k}}^{mn},\end{aligned} \tag{2.17}$$

where elements of the hopping matrix, $t_{\boldsymbol{k}}^{mn}$ and the overlap matrix $s_{\boldsymbol{k}}^{mn}$ have been defined

$$\begin{aligned}t_{\boldsymbol{k}}^{mn} &= \left\langle\psi_{\boldsymbol{k}}^{(m)}\right|\Delta V\left|\psi_{\boldsymbol{k}}^{(m)}\right\rangle = \sum_j e^{i\boldsymbol{k}\cdot\boldsymbol{R}_j}\int d^2r\,\phi^{(m)*}(\boldsymbol{r}+\boldsymbol{\delta}-\boldsymbol{R}_j)\Delta V\phi^{(n)}(\boldsymbol{r}+\boldsymbol{\delta}-\boldsymbol{R}_j) \\ s_{\boldsymbol{k}}^{mn} &= \left\langle\psi_{\boldsymbol{k}}^{(m)}\middle|\psi_{\boldsymbol{k}}^{(m)}\right\rangle = \sum_j e^{i\boldsymbol{k}\cdot\boldsymbol{R}_j}\int d^2r\,\phi^{(m)*}(\boldsymbol{r}+\boldsymbol{\delta}-\boldsymbol{R}_j)\phi^{(n)}(\boldsymbol{r}+\boldsymbol{\delta}-\boldsymbol{R}_j).\end{aligned} \tag{2.18}$$

Referencing Eq. 2.16 with respect to Eq. 2.17, the values of $\epsilon_{\boldsymbol{k}}$ must satisfy the characteristic equation

$$\det\left[t_{\boldsymbol{k}} - \epsilon_{\boldsymbol{k}} s_{\boldsymbol{k}}\right] = 0. \tag{2.19}$$

To diagonalize the tight binding Hamiltonian its matrix elements must be determined. This can be done in the usual way

$$\mathcal{H}^{mn} = \left\langle \psi_{\boldsymbol{k}}^{(m)} \right| \mathcal{H} \left| \psi_{\boldsymbol{k}}^{(n)} \right\rangle \tag{2.20}$$

where now both (m) and (n) can denote either A or B separately. The matrix representation of $\mathcal{H}$ is

$$\mathcal{H} \doteq \begin{bmatrix} \left\langle \psi_{\boldsymbol{k}}^{A} \right| \mathcal{H} \left| \psi_{\boldsymbol{k}}^{A} \right\rangle & \left\langle \psi_{\boldsymbol{k}}^{A} \right| \mathcal{H} \left| \psi_{\boldsymbol{k}}^{B} \right\rangle \\ \left\langle \psi_{\boldsymbol{k}}^{B} \right| \mathcal{H} \left| \psi_{\boldsymbol{k}}^{A} \right\rangle & \left\langle \psi_{\boldsymbol{k}}^{B} \right| \mathcal{H} \left| \psi_{\boldsymbol{k}}^{B} \right\rangle \end{bmatrix}, \tag{2.21}$$

which should be an element-by-element match to the matrix elements of the wave function overlap between lattice sites

$$s_{\boldsymbol{k}} \doteq \begin{bmatrix} \left\langle \psi_{\boldsymbol{k}}^{A} | \psi_{\boldsymbol{k}}^{A} \right\rangle & \left\langle \psi_{\boldsymbol{k}}^{A} | \psi_{\boldsymbol{k}}^{B} \right\rangle \\ \left\langle \psi_{\boldsymbol{k}}^{B} | \psi_{\boldsymbol{k}}^{A} \right\rangle & \left\langle \psi_{\boldsymbol{k}}^{B} | \psi_{\boldsymbol{k}}^{B} \right\rangle \end{bmatrix} \tag{2.22}$$

multiplied by the eigenvalues $\epsilon_{\boldsymbol{k}}$. These eigenvalues will, therefore, satisfy

$$\det \begin{bmatrix} \left\langle \psi_{\boldsymbol{k}}^{A} \right| \mathcal{H} \left| \psi_{\boldsymbol{k}}^{A} \right\rangle - \epsilon_{\boldsymbol{k}} \left\langle \psi_{\boldsymbol{k}}^{A} | \psi_{\boldsymbol{k}}^{A} \right\rangle & \left\langle \psi_{\boldsymbol{k}}^{A} \right| \mathcal{H} \left| \psi_{\boldsymbol{k}}^{B} \right\rangle - \epsilon_{\boldsymbol{k}} \left\langle \psi_{\boldsymbol{k}}^{A} | \psi_{\boldsymbol{k}}^{B} \right\rangle \\ \left\langle \psi_{\boldsymbol{k}}^{B} \right| \mathcal{H} \left| \psi_{\boldsymbol{k}}^{A} \right\rangle - \epsilon_{\boldsymbol{k}} \left\langle \psi_{\boldsymbol{k}}^{B} | \psi_{\boldsymbol{k}}^{A} \right\rangle & \left\langle \psi_{\boldsymbol{k}}^{B} \right| \mathcal{H} \left| \psi_{\boldsymbol{k}}^{B} \right\rangle - \epsilon_{\boldsymbol{k}} \left\langle \psi_{\boldsymbol{k}}^{B} | \psi_{\boldsymbol{k}}^{B} \right\rangle \end{bmatrix} = 0$$

$$\det \left[\mathcal{H} - \epsilon_{\boldsymbol{k}} s_{\boldsymbol{k}} \right] = 0. \tag{2.23}$$

Apply the tight binding Hamiltonian to Eq. 2.23, and the result will be the same characteristic equation as Eq. 2.19. In order to determine graphene's electronic band structure $\epsilon_{\boldsymbol{k}}$ must be found by diagonalizing the Hamiltonian, which now reduces to solving the Eq. 2.19.

2.2.2 Solving the Characteristic Equation

The characteristic equation 2.19 is a matrix equation, written in matrix form it appears

$$\det \begin{bmatrix} t^{AA} - \epsilon s^{AA} & t^{AB} - \epsilon s^{AB} \\ t^{BA} - \epsilon s^{BA} & t^{BB} - \epsilon s^{BB} \end{bmatrix}_{\boldsymbol{k}} = 0. \tag{2.24}$$

By the superscripts one can infer that the diagonal elements of the characteristic matrix are the *NNN* interaction terms, and the off-diagonal elements are the *NN* terms.[2] Before evaluating this determinant, it is useful to find a more explicit form for the matrix elements of $t_{\boldsymbol{k}}$ and $s_{\boldsymbol{k}}$ than those that appear in Eq. 2.18. First consider only the *NN* terms for both $t_{\boldsymbol{k}}$ and $s_{\boldsymbol{k}}$.

Since *NN* atoms in the honeycomb lattice are atoms of separate sublattices, the lattice vectors $\boldsymbol{R}$ in Eq. 2.18 are all zero, so the *NN* terms of $t_{\boldsymbol{k}}$ and $s_{\boldsymbol{k}}$ depend only on the orbital wavefunction ϕ and the *NN* lattice vector $\boldsymbol{\delta}$ for all *NN* atoms. So $t_{\boldsymbol{k}}^{AB}$ and $s_{\boldsymbol{k}}^{AB}$ are

$$\begin{aligned} t_{\boldsymbol{k}}^{AB} &= \sum_{i=1}^{3} t_{\boldsymbol{k}}^{AB_i} \\ s_{\boldsymbol{k}}^{AB} &= \sum_{i=1}^{3} s_{\boldsymbol{k}}^{AB_i}, \end{aligned} \tag{2.25}$$

where $B_{1,2,3}$ are the three *NN* atoms to a central A atom, labeled in Fig. 2.1. The fact that $\boldsymbol{R} = 0$ for all the terms in Eq. 2.25 is problematic for several reasons, first, in this formulation ϕ is unknown and with three different $\boldsymbol{\delta}$-vectors all the integrals will be different and not easily evaluated. The more fatal flaw of this approach is that all information about how the hopping and overlap terms depend on the quasi-momentum is lost.[3] To resolve this issue, consider instead that a central A atom is

[2] See Fig. 1.1

[3] Since the only place where $\boldsymbol{R}$ appears in Eq. 2.18 is multiplying $\boldsymbol{k}$ in the exponential.

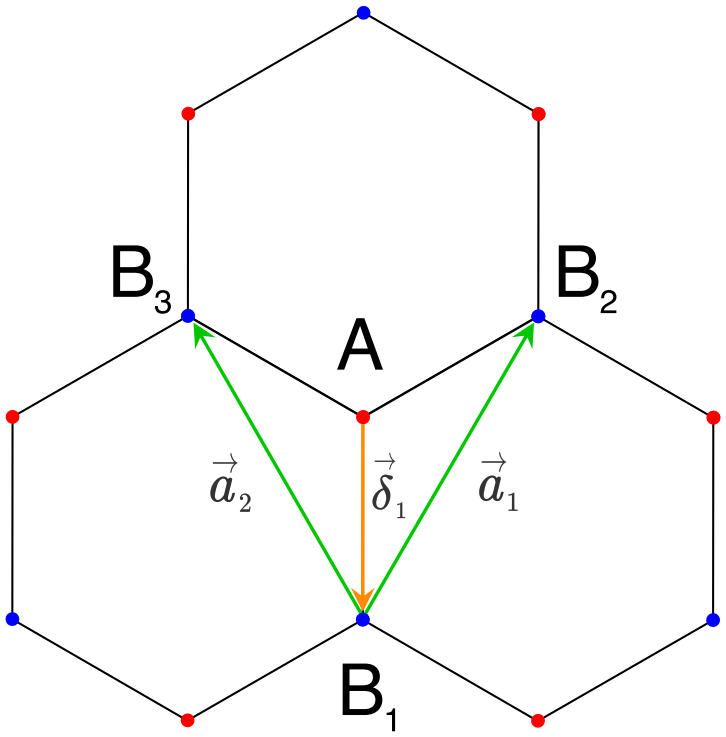

Figure 2.1: Translation from a central atom A to each of its three NN B atoms. The translation $\overrightarrow{AB}_1$ is simply $\boldsymbol{\delta}_1$, $\overrightarrow{AB}_2$ is $\boldsymbol{\delta}_1 + \boldsymbol{a}_1$, and $\overrightarrow{AB}_3$ is $\boldsymbol{\delta}_1 + \boldsymbol{a}_2$.

connected to any of its NN B atoms by a translation of $\boldsymbol{\delta}$.[4] From there, each of the other two NN atom positions can be defined by a translation of either $\boldsymbol{a}_1$ or $\boldsymbol{a}_2$ as shown in Fig. 2.1.

The advantage to considering the NN connections in terms of first a shift to the other sublattice and then a translation by either lattice vector is that now the NN terms of $t_{\boldsymbol{k}}$ and $s_{\boldsymbol{k}}$ depend on the lattice vectors $\boldsymbol{a}_1$ and $\boldsymbol{a}_2$, thus the dependence on quasi-momentum is preserved. Another advantage to this new perspective is that, since there is only one $\boldsymbol{\delta}$-vector to consider, all the integrals will be identical for each

[4]The choice of $\boldsymbol{\delta}_1$ as the initial translation between sublattices is semi-arbitrary, it could also have been $\boldsymbol{\delta}_2$ or $\boldsymbol{\delta}_3$, but either of those choices would have required the use of different lattice vectors from $\boldsymbol{a}_1$ and $\boldsymbol{a}_2$.

NN interaction, which can be defined as constants

$$\begin{aligned} t &= \int d^2r \phi^{A*}(\boldsymbol{r}) \Delta V \phi^B(\boldsymbol{r} + \boldsymbol{\delta}_1) \\ s &= \int d^2r \phi^{A*}(\boldsymbol{r}) \phi^B(\boldsymbol{r} + \boldsymbol{\delta}_1). \end{aligned} \tag{2.26}$$

With the definition of constants t and s,[5] Eq. 2.25 can be written more specifically, with the help of Eq. 2.18

$$\begin{aligned} t_{\boldsymbol{k}}^{AB} &= t \sum_{i=1}^{3} e^{i\boldsymbol{k}\cdot\boldsymbol{R}_{AB_i}} \\ s_{\boldsymbol{k}}^{AB} &= s \sum_{i=1}^{3} e^{i\boldsymbol{k}\cdot\boldsymbol{R}_{AB_i}}. \end{aligned} \tag{2.27}$$

The vectors $\boldsymbol{R}_{AB_i}$ are the lattice vectors connecting the central A atom to its three *NN* atoms B_i after shifting the origin by $\boldsymbol{\delta}_1$, so mathematically these vectors can be written

$$\boldsymbol{R}_{AB_i} = \overrightarrow{AB_i} - \boldsymbol{\delta}_1, \tag{2.28}$$

where $\overrightarrow{AB_i}$ are defined in the caption of Fig. 2.1. The sum in Eq. 2.27 is exactly the same for both $t_{\boldsymbol{k}}^{AB}$ and $s_{\boldsymbol{k}}^{AB}$, and so it is prudent to consider that sum as its own term called $\gamma_{\boldsymbol{k}}$. Using the definitions of $\boldsymbol{R}_{AB_i}$, $\gamma_{\boldsymbol{k}}$ becomes

$$\begin{aligned} \gamma_{\boldsymbol{k}} &= \sum_{i=1}^{3} e^{i\boldsymbol{k}\cdot\boldsymbol{R}_{AB_i}} \\ &= e^{i\boldsymbol{k}\cdot\boldsymbol{R}_{AB_1}} + e^{i\boldsymbol{k}\cdot\boldsymbol{R}_{AB_2}} + e^{i\boldsymbol{k}\cdot\boldsymbol{R}_{AB_3}} \\ &= e^{i\boldsymbol{k}\cdot(\boldsymbol{\delta}_1 - \boldsymbol{\delta}_1)} + e^{i\boldsymbol{k}\cdot(\boldsymbol{a}_1 + \boldsymbol{\delta}_1 - \boldsymbol{\delta}_1)} + e^{i\boldsymbol{k}\cdot(\boldsymbol{a}_2 + \boldsymbol{\delta}_1 - \boldsymbol{\delta}_1)} \\ \gamma_{\boldsymbol{k}} &= 1 + e^{i\boldsymbol{k}\cdot\boldsymbol{a}_1} + e^{i\boldsymbol{k}\cdot\boldsymbol{a}_2}. \end{aligned} \tag{2.29}$$

[5]Note that ϕ^A is a function of $\boldsymbol{r}$ alone since it is periodic with the lattice, and so the shift by $\boldsymbol{R}$ in Eq. 2.18 has no effect on ϕ. Also, ϕ^B includes a shift by $\boldsymbol{\delta}_1$ since the central atom is one of the A sublattice, and so the translation is needed because ϕ^B is not centered at the origin.

So finally,

$$\begin{aligned} t_{\boldsymbol{k}}^{AB} &= t\gamma_{\boldsymbol{k}} \\ s_{\boldsymbol{k}}^{AB} &= s\gamma_{\boldsymbol{k}}. \end{aligned} \tag{2.30}$$

Fig. 2.1 should make clear that, when an atom of the B sublattice is the central atom (meaning $t_{\boldsymbol{k}}^{BA}$ and $s_{\boldsymbol{k}}^{BA}$), $\boldsymbol{R}_{AB_i} = -\boldsymbol{R}_{BA_i}$. So, observing Eq. 2.29,

$$\begin{aligned} t_{\boldsymbol{k}}^{BA} &= t\gamma_{\boldsymbol{k}}^{*} = t_{\boldsymbol{k}}^{BA*} \\ s_{\boldsymbol{k}}^{BA} &= s\gamma_{\boldsymbol{k}}^{*} = s_{\boldsymbol{k}}^{BA*}. \end{aligned} \tag{2.31}$$

The exact value of $\gamma_{\boldsymbol{k}}$ will be evaluated later, but for now Eqs. 2.30 and 2.31 are a sufficiently complete form of the *NN* terms in the characteristic equation. The *NN* elements for $t_{\boldsymbol{k}}$ and $s_{\boldsymbol{k}}$ are remarkably similar in form, since both the overlap of the wavefunctions, and the potential interactions between *NN* atoms are both nontrivial integrals with a prefactor of $\gamma_{\boldsymbol{k}}$. This similarity does not continue to the *NNN* terms, which are the diagonal elements the characteristic equation.

The diagonal elements of $t_{\boldsymbol{k}}$ and $s_{\boldsymbol{k}}$ can no longer be found simultaneously and must be separately evaluated. The simplest terms to find are $s_{\boldsymbol{k}}^{AA}$ and $s_{\boldsymbol{k}}^{BB}$. Once again referencing Eq. 2.18,

$$\begin{aligned} s_{\boldsymbol{k}}^{AA} &= \left\langle \psi_{\boldsymbol{k}}^{A} \middle| \psi_{\boldsymbol{k}}^{A} \right\rangle = 1 \\ s_{\boldsymbol{k}}^{BB} &= \left\langle \psi_{\boldsymbol{k}}^{B} \middle| \psi_{\boldsymbol{k}}^{B} \right\rangle = 1 \end{aligned} \tag{2.32}$$

since the bloch wavefunctions are normalized. On the other hand, the *NNN* elements of the hopping matrix are not so trivial, consider $t_{\boldsymbol{k}}^{AA}$ alone,

$$t_{\boldsymbol{k}}^{AA} = \sum_{\beta=\pm 1} \sum_{i=1}^{3} e^{i\boldsymbol{k}\cdot\beta\boldsymbol{a}_i} \int d^2 r \phi^{A*}(\boldsymbol{r}) \Delta V \phi^{A}(\boldsymbol{r} - \beta\boldsymbol{a}_i) \tag{2.33}$$

where now a third lattice vector $\boldsymbol{a}_3$ has been included in the sum. This extra lattice vector was mentioned in Section 1.2 and is equal to $\sqrt{3}a\hat{x}$. Each atom has six *NNN* within the sublattice, and all of their positions relative to a central atom can be

described by translation by one of the three lattice vectors $\boldsymbol{a}_i$ and their negatives, hence the sum over $\beta = \pm 1$. However the interaction between all *NNN* atoms will be identical, with no preference on a particular direction, meaning that the integral will be the same for all values of $\beta\boldsymbol{a}_i$, so

$$t_{NNN} = \int d^2r \phi^{A*}(\boldsymbol{r}) \Delta V \phi^A(\boldsymbol{r} - \beta\boldsymbol{a}_i) \quad \forall \quad \beta\boldsymbol{a}_i. \tag{2.34}$$

Because there is only one atom type in graphene, t_{NNN} is the same for the $t_{\boldsymbol{k}}^{AA}$ and $t_{\boldsymbol{k}}^{BB}$. The lattice vectors within a sublattice are the same for either sublattice, so the sum of exponentials will also be the same for both $t_{\boldsymbol{k}}^{AA}$ and $t_{\boldsymbol{k}}^{BB}$. These two facts together imply that $t_{\boldsymbol{k}}^{AA} = t_{\boldsymbol{k}}^{BB}$. So, writing out the sum explicitly,

$$\begin{aligned} t_{\boldsymbol{k}}^{AA} &= t_{NNN}(e^{i\boldsymbol{k}\cdot\boldsymbol{a}_1} + e^{-i\boldsymbol{k}\cdot\boldsymbol{a}_1} + e^{i\boldsymbol{k}\cdot\boldsymbol{a}_2} + e^{-i\boldsymbol{k}\cdot\boldsymbol{a}_2} + e^{i\boldsymbol{k}\cdot\boldsymbol{a}_3} + e^{-i\boldsymbol{k}\cdot\boldsymbol{a}_3}) \\ t_{\boldsymbol{k}}^{AA} &= 2t_{NNN} \sum_i^3 \cos i\boldsymbol{k}\cdot\boldsymbol{a}_i = t_{NNN}(|\gamma_{\boldsymbol{k}}|^2 - 3), \end{aligned} \tag{2.35}$$

where $|\gamma_{\boldsymbol{k}}|^2 = \gamma_{\boldsymbol{k}}^* \gamma_{\boldsymbol{k}}$.

Having all of the elements of the hopping and overlap matrices the characteristic equation can be written explicitly in matrix form, leaving the more complicated *NNN* hopping terms simply as $t_{\boldsymbol{k}}^{AA}$,

$$\det \begin{bmatrix} t_{\boldsymbol{k}}^{AA} - \epsilon_{\boldsymbol{k}} & \gamma_{\boldsymbol{k}}^*(t - s\epsilon) \\ \gamma_{\boldsymbol{k}}(t - s\epsilon) & t_{\boldsymbol{k}}^{AA} - \epsilon_{\boldsymbol{k}} \end{bmatrix} = 0$$

$$\epsilon_{\boldsymbol{k}}^2(1 - |\gamma_{\boldsymbol{k}}|^2 s^2) + 2\epsilon_{\boldsymbol{k}}(|\gamma_{\boldsymbol{k}}|^2 st - t_{\boldsymbol{k}}^{AA}) + ((t_{\boldsymbol{k}}^{AA})^2 - |\gamma_{\boldsymbol{k}}|^2 t^2) = 0. \tag{2.36}$$

The two solutions, corresponding to $\beta = \pm$, come from the quadratic equation

$$\epsilon_{\boldsymbol{k}} = \frac{t_{\boldsymbol{k}}^{AA} - |\gamma_{\boldsymbol{k}}|^2 st + \beta|\gamma_{\boldsymbol{k}}|(t - st_{\boldsymbol{k}}^{AA})}{1 - |\gamma_{\boldsymbol{k}}|^2 s^2}$$

gather like powers of s,

$$\epsilon_{\boldsymbol{k}} = \frac{(t_{\boldsymbol{k}}^{AA} - \beta|\gamma_{\boldsymbol{k}}|t) + |\gamma_{\boldsymbol{k}}|s(|\gamma_{\boldsymbol{k}}|t + \beta t_{\boldsymbol{k}}^{AA})}{1 - |\gamma_{\boldsymbol{k}}|^2 s^2},$$

recognize that $\beta^2 = 1$, and so can be multiplied by any term with no effect,

$$\begin{aligned}
\epsilon_{\boldsymbol{k}} &= \frac{(t_{\boldsymbol{k}}^{AA} - \beta|\gamma_{\boldsymbol{k}}|t) + |\gamma_{\boldsymbol{k}}|s(\beta^2|\gamma_{\boldsymbol{k}}|t + \beta t_{\boldsymbol{k}}^{AA})}{1 - \beta^2|\gamma_{\boldsymbol{k}}|^2 s^2} \\
&= \frac{(t_{\boldsymbol{k}}^{AA} + \beta|\gamma_{\boldsymbol{k}}|t)(1 - \beta|\gamma_{\boldsymbol{k}}|s)}{(1 + \beta|\gamma_{\boldsymbol{k}}|s)(1 - \beta|\gamma_{\boldsymbol{k}}|s)} \\
\epsilon_{\boldsymbol{k}} &= \frac{t_{\boldsymbol{k}}^{AA} + \beta|\gamma_{\boldsymbol{k}}|t}{1 - \beta|\gamma_{\boldsymbol{k}}|s}.
\end{aligned} \tag{2.37}$$

In the tight binding model, the overlap of atomic orbitals between atoms is considered to be very small, as is the interaction between NNN atoms compared to the interaction between NN atoms ($t_{NNN} \ll t$), and so Eq. 2.37 can be expanded around $s = 0$ to be,

$$\epsilon_{\boldsymbol{k}} = t_{\boldsymbol{k}}^{AA} + \beta|\gamma_{\boldsymbol{k}}|t - |\gamma_{\boldsymbol{k}}|^2 st, \tag{2.38}$$

where a term $\beta|\gamma_{\boldsymbol{k}}|st_{\boldsymbol{k}}^{AA}$ was omitted since $st_{\boldsymbol{k}}^{AA}$ is very small. Equation 2.38 is the full band structure for all values of $\boldsymbol{k}$, and can be given more specifically using the definition for $t_{\boldsymbol{k}}^{AA}$ in Eq. 2.35,

$$\begin{aligned}
\epsilon_{\boldsymbol{k}} &= (t_{NNN} - st)|\gamma_{\boldsymbol{k}}|^2 + \beta t|\gamma_{\boldsymbol{k}}| - 3t_{NNN} \\
\epsilon_{\boldsymbol{k}} &= 2(t_{NNN} - st)\sum_{i=1}^{3} \cos \boldsymbol{k} \cdot \boldsymbol{a}_i + \beta t\sqrt{3 + 2\sum_{i=1}^{3} \cos \boldsymbol{k} \cdot \boldsymbol{a}_i} - 3t_{NNN}.
\end{aligned} \tag{2.39}$$

Using arbitrary values for t_{NNN}, s, and t, and the actual values for $\boldsymbol{a}_i$, Eq. 2.39 is the equation plotted in Fig. 2.2 (a) and (b).

Equation 2.39 shows that, apart from a small constant $3t_{NNN}$, every term of

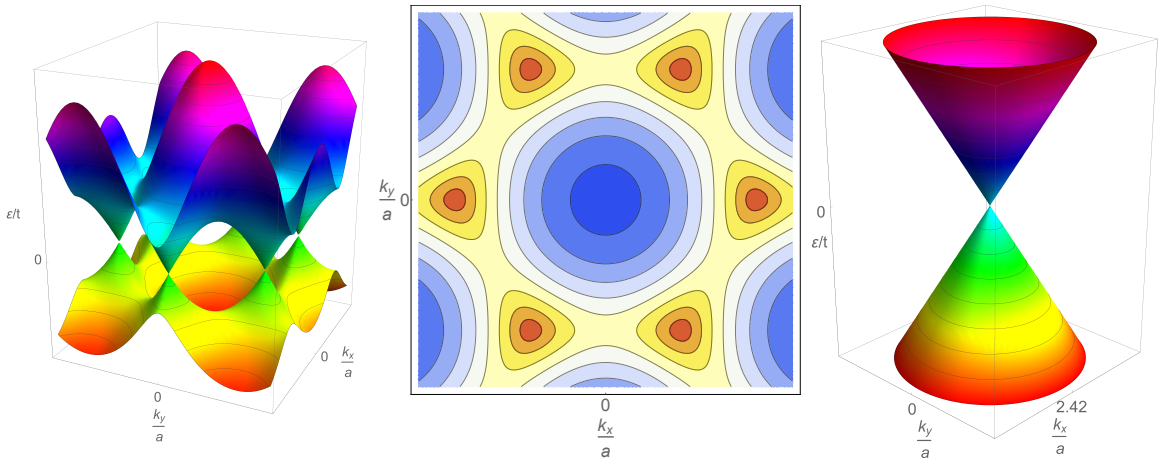

(a) (b) (c)

Figure 2.2: (a) The full band structure as given by Eq. 2.39. This figure shows one six points where the upper and lower band meet. The energies are in units of t, and the positions are in units of a. The maximum energy of the conduction band at the origin is about 12 eV (b) A contour map of (a), also plotted in units of a. Higher energy bands are in blue, while lower energy bands are in red. (c) The energy band very close to $\frac{\boldsymbol{k}}{a} = \frac{4\pi}{3\sqrt{3}}\hat{x}$, a Dirac point coinciding with one corner of the 1st BZ. Figure (c) is exactly the same as the linear spectrum of a Dirac cone given by Eq. 2.43.

the band structure depends on some power of $|\gamma_{\boldsymbol{k}}|$. So the value of $\boldsymbol{k}$ that satisfies $|\gamma_{\boldsymbol{k}}| = 0$ will also be the position in reciprocal space where the energy goes to zero. This point can be shown to be

$$\pm\boldsymbol{D} = \pm\frac{4\pi}{3\sqrt{3}a}\hat{x}, \tag{2.40}$$

which are exactly the two positions $\pm\boldsymbol{K}$, the inequivalent corners of the 1st BZ defined in Sec. 1.2.2. The positions $\pm\boldsymbol{D}$ are known as Dirac points, and they are significant for the reason that they are where the two bands meet; the central points for the Dirac cones like the one shown shown in Fig. 2.2 (c). An important note is that while $\pm\boldsymbol{K}$ and $\pm\boldsymbol{D}$ coincide in the reciprocal lattice, they are not directly connected: $\pm\boldsymbol{D}$ being where the energy goes to zero, and $\pm\boldsymbol{K}$ being crystallographic points from the construction of the 1st BZ. By altering the NN hopping amplitude, t, the positions of the Dirac points may be moved away from $\pm\boldsymbol{K}$, which will become

significant in Ch. 5.

Most electronic behavior in a material occur at low energies near where the conduction and valence bands are closest. In graphene, that is at the Dirac points, and so or all of the proceeding discussion the only relevant energy structure of graphene will be of that close to the Dirac points. A reasonable course of action would be to consider Eq. 2.38 at positions only a small displacement $\boldsymbol{q}$ from a Dirac point. A simple way to represent this is to redefine positions in reciprocal space by redefining the wave vector

$$\boldsymbol{k} = \pm\boldsymbol{D} + \boldsymbol{q}$$

and expand Eq. 2.38 around small values of $\boldsymbol{q}$. Since the expansion will only be valid for a small range of distances the overlap term s and the NNN interactions t_{NNN} can be disregarded entirely. So the band structure, discarding the notation of β, is much more simply,

$$\epsilon_{\boldsymbol{k}} = \pm|\gamma_{\boldsymbol{k}}|t. \tag{2.41}$$

The only factor in Eq. 2.41 is $|\gamma_{\boldsymbol{k}}|$, so to expand Eq. 2.41 around $\boldsymbol{q} = 0$ amounts only to expanding $|\gamma_{\boldsymbol{k}}|$.

$$\begin{aligned}
\gamma_{\boldsymbol{q}} &= 1 + e^{i(\pm\boldsymbol{D}+\boldsymbol{q})\cdot\boldsymbol{a}_1} + e^{i(\pm\boldsymbol{D}+\boldsymbol{q})\cdot\boldsymbol{a}_2} \\
&= 1 + e^{\pm i\frac{2\pi}{3}} e^{i\boldsymbol{q}\cdot\boldsymbol{a}_1} + e^{\mp i\frac{2\pi}{3}} e^{i\boldsymbol{q}\cdot\boldsymbol{a}_2} \\
\gamma_{\boldsymbol{q}} &\simeq 1 + e^{\pm i\frac{2\pi}{3}} \left(1 + i\boldsymbol{q}\cdot\boldsymbol{a}_1 - \frac{1}{2}\boldsymbol{q}\cdot\boldsymbol{a}_1\right) + e^{\mp i\frac{2\pi}{3}} \left(1 + i\boldsymbol{q}\cdot\boldsymbol{a}_2 - \frac{1}{2}\boldsymbol{q}\cdot\boldsymbol{a}_2\right)
\end{aligned}$$

truncating to first order in $\boldsymbol{q}$,

$$\begin{aligned}
\gamma_{\boldsymbol{q}} &\simeq 1 + e^{\pm i\frac{2\pi}{3}} + e^{\mp i\frac{2\pi}{3}} + ie^{\pm i\frac{2\pi}{3}}\boldsymbol{q}\cdot\boldsymbol{a}_1 + ie^{\mp i\frac{2\pi}{3}}\boldsymbol{q}\cdot\boldsymbol{a}_2 \\
&= i\frac{\sqrt{3}a}{2}\left[\left(-\frac{1}{2} \pm i\frac{\sqrt{3}}{2}\right)(q_x + \sqrt{3}q_y) + \left(-\frac{1}{2} \mp i\frac{\sqrt{3}}{2}\right)(-q_x + \sqrt{3}q_y)\right] \\
\gamma_{\boldsymbol{q}} &= \mp\frac{3a}{2}(q_x \pm iq_y) \\
|\gamma_{\boldsymbol{q}}| &= \frac{3a}{2}|\boldsymbol{q}|,
\end{aligned} \tag{2.42}$$

and so,

$$\epsilon_{\boldsymbol{q}} = \pm\frac{3at}{2}|\boldsymbol{q}| = \pm v_F\hbar|\boldsymbol{q}|. \tag{2.43}$$

This is the famous linear band structure of graphene, where the Fermi velocity has also been defined as

$$v_F = \frac{3at}{2\hbar}. \tag{2.44}$$

To get a sense of the energy scale of these cones, the hopping amplitude $t \simeq 3\ eV$[5], and as stated previously, the lattice parameter $a = 0.142\ nm$, making $v_F \sim 10^6\ \frac{m}{s}$, so $v_F\hbar \sim 10^{-10}\ eV\cdot m$. This may seem small, but while the quasi-momentum $\boldsymbol{q}$ (units of m^{-1}) is considered small per the expansion, in reality small is relative, and $\boldsymbol{q} \propto a^{-1}$ can actually be a large number. The energy from the first order expansion Eq. 2.43 is accurate to within 10% of the full solution, Eq. 2.38, up to energies of around 2 eV. This means $\boldsymbol{q} \to 10^{10}\ m^{-1}$ before this expansion requires higher order corrections. So effects within graphene can be described with a reasonable degree of accuracy, up to distances of about a lattice parameter, using only this linear spectrum.

Equation 2.43 describes the Dirac cones centered around Dirac points as shown in Fig. 2.2. While Fig. 2.2 (c) is simply a magnified image of a Dirac point in Fig. 2.2 (a), a plot of Eq. 2.38, plotting Eq. 2.43 would result in exactly the same plot as Fig. 2.2 (c). So Eq. 2.43 is exact when close to a Dirac point. The linear spectrum of graphene has many interesting properties and consequences[5], but the most relevant

for the following discussion is how this linear structure affects charge screening in graphene.

Chapter 3

Charge Screening and Polarization

The polarization of a linear dielectric is a phenomenon every undergraduate physics major learns. In short, when a dielectric is exposed to an external field the atoms in the material will polarize, aligning their dipole moments with the field. The result is that the entire material gains some net, static, polarization

$$\boldsymbol{P} = \varepsilon_0 \chi \boldsymbol{E}. \tag{3.1}$$

The electrons themselves do not rearrange within the material because they are bound to their atoms. In metals, this is not the case, and conduction band electrons are free to move in response to an applied external field, like that of a positive Coulomb impurity. They will do so in such a way that cancels out, or "screens", the effect of the field within the material: an effect aptly named screening in metals. For a full discussion of the concept of screening, consider either Chapter 14 in Kittel[10], or Chapter 17 in Ashcroft & Mermin[11]. The following discussion will be relatively brief and was gathered from those two texts, along primarily with the 2006 paper by Wunsch, Stauber, Sols, and Guinea[12].

3.1 Fundamentals of the Polarization in Graphene

In metals, instead of responding to an external field by polarizing, fields induce charge densities. These charge distributions will be expounded upon, but for now it is sufficient to note that given an external potential $V(\boldsymbol{q})$, the polarization charge density $n(\boldsymbol{q})$ is given by

$$n(\boldsymbol{q}) = Z\Pi(\boldsymbol{q})V(\boldsymbol{q}) \tag{3.2}$$

where Z is the external charge, and n is in units of the electron charge $|e|$. Equation 3.2 is in the limit of linear response, i.e. no electron-electron interactions. This equation is the metalic analog to Eq. 3.1. The value $\Pi(\boldsymbol{q})$ is known as the polarization function, or more lucidly, the Lindhard response function. The latter name is more descriptive because $\Pi(\boldsymbol{q})$, in spite of being called the polarization, it not analogous to the polarization in dielectrics, but it is instead the material's response to an external field making it the equivalent of $\varepsilon_0\chi$. However it will be referred to henceforth as simply the polarization.

The value of $\Pi(\boldsymbol{q})$ is given by the textbook equation

$$\Pi(\boldsymbol{q}) = \int_0^\infty \int_0^\infty \frac{d^2k}{4\pi^2} \frac{f(\epsilon_{\boldsymbol{k}}) - f(\epsilon_{\boldsymbol{k}+\boldsymbol{q}})}{\epsilon_{\boldsymbol{k}} - \epsilon_{\boldsymbol{k}+\boldsymbol{q}}}, \tag{3.3}$$

which applies for any generic two-dimensional electron gas (2DEG), and $f(\epsilon)$ are Fermi functions. So the polarization can be thought of as a weighted sum of probabilities that an electron in a metal will transition from an energy state $\psi_{\boldsymbol{k}}$ to $\psi_{\boldsymbol{k}+\boldsymbol{q}}$. The definition of the 2DEG is an extension of the free electron model, which assumes that the particles in the electron gas are Galilean invariant. That is to say the energy of an electron in the gas is given by

$$\epsilon_{\boldsymbol{k}} = \frac{\hbar^2\boldsymbol{p}^2}{2m}, \tag{3.4}$$

which non-relativistically is proportional to the square of the momentum $\boldsymbol{p}$. Graphene, on the other hand, is not Galilean invariant because its energy is linear with the momentum (Eq. 2.43), and is thus said to be relativistic-like, or *Lorentz* invariant.[1] The Lorentz invariance of graphene becomes significant in the topic of Coulomb response because of how Galilean and Lorentz invariant systems differ in how the ratio of Coulomb energy to kinetic energy of the electrons depend on charge density within the metal.

In a Galilean system, the average momentum per electron in d spatial dimensions is proportional to $n_d^{1/d}$, where $n_d = \ell^{-d}$ is the average electron density, and ℓ is the average distance between electrons. So the average kinetic energy per particle

$$T \sim \overline{\boldsymbol{p}} \propto n_d^{2/d}, \tag{3.5}$$

and the average Coulomb energy per electron as a result of a Coulomb potential, $V(r) = e^2/\varepsilon_0 r$, is

$$E_C \propto n_d^{1/d}, \tag{3.6}$$

thus,

$$\frac{E_C}{T} \propto n_d^{-1/d}, \tag{3.7}$$

The ratio of Eq. 3.7 has the implication that at low electron densities, $E_C \gg T$, and interaction with the Coulomb potential dominates over the kinetic energy of the electrons in determining their behavior. Conversely, at high densities, $E_C \ll T$ and the kinetic energy dominates over Coulomb interactions. So when there are fewer electrons in a region, they are more affected by a Coulomb impurity, but as the density increases the Coulomb potential is overwhelmed by electron-electron interactions and the kinetic energy of the electrons dominate. This is one aspect of the phenomenon

[1] While the energy of electrons in graphene may be relativistic-like, they are not actually relativistic particles, $\frac{v_F}{c} \ll 1$.

of screening in metals.

Lorentz invariant systems have a very different picture of the same ratio. Since the energy is now linear with the momentum

$$T_G \propto n_d^{-1/d}, \tag{3.8}$$

and with the same average Coulomb energy per electron,

$$\frac{E_C}{T_G} \propto n_0 \tag{3.9}$$

where n_0 is a constant that depends only on the properties of the lattice. So this ratio is entirely independent of electron density, completely counter to the Galilean invariant system. Given this highly unusual relationship between Coulomb energy and kinetic energy of electrons due to graphene's linear band energy, a natural question is how that band structure would affect how electrons in graphene respond to a Coulomb impurity.

3.1.1 Spin-Valley Degeneracy

In order to study Coulomb response in the graphene lattice, first return to Eq. 3.3 and modify from the polarization of a 2DEG to the specific case of graphene. The first thing to consider are any degeneracies in the band energy of graphene, since the polarization depends on that energy. There are two inequivalent Dirac points from the fact that there are two inequivalent corners of the 1st BZ from the construction of the reciprocal lattice.[2] This gives the band structure a twofold "valley degeneracy". Another type of degeneracy in graphene's energy is the result of a reformulation of the Hamiltonian in Sec. 2.2. Beginning with the matrix determinant in Eq. 2.36, make

[2]The six corners of the 1st BZ can also be thought of as three pairs of corners connected by a lattice vector $\boldsymbol{b}_i$. Two such corners are on opposite ends of the 1st BZ, refer to Fig. 1.2.

the assumptions that both the overlap between NN and the interactions between NNN can be disregarded before solving the determinant. Doing so results in (including $s_{\boldsymbol{k}}^{AA} = 1$)[3]

$$\det \begin{bmatrix} -\epsilon_{\boldsymbol{k}} s_{\boldsymbol{k}}^{AA} & \gamma_{\boldsymbol{k}}^* t \\ \gamma_{\boldsymbol{k}} t & -\epsilon_{\boldsymbol{k}} s_{\boldsymbol{k}}^{AA} \end{bmatrix} = 0,$$

which is still equivalent to Eq. 2.23 in the tight binding approximation. So writing the matrix alone

$$\begin{aligned} \mathcal{H}_{\boldsymbol{k}} - \epsilon_{\boldsymbol{k}} s_{\boldsymbol{k}} &= \begin{bmatrix} -\epsilon_{\boldsymbol{k}} s_{\boldsymbol{k}}^{AA} & \gamma_{\boldsymbol{k}}^* t \\ \gamma_{\boldsymbol{k}} t & -\epsilon_{\boldsymbol{k}} s_{\boldsymbol{k}}^{AA} \end{bmatrix} \\ \mathcal{H}_{\boldsymbol{k}} &= \begin{bmatrix} 0 & \gamma_{\boldsymbol{k}}^* t \\ \gamma_{\boldsymbol{k}} t & 0 \end{bmatrix}, \end{aligned} \tag{3.10}$$

and from Eq. 2.42, $\gamma_{\boldsymbol{q}} = \mp \frac{3a}{2}(q_x \pm i q_y)$,

$$\begin{aligned} \mathcal{H}_{\boldsymbol{q}} &= \mp \frac{3a}{2} t \begin{bmatrix} 0 & q_x - i q_y \\ q_x + i q_y & 0 \end{bmatrix} \\ &= \mp v_F \hbar \left[q_x \begin{pmatrix} 0 & 1 \\ 1 & 0 \end{pmatrix} + q_y \begin{pmatrix} 0 & -i \\ i & 0 \end{pmatrix} \right] \\ &= \pm v_F \hbar \left(q_x \sigma_x + q_y \sigma_y \right) \\ \mathcal{H}_{\boldsymbol{q}} &= \pm v_F \hbar \boldsymbol{q} \cdot \boldsymbol{\sigma}, \end{aligned} \tag{3.11}$$

where $\boldsymbol{\sigma}$ is the Pauli spin vector.

So the Hamiltonain for graphene is actually a sum of spin matrices. The form of the Hamiltonian in Eq. 3.11 is of the same form as that of the 2D Dirac equation,

[3] It is worth noting that solving this characteristic equation would result in the same solution as Eq. 2.41.

which describes relativistic massless fermions, making electrons in graphene an excellent example of Dirac fermions in nature. This has many more advanced implications on the nature of these Dirac particles that will not be discussed here[8, 9], but the more pertinent result of the Hamiltonian being a spin matrix is that of a twofold spin degeneracy in the energy. The doubly twofold spin-valley degeneracy will amount to a factor of 4 multiplying the polarization, which may seem like a minor detail, but an understanding of the origin of this factor is important.

3.1.2 Band Overlap of the Wavefunctions

Another important distinction with graphene to the 2DEG with regard to the polarization is that of inter and intraband transitions. In order for some amount of screening to take place electrons must be excited into higher energy states generating an electron-hole pair. Such transitions can take place either between the valence and conduction bands (interband transition) or within the same band (intraband transition). Note that in undoped graphene the Fermi levels is $\epsilon_F = 0$, but at some finite chemical potential, μ, intraband transitions can occur within the conduction band as well. So the polarization for graphene has an interband and an intraband transition component that must be summed

$$\Pi(\boldsymbol{q}) = \frac{g_s g_v}{4\pi^2} \sum_{s,s'=\pm 1} \int d^2k \frac{f(\epsilon^s_{\boldsymbol{k}}) - f(\epsilon^{s'}_{\boldsymbol{k}+\boldsymbol{q}})}{\epsilon^s_{\boldsymbol{k}} - \epsilon^{s'}_{\boldsymbol{k}+\boldsymbol{q}}},$$

where g_s and g_v denote the spin and valley degeneracies, each equal to 2, and s, s' denote inter/intraband transitions. Each s and s' can be equal to either ± 1; when $ss' > 0$ the transition from $\psi_{\boldsymbol{k}}$ to $\psi_{\boldsymbol{k}+\boldsymbol{q}}$ is intraband, and when $ss' < 0$, the transition is interband. Negative values for s or s' denote the valence band, while positive values denote the conduction band.

The polarization in graphene is slightly more complicated even than a double

sum over s and s' because the probability that a transition from $\psi_{\boldsymbol{k}}$ to $\psi_{\boldsymbol{k+q}}$ will be interband is not equal to the probability that transition will be intraband. These probabilities can be described by an overlap in the wave functions $\mathcal{F}^{ss'}(\boldsymbol{k},\boldsymbol{q})$, making the polarization for graphene of the form

$$\Pi(\boldsymbol{q}) = \frac{g_s g_v}{4\pi^2} \sum_{s,s'=\pm 1} \int d^2k \mathcal{F}^{ss'}(\boldsymbol{k},\boldsymbol{q}) \frac{f(\epsilon^s_{\boldsymbol{k}}) - f(\epsilon^{s'}_{\boldsymbol{k+q}})}{\epsilon^s_{\boldsymbol{k}} - \epsilon^{s'}_{\boldsymbol{k+q}}}. \tag{3.12}$$

The exact form and calculation of Eq. 3.12 has been written about extensively[5, 7, 12, 13], and will be done here in detail. First, the wave function overlap can be calculated by reconsidering the spin formulation of the Hamiltonain in Eq. 3.11, omitting the, for now, unimportant factor $\pm v_F \hbar$,

$$\mathcal{H}_{\boldsymbol{k}} = \boldsymbol{k}\cdot\boldsymbol{\sigma} = \begin{bmatrix} 0 & k_x - ik_y \\ k_x + ik_y & 0 \end{bmatrix}.$$

Writing the energy eigenvalue equation with some eigenstate in the energy basis $\left|\psi^{\pm}_{\boldsymbol{k}}\right\rangle$, where $\pm$ denotes the upper (conduction) and lower (valence) bands repsectively,

$$\begin{aligned} \mathcal{H}_{\boldsymbol{k}} \left|\psi^{\pm}_{\boldsymbol{k}}\right\rangle &= \epsilon^{\pm}_{\boldsymbol{k}} \left|\psi^{\pm}_{\boldsymbol{k}}\right\rangle \\ (\mathcal{H}_{\boldsymbol{k}} - \epsilon^{\pm}_{\boldsymbol{k}}) \left|\psi^{\pm}_{\boldsymbol{k}}\right\rangle &= 0 \\ \begin{bmatrix} -\epsilon^{\pm}_{\boldsymbol{k}} & k_x - ik_y \\ k_x + ik_y & -\epsilon^{\pm}_{\boldsymbol{k}} \end{bmatrix} \begin{bmatrix} \psi^1_{\boldsymbol{k}} \\ \psi^2_{\boldsymbol{k}} \end{bmatrix} &= 0, \end{aligned}$$

since $\left|\psi^{\pm}_{\boldsymbol{k}}\right\rangle$ is an arbitrary state vector with arbitrary components, let $\psi^1_{\boldsymbol{k}} = 1$ and $\psi^2_{\boldsymbol{k}} = \psi^{\pm}_{\boldsymbol{k}}$, so

$$\begin{bmatrix} -\epsilon^{\pm}_{\boldsymbol{k}} & k_x - ik_y \\ k_x + ik_y & -\epsilon^{\pm}_{\boldsymbol{k}} \end{bmatrix} \begin{bmatrix} 1 \\ \psi^{\pm}_{\boldsymbol{k}} \end{bmatrix} = 0. \tag{3.13}$$

Ultimately the wavefunction overlap, as the probability of transitioning from $\psi_{\boldsymbol{k}}$ to $\psi_{\boldsymbol{k}+\boldsymbol{q}}$ is given generically by

$$\mathcal{F}^{ss'}(\boldsymbol{k},\boldsymbol{q}) = \left|\left\langle \psi^{s}_{\boldsymbol{k}} \middle| \psi^{s'}_{\boldsymbol{k}+\boldsymbol{q}} \right\rangle\right|^2, \tag{3.14}$$

so determining $\mathcal{F}^{ss'}(\boldsymbol{k},\boldsymbol{q})$ is a matter of solving Eq. 3.13 for $\psi^{+}_{\boldsymbol{k}}$ and $\psi^{-}_{\boldsymbol{k}}$. Beginning with $\psi^{+}_{\boldsymbol{k}}$ the energy eigenvalue equation results in a system of equations,

$$\begin{bmatrix} -\epsilon^{+}_{\boldsymbol{k}} & k_x - ik_y \\ k_x + ik_y & -\epsilon^{+}_{\boldsymbol{k}} \end{bmatrix} \begin{bmatrix} 1 \\ \psi^{+}_{\boldsymbol{k}} \end{bmatrix} = 0$$

$$\begin{cases} -\epsilon^{+}_{\boldsymbol{k}} + (k_x - ik_y)\psi^{+}_{\boldsymbol{k}} &= 0 \\ k_x + ik_y - \epsilon^{+}_{\boldsymbol{k}}\psi^{+}_{\boldsymbol{k}} &= 0 \end{cases}$$

$$\begin{cases} (k_x - ik_y)\psi^{+}_{\boldsymbol{k}} &= \epsilon^{+}_{\boldsymbol{k}} \\ k_x + ik_y &= \epsilon^{+}_{\boldsymbol{k}}\psi^{+}_{\boldsymbol{k}} \end{cases}$$

$$\begin{cases} \psi^{+}_{\boldsymbol{k}} &= \frac{\epsilon^{+}_{\boldsymbol{k}}}{k_x - ik_y} \\ \psi^{+}_{\boldsymbol{k}} &= \frac{k_x + ik_y}{\epsilon^{+}_{\boldsymbol{k}}} \end{cases},$$

these two solutions are equivalent due to the fact that $(k_x - ik_y)(k_x + ik_y) = k_x^2 + k_y^2 = (\epsilon^{+}_{\boldsymbol{k}})^2 = |\boldsymbol{k}|^2$, so

$$\psi^{+}_{\boldsymbol{k}} = \frac{k_x + ik_y}{\epsilon^{+}_{\boldsymbol{k}}} = \frac{k_x + ik_y}{|\boldsymbol{k}|},$$

and by the same procedure,

$$\psi^{-}_{\boldsymbol{k}} = \frac{k_x + ik_y}{\epsilon^{-}_{\boldsymbol{k}}} = -\frac{k_x + ik_y}{|\boldsymbol{k}|}.$$

Finally, the normalized state vectors are, in terms of s and s',

$$|\psi^s_{\boldsymbol{k}}\rangle = \frac{1}{\sqrt{2}} \begin{bmatrix} 1 \\ s\frac{k_x+ik_y}{|\boldsymbol{k}|} \end{bmatrix} \qquad \left|\psi^{s'}_{\boldsymbol{k}}\right\rangle = \frac{1}{\sqrt{2}} \begin{bmatrix} 1 \\ s'\frac{k_x+ik_y}{|\boldsymbol{k}|} \end{bmatrix}. \tag{3.15}$$

Now the wavefunction overlap (Eq. 3.14) can be explicitly calculated,

$$\begin{aligned}
\mathcal{F}^{ss'}(\boldsymbol{k},\boldsymbol{q}) &= \left|\left\langle \psi^s_{\boldsymbol{k}} \middle| \psi^{s'}_{\boldsymbol{k}+\boldsymbol{q}} \right\rangle\right|^2 \\
&= \frac{1}{4}\left| \begin{bmatrix} 1 & s\frac{k_x-ik_y}{|\boldsymbol{k}|} \end{bmatrix} \begin{bmatrix} 1 \\ s'\frac{(k+q)_x+i(k+q)_y}{|\boldsymbol{k}+\boldsymbol{q}|} \end{bmatrix} \right|^2 \\
&= \frac{1}{4}\left|1 + ss'\frac{k_x(k+q)_x + k_y(k+q)_y}{|\boldsymbol{k}||\boldsymbol{k}+\boldsymbol{q}|} + iss'\frac{k_x(k+q)_y - k_y(k+q)_x}{|\boldsymbol{k}||\boldsymbol{k}+\boldsymbol{q}|}\right|^2 \\
&= \frac{1}{4}\left[\left(1 + ss'\frac{k_x(k+q)_x + k_y(k+q)_y}{|\boldsymbol{k}||\boldsymbol{k}+\boldsymbol{q}|}\right)^2 + \left(ss'\frac{k_x(k+q)_y - k_y(k+q)_x}{|\boldsymbol{k}||\boldsymbol{k}+\boldsymbol{q}|}\right)^2\right] \\
&= \frac{1}{2}\left(1 + ss'\frac{k_x(k+q)_x + k_y(k+q)_y}{|\boldsymbol{k}||\boldsymbol{k}+\boldsymbol{q}|}\right) \\
\mathcal{F}^{ss'}(\boldsymbol{k},\boldsymbol{q}) &= \frac{1}{2}\left(1 + ss'\frac{\boldsymbol{k}\cdot(\boldsymbol{k}+\boldsymbol{q})}{|\boldsymbol{k}||\boldsymbol{k}+\boldsymbol{q}|}\right),
\end{aligned} \tag{3.16}$$

utilizing the fact that $(ss')^2 = ss'$.

3.1.3 Inter/Intraband Transition terms in the Polarization

With the exact form of $\mathcal{F}^{ss'}(\boldsymbol{k},\boldsymbol{q})$, everything needed to calculate $\Pi(\boldsymbol{q})$ for graphene is now in hand, but there is one more small consideration that must be made before diving into the derivation. While there is no reason why $\Pi(\boldsymbol{q})$ cannot be calculated for the band structure Eq. 2.43, the result would be uninteresting. In metals, the screened Coulomb potential depends intrinsically on the Fermi level ϵ_F[10]. In the Thomas-Fermi theory of screening (of which the Lindhard theory used here is

a quantum mechanical correction to) states that the screened Coulomb potential is

$$V_s(\boldsymbol{r}) = \frac{Q}{r} e^{-k_0 r}$$

where k_0 is proportional to the Fermi-momentum k_F[11]. If $k_F = 0$ then the the screened potential would decay as r^{-1} just as an unscreened Coulomb potential, meaning that no screening occurs. For undoped graphene $\epsilon_F = 0$, and by extension $k_F = 0$, and so screening of a Coulomb impurity is entirely suppressed. So for there to result in an interesting distribution of charge, ϵ_F must be moved, and this can be accomplished by considering the band structure at some finite chemical potential μ,

$$\epsilon^{\pm}_{\boldsymbol{k}} = \pm v_F \hbar |\boldsymbol{k}| - \mu. \tag{3.17}$$

The addition of μ has a profound impact on the form of the charge density. A fact that will be further explained after the polarization has been derived, which begins with recalling Eq. 3.12,

$$\Pi(\boldsymbol{q}) = \frac{g_s g_v}{4\pi^2} \sum_{s,s'=\pm 1} \int d^2k \mathcal{F}^{ss'}(\boldsymbol{k}, \boldsymbol{q}) \frac{f(\epsilon^s_{\boldsymbol{k}}) - f(\epsilon^{s'}_{\boldsymbol{k}+\boldsymbol{q}})}{\epsilon^s_{\boldsymbol{k}} - \epsilon^{s'}_{\boldsymbol{k}+\boldsymbol{q}}},$$

where, for notational simplicity, the full form of $\mathcal{F}^{ss'}(\boldsymbol{k}, \boldsymbol{q})$ in Eq. 3.16, it will be included later. The sum in Eq. 3.12 has four terms, $(s, s') = \{(1,1), (1,-1), (-1,1), (-1,-1)\}$, so the polarization can be written as a sum of four $\Pi^{ss'}_{\boldsymbol{q}}$ terms,

$$\frac{4\pi^2 \Pi(\boldsymbol{q})}{g_s g_v} = \sum_{s,s'=\pm 1} \Pi^{ss'}_{\boldsymbol{q}} = \Pi^{++}_{\boldsymbol{q}} + \Pi^{+-}_{\boldsymbol{q}} + \Pi^{-+}_{\boldsymbol{q}} + \Pi^{--}_{\boldsymbol{q}}, \tag{3.18}$$

so $\Pi^{ss'}_{\boldsymbol{q}}$ is the integral of Eq. 3.12,

$$\Pi^{ss'}_{\boldsymbol{q}} = \int d^2k \mathcal{F}^{ss'}(\boldsymbol{k}, \boldsymbol{q}) \frac{f(\epsilon^s_{\boldsymbol{k}}) - f(\epsilon^{s'}_{\boldsymbol{k}+\boldsymbol{q}})}{\epsilon^s_{\boldsymbol{k}} - \epsilon^{s'}_{\boldsymbol{k}+\boldsymbol{q}}}. \tag{3.19}$$

At zero temperature the Fermi functions reduce to step functions, so substitute Eq. 3.17 into this integral (once again omitting $v_F\hbar$),

$$\Pi_{\boldsymbol{q}}^{ss'} = \int d^2k \mathcal{F}^{ss'}(\boldsymbol{k},\boldsymbol{q}) \frac{\Theta(s|\boldsymbol{k}| - \mu) - \Theta(s'|\boldsymbol{k}+\boldsymbol{q}| - \mu)}{s|\boldsymbol{k}| - s'|\boldsymbol{k}+\boldsymbol{q}|}. \tag{3.20}$$

The step functions limit the upper bound of the integral to the value of $\boldsymbol{k}$ for which the argument of Θ goes to zero. Each $\Pi_{\boldsymbol{q}}^{ss'}$ therefore becomes two integrals with different limits: ones whose upper limit is C_1^s, the solution to $s|\boldsymbol{k}| - \mu = 0$, and others whose upper limit $C_2^{s'}$, the solution to $s|\boldsymbol{k}+\boldsymbol{q}| - \mu = 0$. If solutions to $s|\boldsymbol{k}+\boldsymbol{q}| - \mu = 0$ or $s'|\boldsymbol{k}| - \mu = 0$ do not exist then the upper limit remains infinite. The expanded form of Eq. 3.19 is then

$$\Pi_{\boldsymbol{q}}^{ss'} = \int\limits_{k<C_1^s} d^2k \frac{\mathcal{F}^{ss'}(\boldsymbol{k},\boldsymbol{q})}{s|\boldsymbol{k}| - s'|\boldsymbol{k}+\boldsymbol{q}|} - \int\limits_{k<C_2^{s'}} d^2k \frac{\mathcal{F}^{ss'}(\boldsymbol{k},\boldsymbol{q})}{s|\boldsymbol{k}| - s'|\boldsymbol{k}+\boldsymbol{q}|}. \tag{3.21}$$

The upper bounds each have two values corresponding to $s, s' = \pm 1$: $C_1^+ = \mu$, $C_1^- = \infty$, and $C_2^- = \infty$. The equation $|\boldsymbol{k}+\boldsymbol{q}| - \mu = 0$ does not have a simple solution, so C_2^+ will be set equal to some constant upper-bound C. The term $\Pi_{\boldsymbol{q}}^{--}$ is significant for the fact that the upperbounds for both terms in Eq. 3.21, and the integrands for both terms are also equal, so

$$\Pi_{\boldsymbol{q}}^{--} = \int\limits_{k<\infty} d^2k \frac{\mathcal{F}^{+}(\boldsymbol{k},\boldsymbol{q})}{-|\boldsymbol{k}| + |\boldsymbol{k}+\boldsymbol{q}|} - \int\limits_{k<\infty} d^2k \frac{\mathcal{F}^{+}(\boldsymbol{k},\boldsymbol{q})}{-|\boldsymbol{k}| + |\boldsymbol{k}+\boldsymbol{q}|}$$

$$\Pi_{\boldsymbol{q}}^{--} = 0, \tag{3.22}$$

the intraband contribution to the polarization for transitions within the valence band is zero.[4] In other words, there can be no polarizations from electrons transitioning

[4]Note the "+" superscript for $\mathcal{F}$ in Eq. 3.22 in spite of both s and s' being negative. This is because $\mathcal{F}$ does not depend on s and s' separately, but rather their product. Unlike $\Pi_{\boldsymbol{q}}^{ss'}$, it does not distinguish between transitions in the conduction band, and those in the valence band, only whether or not the transition is intraband or interband. So $\mathcal{F}^{++} = \mathcal{F}^{--} = \mathcal{F}^{+}$, and $\mathcal{F}^{+-} = \mathcal{F}^{-+} = \mathcal{F}^{-}$.

within the valence band; for screening to occur electrons must transition either from the valence band to the conduction band, or within the conduction band. This can be thought of as a consequence of finite μ since polarizations depend on transitions across the Fermi level.

Next consider terms where the upper-bound is C, $\Pi_{\boldsymbol{q}}^{++}$ and $\Pi_{\boldsymbol{q}}^{-+}$,

$$\begin{aligned}\Pi_{\boldsymbol{q}}^{++} &= \int\limits_{k<\mu} d^2k \frac{\mathcal{F}^{+}(\boldsymbol{k},\boldsymbol{q})}{|\boldsymbol{k}| - |\boldsymbol{k}+\boldsymbol{q}|} - \int\limits_{k<C} d^2k \frac{\mathcal{F}^{+}(\boldsymbol{k},\boldsymbol{q})}{|\boldsymbol{k}| - |\boldsymbol{k}+\boldsymbol{q}|} \\ \Pi_{\boldsymbol{q}}^{-+} &= \int\limits_{k<\infty} d^2k \frac{\mathcal{F}^{-}(\boldsymbol{k},\boldsymbol{q})}{-|\boldsymbol{k}| - |\boldsymbol{k}+\boldsymbol{q}|} - \int\limits_{k<C} d^2k \frac{\mathcal{F}^{-}(\boldsymbol{k},\boldsymbol{q})}{-|\boldsymbol{k}| - |\boldsymbol{k}+\boldsymbol{q}|},\end{aligned} \tag{3.23}$$

make the substitution $\boldsymbol{k} = \boldsymbol{k} - \boldsymbol{q}$, meaning that the upper-bound C is now the solution to the equation $|\boldsymbol{k} - \boldsymbol{q} + \boldsymbol{q}| - \mu = 0$, making $C = \mu$ after this substitution. Since the integrands are even[5] in $\boldsymbol{q}$, $|\boldsymbol{k} - \boldsymbol{q}| = |\boldsymbol{k} + \boldsymbol{q}|$, and Eq. 3.23 is transformed to

$$\begin{aligned}\Pi_{\boldsymbol{q}}^{++} &= \int\limits_{k<\mu} d^2k \frac{\mathcal{F}^{+}(\boldsymbol{k},\boldsymbol{q})}{|\boldsymbol{k}| - |\boldsymbol{k}+\boldsymbol{q}|} - \int\limits_{k<\mu} d^2k \frac{\mathcal{F}^{+}(\boldsymbol{k},\boldsymbol{q})}{-|\boldsymbol{k}| + |\boldsymbol{k}+\boldsymbol{q}|} \\ \Pi_{\boldsymbol{q}}^{-+} &= \int\limits_{k<\mu} d^2k \frac{\mathcal{F}^{-}(\boldsymbol{k},\boldsymbol{q})}{|\boldsymbol{k}| + |\boldsymbol{k}+\boldsymbol{q}|} - \int\limits_{k<\infty} d^2k \frac{\mathcal{F}^{-}(\boldsymbol{k},\boldsymbol{q})}{|\boldsymbol{k}| + |\boldsymbol{k}+\boldsymbol{q}|}.\end{aligned} \tag{3.24}$$

The remaining unmentioned term is $\Pi_{\boldsymbol{q}}^{+-}$ is

$$\Pi_{\boldsymbol{q}}^{+-} = \int\limits_{k<\mu} d^2k \frac{\mathcal{F}^{+}(\boldsymbol{k},\boldsymbol{q})}{|\boldsymbol{k}| + |\boldsymbol{k}+\boldsymbol{q}|} - \int\limits_{k<\infty} d^2k \frac{\mathcal{F}^{+}(\boldsymbol{k},\boldsymbol{q})}{|\boldsymbol{k}| + |\boldsymbol{k}+\boldsymbol{q}|}. \tag{3.25}$$

[5]The only two terms where $\boldsymbol{q}$ appears are $\boldsymbol{k}\cdot\boldsymbol{q}$ (from $\mathcal{F}$), and $|\boldsymbol{k}+\boldsymbol{q}|$. Each of these can be written in forms where the only odd power of $\boldsymbol{q}$ multiplies a factor of $\cos\varphi$, where φ is the angle between $\boldsymbol{k}$ and $\boldsymbol{q}$. When $\boldsymbol{q}$ changes sign so does φ, and thus the product of $\boldsymbol{q}$ and $\cos\varphi$ will be even under parity of $\boldsymbol{q}$.

Finally, substituting Eqs. 3.22, 3.24, and 3.25 into Eq. 3.18, summing like terms, and reintroducing the notation $\epsilon_{\boldsymbol{k}}^{\pm} = \pm|\boldsymbol{k}|$,

$$\Pi(\boldsymbol{q}) = \frac{2g_s g_v}{4\pi^2}\left[\int_{k<\mu} d^2k \frac{\mathcal{F}^+(\boldsymbol{k},\boldsymbol{q})}{\epsilon_{\boldsymbol{k}}^+ - \epsilon_{\boldsymbol{k}+\boldsymbol{q}}^+} + \int_{k<\mu} d^2k \frac{\mathcal{F}^-(\boldsymbol{k},\boldsymbol{q})}{\epsilon_{\boldsymbol{k}}^+ - \epsilon_{\boldsymbol{k}+\boldsymbol{q}}^-} - \int_{k<\infty} d^2k \frac{\mathcal{F}^-(\boldsymbol{k},\boldsymbol{q})}{\epsilon_{\boldsymbol{k}}^+ - \epsilon_{\boldsymbol{k}+\boldsymbol{q}}^-}\right]. \quad (3.26)$$

An elucidative interpretation of Eq. 3.26 is that the polarization in graphene is the the difference between the sum of interband and intraband polarizations at finite μ and interband transitions without any chemical potential.

Up to this point in the discussion, the only modification to the linear band structure in Eq. 2.43 has been to include a finite chemical potential μ. Since none of the dot products in $\mathcal{F}$ or the additions to $\boldsymbol{k}$ in $\epsilon_{\boldsymbol{k}+\boldsymbol{q}}$ have needed to be evaluated, the specific components of $\epsilon_{\boldsymbol{k}}$ and $\boldsymbol{q}$ are not yet relevant. However to move forward in the discussion these components must be considered, and that leads to a central aspect of this investigation, the application of strain on graphene.

3.2 Uniaxial Strain and the Polarization Function

How strain affects screening of a Coulomb impurity in graphene is a keystone concept in this investigation. There is no reason why Eq. 3.26 cannot be evaluated for isotropic graphene, indeed this has been done, and the resultant charge density studied in detail[12]. The central question to the first case mentioned in Sec. 1.3 is, then, how do those results differ when uniaxial strain is applied along the armchair direction in graphene?

To begin, recall the equation for Dirac cones both in terms of the Fermi velocity, v_F and the NN hopping amplitude t,

$$\epsilon_{\boldsymbol{q}} = \pm\frac{3at}{2}|\boldsymbol{q}| = \pm v_F\hbar|\boldsymbol{q}|.$$

In isotropic graphene, all *NN* lattice vectors $\boldsymbol{\delta}_i$ have the exact same magnitude, and recall the definition of t,

$$t = \int d^2 r \phi^{(m)*}(\boldsymbol{r}) \Delta V \phi^{(n)}(\boldsymbol{r} + \boldsymbol{\delta}_1),$$

for $m \neq n$. The argument in Sec 2.2.2 was that this was a constant amplitude for all *NN* interactions since a central atom could be connected to all of its *NN* by a shift by any $\boldsymbol{\delta}$-vector followed wtih a translation by an $\boldsymbol{a}$-vector. Since all $\boldsymbol{\delta}$-vectors have equal magnitude in unstrained graphene, the choice of which to initially translate by was arbitrary, but when strain is applied along the armchair direction this is no longer the case. One can imagine stretching the honeycomb lattice in Fig. 1.1 so that the $\hat{y}$-components of $\boldsymbol{\delta}_i$ are elongated, and so some inherent dependence on direction must be incorporated into the amplitude of *NN* interactions, t. Conceptually, the distance between *NN* atoms in graphene now varies by direction, and interactions fundamentally depend on distance. So by straining graphene along the armchair direction, t would now become a vector,

$$\boldsymbol{t} = t_x \hat{x} + t_y \hat{y},$$

meaning that v_F, which is directly proportional to t (Eq. 2.44), would also now have unequal vector components. As a result $\epsilon_{\boldsymbol{q}}$ would now be proportional to the magnitude of a new vector

$$\widetilde{\boldsymbol{q}} = v_{Fx} q_x \hat{x} + v_{Fy} q_y \hat{y},$$

and,

$$\epsilon_{\widetilde{\boldsymbol{q}}} = \pm\hbar|\widetilde{\boldsymbol{q}}| = \pm\hbar\sqrt{v_{Fx}^2 q_x^2 + v_{Fy}^2 q_y^2}. \tag{3.27}$$

In principle, Eq. 3.27 is the most general form of the band structure near the Dirac points. In the unstrained case, $v_{Fx} = v_{Fy} = v_F$, and one recovers the original isotropic

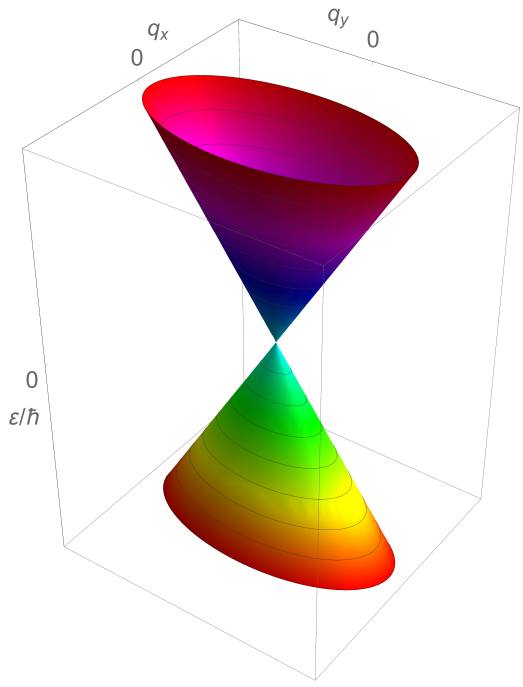

Figure 3.1: An elliptic Dirac cone plotted directly from Eq. 3.27. This plot simulates strain along the armchair direction, i.e. $v_{Fx} > v_{Fy}$. The scale is arbitrary, but proportional, higher momenta must be reached along the $\hat{y}$-direction to achieve the same energy as along the $\hat{x}$-direction, which carries the implication that were an electron to transition to a higher energy state and polarize, it would be more likely to do so along in the zig-zag direction.

band structure.

On the other hand, when strain is applied along the armchair direction, $v_{Fx} > v_{Fy}$[6], and the band structure described in Eq. 3.27 will be that of an *elliptic* Dirac cone, shown in Fig. 3.1. This elliptic band structure can be applied to the polarization, Eq. 3.26. It may be tempting to believe that with this change, much of the analysis in the previous section no longer applies and Eq. 3.26 is not valid under strain. However the redefinition of $\widetilde{\boldsymbol{q}}$ from $\boldsymbol{q}$ can be applied to all the vectors in the polarization and treated as a change of variables. Thus, the only manifestation of

[6]Strain along a particular direction will decrease the Fermi velocity in that direction.

strain in the polarization will be a new prefactor including v_{Fx} and v_{Fy},

$$\Pi(\boldsymbol{q}) = \frac{2g_s g_v}{4\pi^2 v_x v_y}\left[\int\limits_{k<\mu} d^2k \frac{\mathcal{F}^+(\boldsymbol{k},\boldsymbol{q})}{\epsilon^+_{\boldsymbol{k}} - \epsilon^+_{\boldsymbol{k}+\boldsymbol{q}}} + \int\limits_{k<\mu} d^2k \frac{\mathcal{F}^-(\boldsymbol{k},\boldsymbol{q})}{\epsilon^+_{\boldsymbol{k}} - \epsilon^-_{\boldsymbol{k}+\boldsymbol{q}}} - \int\limits_{k<\infty} d^2k \frac{\mathcal{F}^-(\boldsymbol{k},\boldsymbol{q})}{\epsilon^+_{\boldsymbol{k}} - \epsilon^-_{\boldsymbol{k}+\boldsymbol{q}}}\right], \tag{3.28}$$

where for notational simplicity, both the F subscript and the tilde have been omitted; with the prefactor $v_x v_y$ the presence of strain has been accounted for, and no further indication of it need be made.

Each of the integrals in Eq. 3.28 are very similar, and evaluating all three at once would be cumbersome, thus it pays to introduce a new function

$$\chi_U^{ss'}(\boldsymbol{q}) = \int\limits_{k<U} d^2k \frac{\mathcal{F}^{ss'}(\boldsymbol{k},\boldsymbol{q})}{\epsilon^s_{\boldsymbol{k}} - \epsilon^{s'}_{\boldsymbol{k}+\boldsymbol{q}}}$$

so that Eq. 3.28 can be more compactly written

$$\Pi(\boldsymbol{q}) = \frac{2g_s g_v}{4\pi^2 v_x v_y}\left[\chi_\mu^{++}(\boldsymbol{q}) + \chi_\mu^{+-}(\boldsymbol{q}) - \chi_\infty^{+-}(\boldsymbol{q})\right], \tag{3.29}$$

and each χ function can be evaluated individually. First χ_∞^{+-}, now using the exact form of the wavefunction overlap from Eq. 3.16, and magnitudes of vectors will henceforth be written $A \equiv |\boldsymbol{A}|$,

$$\begin{aligned}
\chi_\infty^{+-}(\boldsymbol{q}) &= \frac{1}{2}\int\limits_{k<\infty} d^2k \left(1 - \frac{\boldsymbol{k}\cdot(\boldsymbol{k}+\boldsymbol{q})}{|\boldsymbol{k}||\boldsymbol{k}+\boldsymbol{q}|}\right)\frac{1}{|\boldsymbol{k}| + |\boldsymbol{k}+\boldsymbol{q}|} \\
&= \frac{1}{2}\int\limits_{k<\infty} d^2k \left(1 - \frac{\boldsymbol{k}\cdot\boldsymbol{k} + \boldsymbol{k}\cdot\boldsymbol{q}}{|\boldsymbol{k}||\boldsymbol{k}+\boldsymbol{q}|}\right)\frac{1}{|\boldsymbol{k}| + |\boldsymbol{k}+\boldsymbol{q}|} \\
\chi_\infty^{+-}(\boldsymbol{q}) &= \frac{1}{2}\int_0^\infty \int_0^{2\pi} dk d\varphi k \left(1 - \frac{k^2 + kq\cos\varphi}{k\sqrt{k^2+q^2+kq\cos\varphi}}\right)\frac{1}{k + \sqrt{k^2+q^2+kq\cos\varphi}},
\end{aligned}$$

where φ is the angle between $\boldsymbol{k}$ and $\boldsymbol{q}$, and the absolute value notation for vector magnitudes has been dropped, and henceforth $A \equiv |\boldsymbol{A}|$,

$$\chi_{\infty}^{+-}(\boldsymbol{q}) = \frac{1}{2}\int_0^{\infty}\int_0^{2\pi} dk d\varphi k \left(1 - \frac{k + q\cos\varphi}{\sqrt{k^2+q^2+kq\cos\varphi}}\right)\frac{1}{k+\sqrt{k^2+q^2+kq\cos\varphi}},$$

substitute $k = k'q$ and simplify,

$$\chi_{\infty}^{+-}(\boldsymbol{q}) = \frac{q}{2}\int_0^{\infty}\int_0^{2\pi} dk' d\varphi k' \left(1 - \frac{k' + \cos\varphi}{\sqrt{k'^2+1+k'\cos\varphi}}\right)\frac{1}{k'+\sqrt{k'^2+1+k'\cos\varphi}}, \tag{3.30}$$

which can be evaluated to be

$$\chi_{\infty}^{+-}(\boldsymbol{q}) = \frac{q\pi^2}{8}. \tag{3.31}$$

A very similar procedure and a good deal of algebra can be applied to the sum of the terms where μ is the upper-bound of the integration, simplifying them to

$$\chi_{\mu}^{++}(\boldsymbol{q}) + \chi_{\mu}^{+-}(\boldsymbol{q}) = \chi_{\mu}(\boldsymbol{q}) = -\frac{q}{2}\int_0^{\frac{2\mu}{q}}\int_0^{\pi} dk' d\varphi \frac{k'^2 + k'\cos\varphi}{1+k'\cos\varphi}. \tag{3.32}$$

The only significant difference in the procedure between Eqs. 3.30 and 3.32 is that for the latter, the substitution from k to k' was $k = \frac{k'q}{2}$, and the upper-bound in k, being finite in this case, has resultantly changed from μ to $\frac{2\mu}{q}$.[7] This integral can be

[7]The upper-bound of the φ integral has also changed utilizing the fact that the integrand is even around π, so the region of integration from π to 2π simply results in a factor of 2.

done analytically unlike the other, first by performing the integral over φ,

$$\begin{aligned}
\chi_\mu(\boldsymbol{q}) &= -\frac{q}{2}\int_0^{\frac{2\mu}{q}} dk' \left[\varphi + 2\sqrt{k'^2-1}\,\operatorname{arctanh}\left(\sqrt{\frac{k'-1}{k'+1}}\tan\frac{\varphi}{2}\right)\right]_0^{\pi} \\
&= -\frac{q}{2}\int_0^{\frac{2\mu}{q}} dk'\pi - \frac{q}{2}\int_0^{\frac{2\mu}{q}} dk' 2\sqrt{k'^2-1}\frac{i\pi}{2} \\
&= -\frac{q}{2}\frac{2\mu}{q}\pi - \frac{iq\pi}{2}\left[\frac{k'}{2}\sqrt{k'^2-1} - \frac{1}{2}\ln\left(k' + \sqrt{k'^2-1}\right)\right]_0^{\frac{2\mu}{q}} \\
\chi_\mu(\boldsymbol{q}) &= -\pi\mu - \frac{q\pi}{4}\left[k'\sqrt{1-k'^2} - i\ln\left(k' + i\sqrt{1-k'^2}\right)\right]_0^{\frac{2\mu}{q}}. \qquad (3.33)
\end{aligned}$$

From here, the natural log can be simplified by first writing the argument in terms of polar coordinates, $k' = r\cos\theta \Rightarrow \sqrt{1-k'^2} = r\sin\theta$, so

$$\begin{aligned}
-i\ln\left(k' + i\sqrt{1-k'^2}\right) &= -i\ln\left(r\cos\theta + ir\sin\theta\right) \\
&= -i\ln re^{i\theta} \\
&= -i\ln r - i(i\theta) \\
-i\ln\left(k' + i\sqrt{1-k'^2}\right) &= -i\ln r + \theta,
\end{aligned}$$

consider that $\theta = \arccos\frac{k'}{r}$, and $r = \sqrt{k'^2+1=k'^2} = 1$, so

$$-i\ln\left(k' + i\sqrt{1-k'^2}\right) = \arccos k'.$$

This relation is only possible when the argument of a natural log is complex, but if $1-k'^2 < 1$, then the argument is entirely real and this relation is no longer valid. The addition of a step-function resolves this issue however,

$$-i\ln\left(k' + i\sqrt{1-k'^2}\right) = \Theta(1-k'^2)\arccos k', \qquad (3.34)$$

and since $k'^2 \leq 1 \Rightarrow k' \leq 1$, and $k'^2 \geq 1 \Rightarrow k' \geq 1$ it is valid to say that $\Theta(1-k'^2) = \Theta(1-k')$. Make the substitution of Eq. 3.34 back into Eq. 3.33,

$$\chi_\mu(\boldsymbol{q}) = -\pi\mu - \frac{q\pi}{4}\left[k'\sqrt{1-k'^2} + \Theta(1-k')\arccos k'\right]_0^{\frac{2\mu}{q}},$$

because of the step function this equation has a discontinuity at $k' = 1$, so the evaluation must be split between a region below 1 (1^-), and another above 1 (1^+),

$$\chi_\mu(\boldsymbol{q}) = -\pi\mu - \frac{q\pi}{4}\left[\left[k'\sqrt{1-k'^2} + \Theta(1-k')\arccos k'\right]_0^{1^-} + \left[k'\sqrt{1-k'^2} + \Theta(1-k')\arccos k'\right]_{1^+}^{\frac{2\mu}{q}}\right]. \tag{3.35}$$

Equation 3.35 marks an important distinction in the value of $\frac{2\mu}{q}$; if $\frac{2\mu}{q} > 1$ then the second term in Eq. 3.35 becomes complex, but if $\frac{2\mu}{q} < 1$ then, with a sign change, the bounds of the second term can be flipped and both terms will be real. An equivalent way to define these two cases are whether $q < 2\mu$ or $q > 2\mu$ respectively, and so the discontinuity in the natural log of Eq. 3.33 at $k' = 1$ manifests itself as a discontinuity at $q = 2\mu$. This nonanalyticity in the polarization at $q = 2\mu$ will become very important in the calculation of the charge density.

First, the case where $q > 2\mu$; both terms can be evaluated by flipping the sign and the bounds of the second term,

$$\begin{aligned}
\chi_\mu(\boldsymbol{q}) &= -\pi\mu - \frac{q\pi}{4}\left[\left[k'\sqrt{1-k'^2} + \Theta(1-k')\arccos k'\right]_0^{1} - \left[k'\sqrt{1-k'^2} + \Theta(1-k')\arccos k'\right]_{\frac{2\mu}{q}}^{1}\right] \\
&= -\pi\mu - \frac{q\pi}{4}\left[-\pi - \arccos 0 - \frac{2\mu}{q}\sqrt{1-\left(\frac{2\mu}{q}\right)^2} - \arccos\frac{2\mu}{q}\right] \\
\chi_\mu(\boldsymbol{q}) &= -\pi\mu + \frac{q\pi}{4}\left[\frac{\pi}{2} + \frac{2\mu}{q}\sqrt{1-\left(\frac{2\mu}{q}\right)^2} + \arccos\frac{2\mu}{q} + \pi\right]
\end{aligned}$$

using the identity, $\arccos x + \pi = -\arccos x$,

$$\chi_\mu(\boldsymbol{q}) = -\pi\mu + \frac{q\pi^2}{8} + \frac{q\pi}{4}\left[\frac{2\mu}{q}\sqrt{1-\left(\frac{2\mu}{q}\right)^2} - \arccos\frac{2\mu}{q}\right]$$
$$\chi_\mu(\boldsymbol{q}) = -\pi\mu + \frac{q\pi^2}{8} + \frac{q\pi}{4}G\left(\frac{2\mu}{q}\right), \tag{3.36}$$

where the function $G(x)$ has been defined as

$$G(x) = x\sqrt{1-x^2} - \arccos x. \tag{3.37}$$

In a similar manner, the case $q < 2\mu$ yields the same solution as Eq. 3.36 omitting the term involving G. So once again the discontinuity is captured nicely by the inclusion of a step function,

$$\chi_\mu(\boldsymbol{q}) = -\pi\mu + \frac{q\pi^2}{8} + \frac{q\pi}{4}G\left(\frac{2\mu}{q}\right)\Theta(q-2\mu) \tag{3.38}$$

All that is left is to substitute Eq. 3.38 and Eq. 3.31 into Eq. 3.29,

$$\Pi(\boldsymbol{q}) = \frac{2g_s g_v}{4\pi^2 v_x v_y}\left[\chi_\mu(\boldsymbol{q}) - \chi_\infty^{--}\right]$$
$$= \frac{2g_s g_v}{4\pi^2 v_x v_y}\left[-\pi\mu + \frac{q\pi^2}{8} + \frac{q\pi}{4}G\left(\frac{2\mu}{q}\right)\Theta(q-2\mu) - \frac{q\pi^2}{8}\right]$$
$$\Pi(\boldsymbol{q}) = \frac{g_s g_v}{2\pi v_x v_y}\left[-\mu + \frac{q}{4}G\left(\frac{2\mu}{q}\right)\Theta(q-2\mu)\right],$$

since the prefactor of $\hbar$ was omitted earlier, recalling the long list of redefinitions, $q \equiv |\boldsymbol{q}| \equiv |\widetilde{\boldsymbol{q}}| = \sqrt{v_x^2 q_x^2 + v_y^2 q_y^2} = \epsilon_{\boldsymbol{q}}$,

$$\Pi(\boldsymbol{q}) = \frac{g_s g_v}{2\pi v_x v_y}\left[-\mu + \frac{\epsilon_{\boldsymbol{q}}}{4}G\left(\frac{2\mu}{\epsilon_{\boldsymbol{q}}}\right)\Theta(\epsilon_{\boldsymbol{q}} - 2\mu)\right], \tag{3.39}$$

which is the final form of the polarization function in strained graphene.

Chapter 4

Charge Distribution for Doped Graphene Under Strain

With the polarization function (Eq. 3.39) in an exact form, the way in which charges respond to an external Coulomb impurity with charge, $Z|e|$, in strained graphene can be characterized. In the limit of linear response, i.e. neglecting the effect of electron-electron (e-e) interactions the charge distribution that forms in response to a potential field $V(\boldsymbol{q})$ is from Eq. 3.2, but when e-e interactions are taken into account, an extra factor appears in the expression,

$$n(\boldsymbol{q}) = Z\frac{\Pi(\boldsymbol{q})V(\boldsymbol{q})}{1-\Pi(\boldsymbol{q})V(\boldsymbol{q})},$$

which is a textbook equation. The numerator is the linear response effect, and the denominator is the dielectric function[5], or screened response; the ratio of the two is the total charge density response to an impurity. The above equation gives the polarization charge density in momentum space, but finding n in real space is as

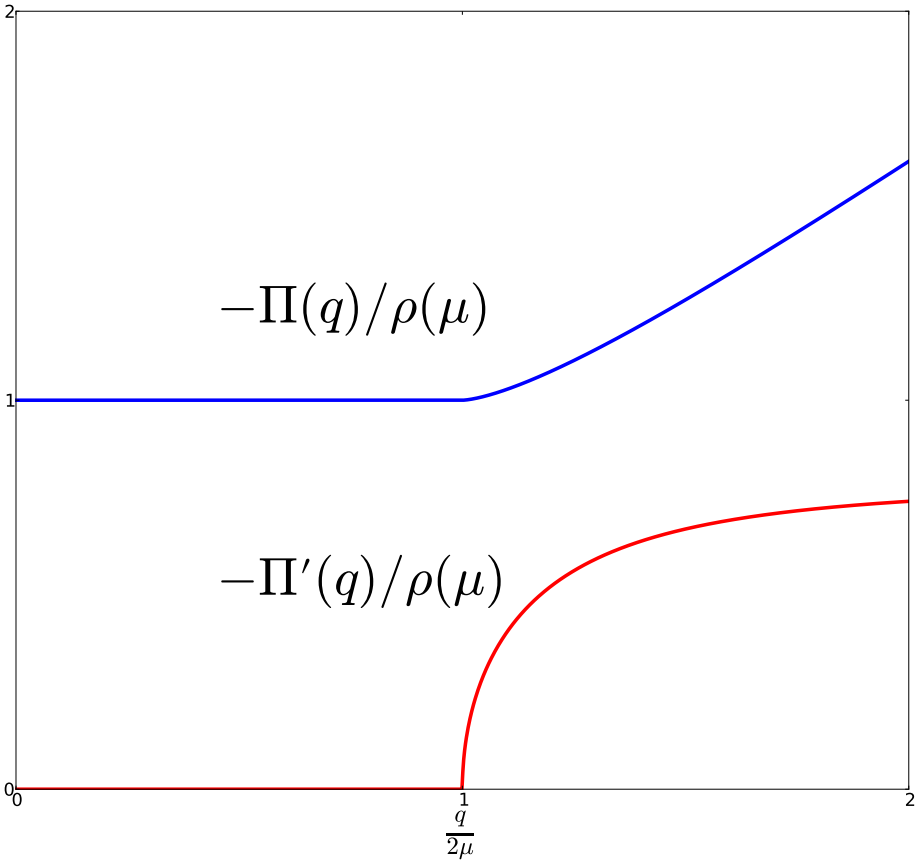

Figure 4.1: Plot of the polarization function as it appears in Eq. 3.39 (in blue) and its first derivative (in red). Each are normalized by the density of states at the Fermi level $\rho(\mu) = \frac{g_s g_v \mu}{2\pi v_x v_y}$. The vertical units are arbitrary, but the horizontal axis is in units of 2μ, so the discontinuity occurs at $\frac{q}{2\mu} = 1$.

simple as taking an inverse Fourier transform,

$$n(\boldsymbol{r}) = Z \int\limits_{q<\infty} \frac{d^2q}{4\pi^2} \frac{e^{i\boldsymbol{q}\cdot\boldsymbol{r}}\Pi(\boldsymbol{q})V(\boldsymbol{q})}{1-\Pi(\boldsymbol{q})V(\boldsymbol{q})}. \tag{4.1}$$

While the inverse Fourier transform in Eq. 4.1 is simple conceptually, with a form of the polarization as complex as that in Eq. 3.39, actually evaluating this integral can be anything but simple. There are several things that may be gleaned about the form of $n(\boldsymbol{r})$ without having to perform the integral explicitly. First,

and arguably most significantly are the presence of Friedel oscillations. The discontinuity in the polarization at $q = 2\mu$ becomes very important when evaluating the inverse Fourier transform, and so it pays to understand a little more about that discontinuity. Figure 4.1 shows the polarization as it appears in Eq. 3.39 and the first derivative of the polarization. While the polarization does make a clear transition from a constant value to a linear function in q at $\frac{q}{2\mu} = 1$, it is still continuous. Rather, the true discontinuity at $q = 2\mu$ occurs in the first derivative of the polarization. This is significant because a property of nonanalytic functions, is that their Fourier transforms take the form of oscillations that decay as a power law. In screening these are known as Friedel oscillations. While the polarization in graphene is entirely analytic, the first derivative is not, and so it is expected that

$$n(\boldsymbol{r}) \sim \frac{\cos \omega r}{r^3}, \tag{4.2}$$

which is the generic form of Friedel oscillations[11], and they have been observed in this form for the case of unstrained graphene[12]. Friedel oscillations are a result of the quantum mechanical nature of electrons. Being described by wavefunctions, instead of as point charges, allows for overlap of electron states as they move to screen an impurity. These overlaps result in regions of constructive and destructive interference giving rise to oscillations in the charge density. Friedel oscillations are not a mathematical oddity, but are, in fact, a measurable effect[14]. While the charge density of Eq. 4.1 for the specific polarization in Eq. 3.39 is expected to take the generic form of Eq. 4.2, nothing is yet known about the specific function. To move forward the exact integrand must be considered, which has no known analytic solution, but it can be simplified by means of the stationary phase approximation.

4.1 The Stationary Phase Approximation

Given an impurity of the form $Z|e|$, the Coulomb potential that must be screened takes the form

$$V(\boldsymbol{q}) = \frac{2\pi e^2}{q},$$

so consider the term $\Pi(\boldsymbol{q})V(\boldsymbol{q})$, which appears twice in Eq. 4.1, with this potential and the specific form of the polarization from Eq. 3.39,

$$\Pi(\boldsymbol{q})V(\boldsymbol{q}) = \frac{g_s g_v}{2\pi v_x v_y}\left[-\mu + \frac{\epsilon_{\boldsymbol{q}}}{4}G\left(\frac{2\mu}{\epsilon_{\boldsymbol{q}}}\right)\Theta(\epsilon_{\boldsymbol{q}} - 2\mu)\right]\frac{2\pi e^2}{q},$$

using $g_s = g_v = 2$, and simplifying,

$$\Pi(\boldsymbol{q})V(\boldsymbol{q}) = \frac{e^2}{qv_x}\left[-\frac{2\mu}{v_y} + \frac{\epsilon_{\boldsymbol{q}}}{2v_y}G\left(\frac{2\mu}{\epsilon_{\boldsymbol{q}}}\right)\Theta\left(\frac{\epsilon_{\boldsymbol{q}}}{2\mu} - 1\right)\right],$$

define an effective e-e parameter $\alpha = \frac{e^2}{v_x}$; this is a common definition[12] that will be shown to govern the strength of e-e interactions. In addition, use $\epsilon_{\boldsymbol{q}} = v_x\sqrt{q_x^2 + \left(\frac{v_y}{v_x}\right)^2 q_y^2}$, and let $\hbar = 1$ for the remainder of the derivation,

$$\Pi(\boldsymbol{q})V(\boldsymbol{q}) = \frac{\alpha}{q}\left[-\frac{2\mu}{v_y} + \frac{v_x\sqrt{q_x^2 + \frac{v_y}{v_x}^2 q_y^2}}{2v_y}G\left(\frac{2\mu}{v_x\sqrt{q_x^2 + \frac{v_y}{v_x}^2 q_y^2}}\right)\Theta\left(\frac{v_x\sqrt{q_x^2 + \frac{v_y}{v_x}^2 q_y^2}}{2\mu} - 1\right)\right],$$

recognize that $k_F = \frac{\mu}{v_x}$, the Fermi momentum,[1]

$$\Pi(\boldsymbol{q})V(\boldsymbol{q}) = \frac{\alpha}{q}\left[-\frac{2k_F v_x}{v_y} + \frac{v_x\sqrt{q_x^2 + \frac{v_y}{v_x}^2 q_y^2}}{2v_y}G\left(\frac{2k_F}{\sqrt{q_x^2 + \frac{v_y}{v_x}^2 q_y^2}}\right)\Theta\left(\frac{\sqrt{q_x^2 + \frac{v_y}{v_x}^2 q_y^2}}{2k_F} - 1\right)\right].$$

The ratio $\frac{v_y}{v_x}$ appears often, so it is reasonable to redefine that value to be $v_\perp$, which will determine the strength of the strain applied to the lattice. As previously men-

[1] In a Lorentz-invariant system, $\epsilon_F = m^* k_F$, where m^* is the effective mass. In graphene, $\epsilon_{\boldsymbol{q}} = v_F q$, so $m^* = \frac{d\epsilon_q}{dq} = v_F$. So, $k_F = \frac{\mu}{v_F}$. The choice of v_x is arbitrary.

tioned, the strain will be applied in the armchair direction, which will decrease v_y while v_x remains essentially unchanged. So the greater strain corresponds to smaller values of $v_\perp$. With this definition,

$$\Pi(\boldsymbol{q})V(\boldsymbol{q}) = \frac{\alpha}{q}\left[-\frac{2k_F}{v_\perp} + \frac{\sqrt{q_x^2 + v_\perp^2 q_y^2}}{2v_\perp} G\left(\frac{2k_F}{\sqrt{q_x^2 + v_\perp^2 q_y^2}}\right)\Theta\left(\frac{\sqrt{q_x^2 + v_\perp^2 q_y^2}}{2k_F} - 1\right)\right].$$

The next step is to convert from cartesian $\boldsymbol{q}$ to polar, so $q_x = q\cos\phi$, and $q_y = q\sin\phi$, and let $q\sqrt{\cos^2\phi + v_\perp^2\sin^2\phi} = qs(\phi, v_\perp)$, where $s(\phi, v_\perp) = \sqrt{\cos^2\phi + v_\perp^2\sin^2\phi}$,

$$\Pi(\boldsymbol{q})V(\boldsymbol{q}) = \frac{\alpha}{qv_\perp}\left[-2k_F + \frac{qs(\phi, v_\perp)}{2} G\left(\frac{2k_F}{qs(\phi, v_\perp)}\right)\Theta\left(\frac{qs(\phi, v_\perp)}{2k_F} - 1\right)\right]. \quad (4.3)$$

Use Eq. 4.3 in Eq. 4.1,

$$n(\boldsymbol{r}) = Z\frac{\alpha}{v_\perp}\int_0^\infty\int_0^{2\pi}\frac{dqd\phi}{4\pi^2}q\frac{e^{i\boldsymbol{q}\cdot\boldsymbol{r}}\frac{1}{q}\left[-2k_F + \frac{qs(\phi,v_\perp)}{2}G\left(\frac{2k_F}{qs(\phi,v_\perp)}\right)\Theta\left(\frac{qs(\phi,v_\perp)}{2k_F} - 1\right)\right]}{1 - \frac{\alpha}{qv_\perp}\left[-2k_F + \frac{qs(\phi,v_\perp)}{2}G\left(\frac{2k_F}{qs(\phi,v_\perp)}\right)\Theta\left(\frac{qs(\phi,v_\perp)}{2k_F} - 1\right)\right]},$$

make the substitution $Q = \frac{qs(\phi,v_\perp)}{2k_F}$ and simplify to get

$$n(\boldsymbol{r}) = Z\frac{2\alpha k_F^2}{v_\perp}\int_0^\infty\int_0^{2\pi}\frac{dQd\phi}{4\pi^2 s(\phi, v_\perp)}\frac{e^{i\boldsymbol{q}\cdot\boldsymbol{r}}\left[-2 + QG\left(\frac{1}{Q}\right)\Theta\left(Q-1\right)\right]}{1 + \frac{2\alpha s(\phi,v_\perp)}{Qv_\perp} - \frac{\alpha s(\phi,v_\perp)}{v_\perp}G\left(\frac{1}{Q}\right)\Theta(Q-1)}$$

Finally, consider the transition to polar coordinates with respect to the dot product $\boldsymbol{q}\cdot\boldsymbol{r}$,

$$\begin{aligned}\boldsymbol{q}\cdot\boldsymbol{r} &= xq\cos\phi + yq\sin\phi \\ &= \frac{q}{k_F}(k_F x\cos\phi + k_F y\sin\phi) \\ \boldsymbol{q}\cdot\boldsymbol{r} &= \frac{2Q}{s(\phi, v_\perp)}(X\cos\phi + Y\sin\phi),\end{aligned}$$

where the dimensionless quantities $X = k_F x$ and $Y = k_F y$ have been defined. For simplicity, let $\boldsymbol{q} \cdot \boldsymbol{r} = F(Q, \phi, X, Y, v_\perp)$, so

$$n(\boldsymbol{r}) = Z\frac{4\alpha k_F^2}{v_\perp}\int_0^\infty \int_0^\pi \frac{dQd\phi}{4\pi^2 s(\phi, v_\perp)} \frac{e^{iF(Q,\phi,X,Y,v_\perp)}\left[-2 + QG\left(\frac{1}{Q}\right)\Theta\left(Q-1\right)\right]}{1 + \frac{2\alpha s(\phi,v_\perp)}{Qv_\perp} - \frac{\alpha s(\phi,v_\perp)}{v_\perp}G\left(\frac{1}{Q}\right)\Theta(Q-1)}, \quad (4.4)$$

where the fact that the integrand is even around π has been utilized. Equation 4.4 has no known analytic solution, and so a closed form for $n(\boldsymbol{r})$ may not be possible. The only avenue, thus, is numerical evaluation. Evaluating Eq. 4.4 once gives n at exactly one position (X, Y), and to have a complete plot of $n(\boldsymbol{r})$ this integral must be evaluated hundreds of times. The problem is that the integrand is highly oscillatory in both Q and ϕ, and the integral is two-dimensional, each fact making numerics difficult and time-consuming. On the otherhand, Eq. 4.4 is a Fourier integral, and especially as Q grows large, the integrand has regions of slower oscillation and highly rapid oscillation over the domain $\phi = [0, \pi]$ as shown in Fig. 4.2. Because of this, it is reasonable to anticipate that the value of the integral will be dominated by the integration near the region of slower oscillation, or rather, the region of slower phase variation.

The point around which phase variation goes to zero is known as the saddle point, and is given by extremizing the function in the exponential,

$$\left.\frac{\partial F}{\partial \phi}\right|_{\phi_0} = 0. \quad (4.5)$$

If the integral is dominated by the region near $\phi = \phi_0$, then the integrand can be approximated by performing an expansion of F near the saddle point, truncated after second order,

$$F(\phi) \approx F(\phi_0) + \frac{1}{2}\left.\frac{\partial^2 F}{\partial \phi^2}\right|_{\phi_0}(\phi - \phi_0)^2. \quad (4.6)$$

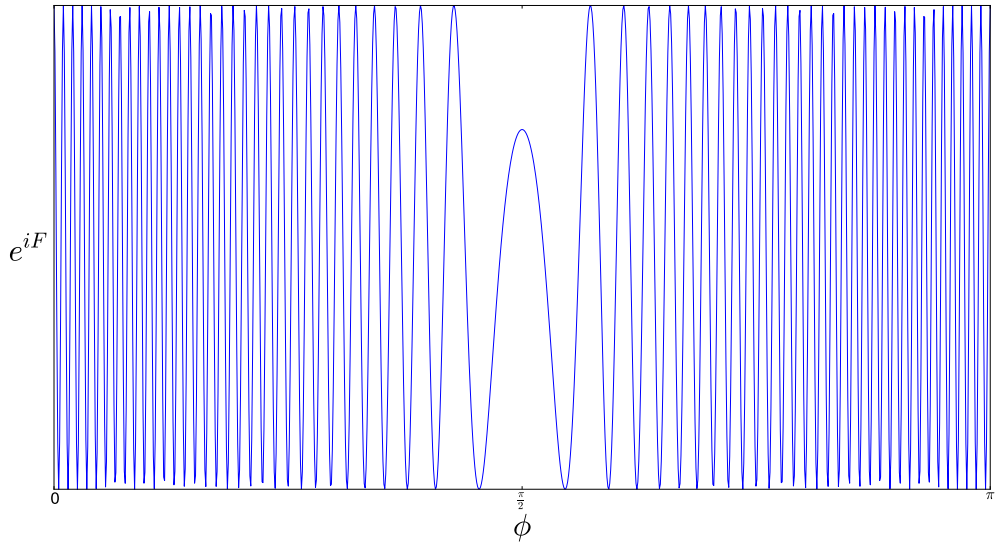

Figure 4.2: Plot of the complex exponential in Eq. 4.4, e^{iF}, at $Q = 100$, $Y = 0$, $X = 1$, and $v_\perp = 1$, over the domain $[0, \pi]$. The saddle point ϕ_0 along this direction is at $\frac{\pi}{2}$, and the region near the saddle point oscillates more slowly and is, thus, the main contribution to the evaluation of the integral. This is the idea behind the method of stationary phase.

So labeling everything (including constants) besides the exponential in Eq. 4.4 as $f(Q, \phi)$, which will be evaluated at the saddle point, and using the prime-notation for derivatives, the integral approximates to

$$n(\boldsymbol{r}) \approx \int_0^\infty dQ f(Q, \phi_0) \int_0^\pi d\phi e^{i\left(F(\phi_0) + \frac{1}{2}F''(\phi_0)(\phi-\phi_0)^2\right)}.$$

Though it has been omitted in the notation, $F(\phi_0)$ is still a function of Q so it must remain in the Q integral.

$$n(\boldsymbol{r}) \approx \int_0^\infty dQ e^{iF(\phi_0)} f(Q, \phi_0) \int_0^\pi d\phi e^{i\frac{1}{2}F''(\phi_0)(\phi-\phi_0)^2}.$$

In this form, the integral appears to be in the form of a Gaussian over ϕ. To show this more explicitly, make the substitution $\Psi = \sqrt{\frac{1}{2}F''(\phi_0)}(\phi - \phi_0)$, and let $\beta =$

$\text{sign}(F''(\phi_0))$,

$$n(\boldsymbol{r}) \approx \sqrt{2}\int_0^\infty dQ \frac{e^{iF(\phi_0)}}{\sqrt{|F''(\phi_0)|}} f(Q,\phi_0)\int_0^C d\Psi e^{\beta i \Psi^2},$$

where $C = \sqrt{\frac{1}{2}F''(\phi_0)}(\pi - \phi_0)$, which is very large and so can be approximated to approach infinity. The integrand is also even, thus,

$$n(\boldsymbol{r}) \approx \sqrt{\frac{1}{2}}\int_0^\infty dQ \frac{e^{iF(\phi_0)}}{\sqrt{|F''(\phi_0)|}} f(Q,\phi_0)\int_{-\infty}^\infty d\Psi e^{\beta i \Psi^2}.$$

The evaluation of the Gaussian is textbook,

$$n(\boldsymbol{r}) \approx \sqrt{\frac{\pi}{-2\beta i}}\int_0^\infty dQ \frac{e^{iF(\phi_0)}}{\sqrt{|F''(\phi_0)|}} f(Q,\phi_0),$$

rewrite $(-\beta i)^{-\frac{1}{2}} = e^{i\beta\frac{\pi}{4}}$, leaving

$$n(\boldsymbol{r}) \approx e^{i\beta\frac{\pi}{4}}\sqrt{\frac{\pi}{2}}\int_0^\infty dQ \frac{e^{iF(\phi_0)}}{\sqrt{|F''(\phi_0)|}} f(Q,\phi_0). \tag{4.7}$$

This entire procedure is quite general and is known as the method of stationary phase[15]; Equation 4.7 is likewise called the stationary phase approximation. The advantage to this approximation is clear, without the integral over ϕ, the charge density can be evaluated as a single-dimensional integral, making numerics much easier. Applying the exact form of the function F to Eq. 4.7 is straightforward, but tedious, algebra-laden, and not particularly elucidating, so it will not be shown here. Another barrier to showing a full derivation for this particular case is that there will be a different saddle point for every pair of coordinates (X, Y), there is no general expression for ϕ_0 as a function of X and Y. Each saddle point must also be found numerically before the integral is performed, but that has a much lower numeric cost than integrating over ϕ.

4.2 Results of Numerical Evaluation

Restoring $f(Q,\phi)$, the integral to be numerically evaluated is[2]

$$\frac{\pi^2 n(\boldsymbol{r})}{Zk_F^2} = \sqrt{\frac{\pi}{2}}\frac{\alpha e^{i\beta\frac{\pi}{4}}}{v_\perp s(\phi_0,v_\perp)}\int_0^\infty dQ \frac{e^{iF(\phi_0)}}{\sqrt{|F''(\phi_0)|}}\frac{\left[-2+QG\left(\frac{1}{Q}\right)\Theta\left(Q-1\right)\right]}{1+\frac{2\alpha s(\phi_0,v_\perp)}{Qv_\perp}-\frac{\alpha s(\phi_0,v_\perp)}{v_\perp}G\left(\frac{1}{Q}\right)\Theta(Q-1)}, \tag{4.8}$$

remembering that both $F(\phi_0)$ and $F''(\phi_0)$ are functions[3] of Q, X and Y. There are two factors that can be systematically changed to produce different results that are physically meaningful: α and $v_\perp$.

The first, α is an overall prefactor to the integration, altering the amplitude of the oscillations expected by Eq. 4.2, but it also appears as a coefficient of two of the three terms in the denominator of the integrand. If $\alpha = 0$, then $n(\boldsymbol{r})$ becomes, reducing back to the general form of Eq. 4.1,

$$\lim_{\alpha\to 0} n(\boldsymbol{r}) = Z\int\limits_{q<\infty}\frac{d^2q}{4\pi^2}e^{i\boldsymbol{q}\cdot\boldsymbol{r}}\Pi(\boldsymbol{q})V(\boldsymbol{q}),$$

which is the limit of no e-e interactions. Thus α, as stated before, is an effective e-e interaction term; increasing α increases the strength of e-e interactions, while decreasing α decreases the strength of e-e interactions. Accepted values of α for graphene are a little more than 2[12]. The second, $v_\perp$, the ratio of v_y and v_x was explained before as the degree of strain. The strain is being applied along the armchair direction[4], and so v_y decreases as strain increases. A maximum value of $v_\perp = 1$ corresponds to no strain, and the screening density for unstrained graphene has been

[2]It merits pointing out that, because of the step function, this integral is actually two: one over the domain $Q = [0,1]$ where the G functions disappear, and another from $Q = [1,\infty)$ where the step function evaluates to 1. It is the addition of these two integrals that results in the correct charge density $n(\boldsymbol{r})$.

[3]The functions are explicitly linear in all three, but since ϕ_0 itself depends on the coordinates X and Y, the actual dependence on those two is much harder to define.

[4]See Fig. 1.1

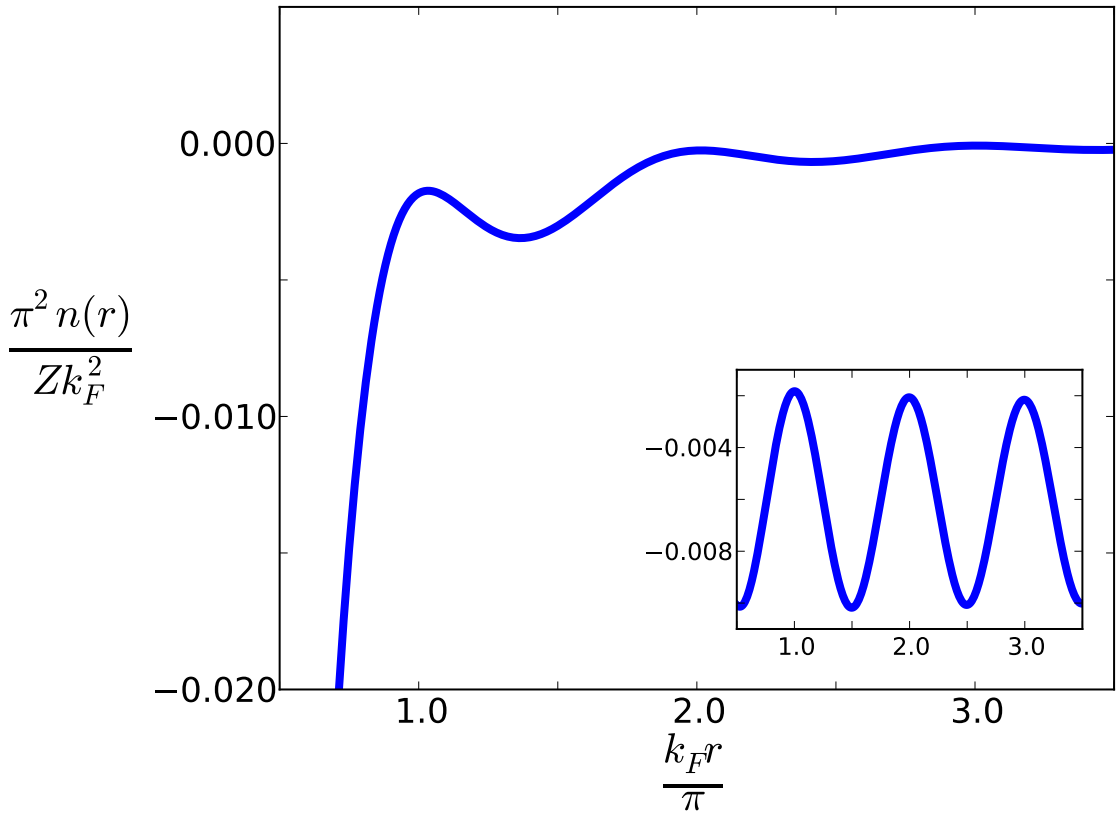

Figure 4.3: Plot of the polarization charge density when graphene is unstrained, $v_\perp = 1$. The distance is in units of π, because the periodicity of the unstrained case is in intervals of π. The inset plot is the charge density multiplied by r^3 showing only the oscillations without the power-law decay. The e-e parameter α is 1.

previously documented[12].

The unstrained case, given that there is a previous and independently achieved result, will be used as the control case, and is shown in Fig. 4.3. This plot, found directly by numerical evaluation of Eq. 4.8, matches very well to the behavior shown in Wunsch, Stauber, Sols, and Guinea: the periodicity is in intervals of π, the first peak occurs at $\frac{k_F r}{\pi} = 1$, and, perhaps most importantly, the charge density never crosses above zero. For all distances, the positive Coulomb impurity is screened by a negative distribution of charge. The density exhibits both the oscillations, and the r^{-3} decay predicted by the generic form of Eq. 4.2, as shown in the inset. The inset plot is the same data as in the main plot multiplied by r^3, and shows that

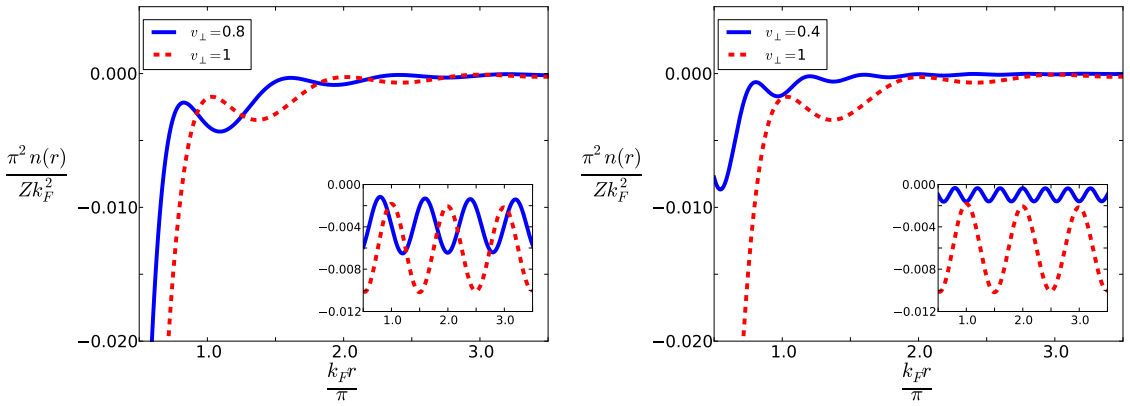

(a) (b)

Figure 4.4: Polarization charge density along the armchair direction for e-e parameter $\alpha = 2.2$. Two different degrees of strain are shown: (a) $v_\perp = 0.8$, and (b) $v_\perp = 0.4$. The strained densities are shown in the blue, solid line, while the control case of the unstrained density is shown in the dashed red line. The period and amplitude of oscillations both decrease dramatically, and the overall charge density is much lower than the unstrained case.

without that decay, the amplitude of the oscillations remain stable, meaning there is no other decay in the charge density. This rescaled density also shows that the period of oscillation is stable at π. With the unstrained charge density verified, the method of analysis can be considered valid, and the charge density under strain can be investigated.

When considering the density of strained graphene, the direction must be taken into account, and so the charge density will be mainly evaluated along the the zig-zag (or x) direction and along the armchair (or y) direction individually. It will be shown that the behavior at these two extremes adequately characterizes the density over all space, as every direction between the zig-zag and armchair direction will exhibit some intermediate behavior. Along the armchair direction, the Fermi velocity becomes relatively small as strain increases, making it more difficult for electrons to transport along the armchair direction. Thus, one would expect the density to diminish, and that is exactly what is seen in Fig. 4.4.

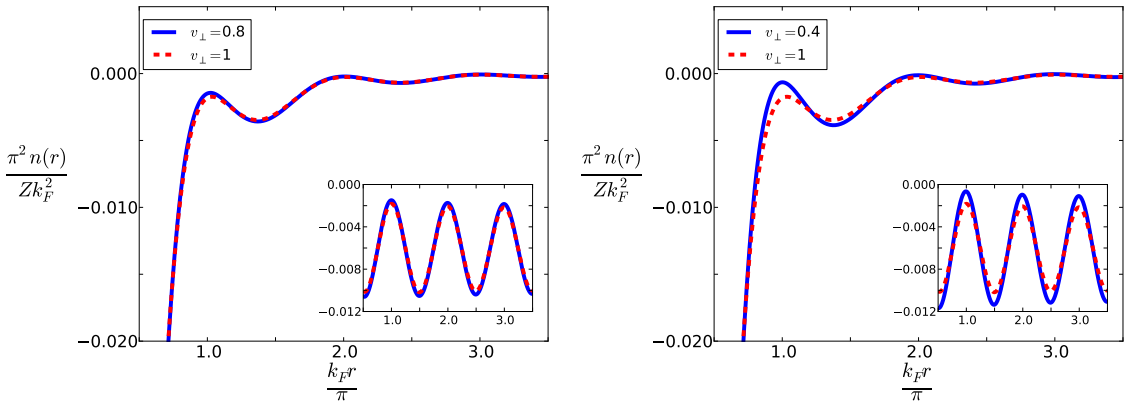

(a) (b)

Figure 4.5: Polarization charge density along the zig-zag direction for e-e parameter $\alpha = 2.2$. Two different degrees of strain are shown: (a) $v_\perp = 0.8$, and (b) $v_\perp = 0.4$. The strained densities are shown in the blue, solid line, while the control case of the unstrained density is shown in the dashed red line. The frequency and decay rate of oscillations remain unchanged, but the amplitude of oscillations increases noticeably.

Even at a reasonable degree of strain, $v_\perp = 0.8$ in Fig. 4.4 (a), which corresponds to about an 8% strain[16], the effects are already very evident. The inset shows clearly a decrease in amplitude compared to the unstrained case, but also, interestingly, a decrease in period as well; three peaks appear in the unstrained plot, while there are four on the same interval when graphene is strained. The first peak shown in the plot is the first peak that appears in the charge density, so this is not an apparent effect from something else like a phase shift. In the more extreme case of $v_\perp = 0.4$ (about 25% strain) in Fig. 4.4 (b) the effect is significantly more pronounced. Not only is the amplitude of oscillation much smaller, but the charge density as a whole is significantly lower, and yet still decays at the expected rate of r^{-3} and never crosses zero. The decrease in period seen in Fig. 4.4 (a) is also, clearly, enhanced. The lower charge density, may, in part, explain the change in frequency. Fewer electrons means fewer interfering wavefunctions leaving more frequent, smaller peaks in the charge density.

Along the zig-zag direction the Fermi velocity hardly changes at all, and

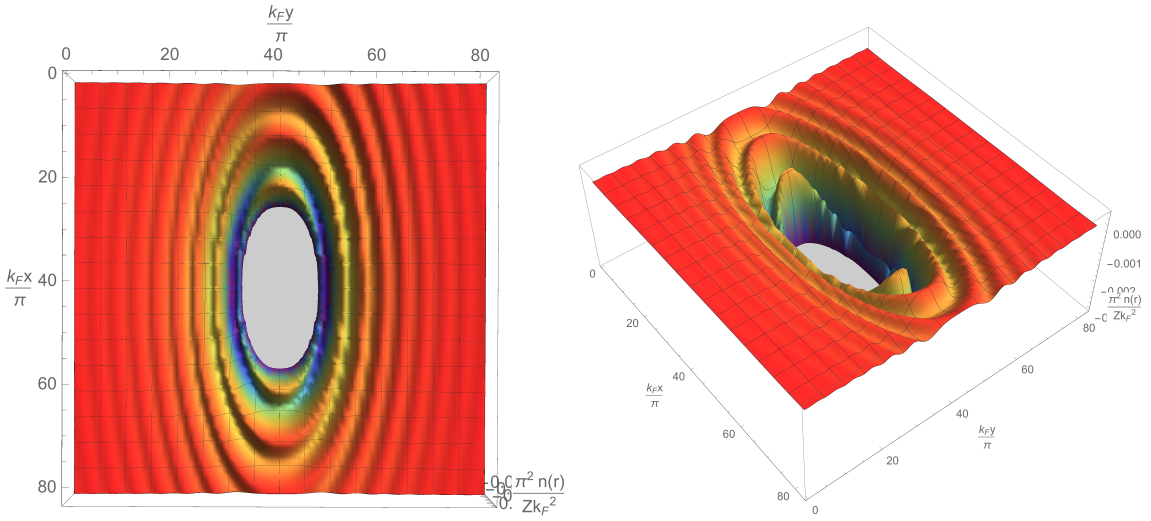

(a) (b)

Figure 4.6: The full polarization charge distribution around a Coulomb impurity. Figure (a) is the view from above, and figure (b) is from an angle. The higher frequency and lower amplitudes along the armchair direction can be clearly seen in both figures.

so one would expect the response of electrons along the zig-zag direction to remain largely unchanged from the unstrained case. However, there is, quite unexpectedly, a significant change in the charge density both at a reasonable degree of strain, $v_\perp = 0.8$, and at the more intense $v_\perp = 0.4$, each shown in Fig. 4.5. In each case, the period of oscillations remains unaltered at π, the decay still occurs as r^{-3}, and the density remains below zero, but the amplitude of oscillation increase slightly at both levels of strain. Even the relatively weak $v_\perp = 0.8$ shows a noticeable, albeit not striking, increase in amplitude of the oscillations. Like the changes in the armchair direction, the affect of strain is increased with the intensity of strain along the zig-zag direction; a strain of $v_\perp = 0.4$ exhibits a very large increase in amplitude, and the magnitude of this increase, judging by the inset, remains constant at all distances.

This effect is very interesting an unexpected since the changes in the lattice along the zig-zag direction are very minimal when strain is applied along the arm-chair direction. However, the total polarization charge density must be enough to

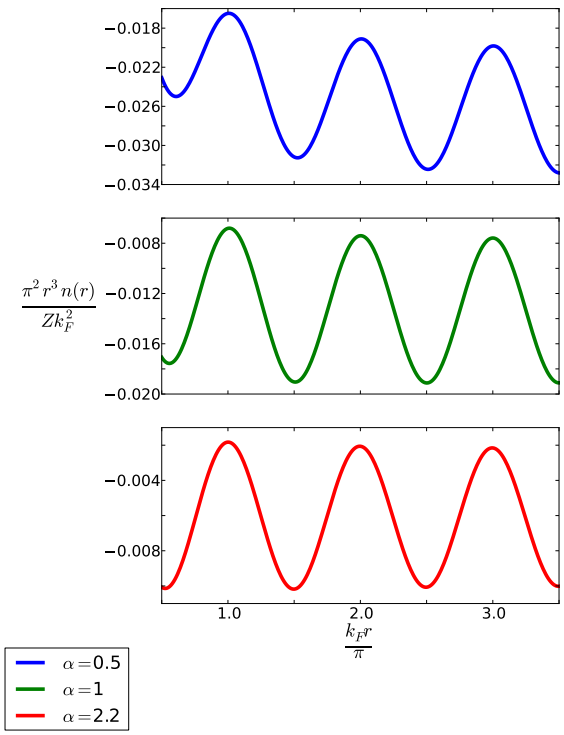

Figure 4.7: Variation of the e-e parameter α from 0.5 to 1, to the more physically realistic 2.2. Each plot is made for the unstrained case, $v_\perp = 1$, and is scaled by r^3 like the insets of Figs. 4.4 and 4.5.

completely screen an impurity charge. Since the density along the armchair direction decreases, it would seem that instead of the density decaying more slowly (meaning higher relative densities at larger distances), the excess charge polarizes along the zig-zag direction leading to slightly greater density amplitudes in that direction. It should be noted that this is entirely speculation.

While in principle, every direction between the zig-zag and the armchair direction does produce a unique charge density, these two directions showcase the extreme behavior of the distribution. Figure 4.6 shows a complete two-dimensional contour plot of the distribution. The anisotropy of the charge distribution is very evident in the elliptical nature of $n(\boldsymbol{r})$, but there are no extra lobes or unique angular regions around the origin that would require a more thorough analysis of the distribution's directionality. So it is a reasonable conclusion to say that the behavior

along the zig-zag and armchair fully characterize the distribution as a whole.

The effect of altering α, shown in Fig. 4.7 is less evident than increasing strain, but still noticeable. First, the overall density and the amplitude of oscillation decrease significantly between $\alpha = 0.5$ and $\alpha = 2.2$. The period of the oscillations appear unaffected, but the decay rate does seem to have some dependence on α. While in each case, the amplitude becomes stable eventually, at lower α, there is some transient behavior, deviating from the r^{-3} decay at distances close to the impurity. For very weak e-e interactions, $\alpha = 0.5$, these transients remain until $\frac{k_F r}{\pi} \approx 2.5$, which is significant because by this distance the density has almost completely decayed. These effects are essentially the same for each direction and each degree of strain.

Chapter 5

Extreme Strain to the point of Dirac Point Merger

With a degree of strain even as intense as 25%, which would be very difficult to achieve in a lab, the Dirac cones become highly elliptic, but the band structure of graphene does not fundamentally change in any way. Strain, will, of course, increase the *NN* lattice vectors along the direction of strain, and by increasing the *NN* lattice vectors, the hopping parameter t is no longer a constant, but rather depends on the specific pair of *NN* atoms in the strained lattice. This is especially important when considering the band structure in the form of Eq. 2.41, meaning,

$$\epsilon_{\boldsymbol{k}} \sim \gamma_{\boldsymbol{k}} t.$$

If strain is applied along the zig-zag direction, then by observation,[1] $\boldsymbol{\delta}_1$ and $\boldsymbol{\delta}_2$ will be larger than $\boldsymbol{\delta}_1$, and so the hopping amplitude between *NN* atoms connected by $\boldsymbol{\delta}_1$ will be different from that of atoms connected by $\boldsymbol{\delta}_1$ and $\boldsymbol{\delta}_2$. Remembering that each term in $\gamma_{\boldsymbol{k}}$ corresponded to a different *NN* atom, the band structure may be written

[1] See Fig. 1.1

as

$$\epsilon_{\boldsymbol{k}} \sim t' + te^{i\boldsymbol{k}\cdot\boldsymbol{a}_1} + te^{i\boldsymbol{k}\cdot\boldsymbol{a}_2},$$

where t' is the hopping amplitude between NN atoms connected by $\boldsymbol{\delta}_1$, and t are the other two hopping amplitudes. At the Dirac points, $\boldsymbol{D}$, $\epsilon_{\boldsymbol{k}} = 0$, so

$$t' + te^{i\boldsymbol{D}\cdot\boldsymbol{a}_1} + te^{i\boldsymbol{D}\cdot\boldsymbol{a}_2} = 0 \tag{5.1}$$

which has real and imaginary components. Since t' and t are real, the imaginary part of Eq. 5.1 is, applying the specific form of the lattice vectors $\boldsymbol{a}_i$ given by Eq. 1.1,

$$t\sin\left(\frac{\sqrt{3}a}{2}(D_x + \sqrt{3}D_y)\right) + t\sin\left(\frac{\sqrt{3}a}{2}(-D_x + \sqrt{3}D_y)\right) = 0. \tag{5.2}$$

This equation is satisfied when $D_y = 0$. Moving on to the real part of Eq. 5.1,

$$\begin{aligned}
&t' + t\cos\left(\frac{\sqrt{3}a}{2}(D_x + \sqrt{3}D_y)\right) + t\cos\left(\frac{\sqrt{3}a}{2}(-D_x + \sqrt{3}D_y)\right) = 0 \\
&t' + t\cos\left(\frac{\sqrt{3}a}{2}D_x\right) + t\cos\left(-\frac{\sqrt{3}a}{2}D_x\right) = 0 \\
&t' + 2t\cos\left(\frac{\sqrt{3}a}{2}D_x\right) = 0 \\
&D_x = \frac{2}{\sqrt{3}a}\arccos\left(-\frac{t'}{2t}\right).
\end{aligned} \tag{5.3}$$

Thus the position of the Dirac points depends on the ratio of hopping parameters $\frac{t'}{2t}$. As this ratio grows, the Dirac point moves closer to the origin, and as the ratio decreases it will move farther away. With strain along the zig-zag direction, $t' \geq t$, and so D_x will decrease. Considering that there are two inequivalent Dirac points located both D_x and $-D_x$, as zig-zag strain increases, these two points will move closer together, eventually meeting in the middle and merging into a new energy spectrum in a phenomena known self-evidently as Dirac point merging. This phenomena has

been noted several times before[6, 17], but after a brief overview of what kind of band structure these cones merge to form, the polarization charge density will be evaluated for this exotic form of graphene.[2]

5.1 Merged Band Structure

To begin, recall $\gamma_{\boldsymbol{k}}$ in its most general form,

$$\gamma_{\boldsymbol{k}} = \sum_{m,n} e^{i\boldsymbol{k}\cdot\boldsymbol{R}_{mn}},$$

where $\boldsymbol{R}_{mn}$ are arbitrary lattice vectors, given in their most generic form as a linear combination of the lattice vectors $\boldsymbol{a}_1$ and $\boldsymbol{a}_2$,

$$\boldsymbol{R}_{mn} = m\boldsymbol{a}_1 + n\boldsymbol{a}_2 \quad m, n \in \mathbb{Z}.$$

Once again imagine expanding $\gamma_{\boldsymbol{k}}$ near the Dirac point $\pm\boldsymbol{D}$, letting $\boldsymbol{k} = \pm\boldsymbol{D} + \boldsymbol{q}$, this time truncating after second-order in $\boldsymbol{q}$,

$$\gamma_{\boldsymbol{q}} = \sum_{m,n} e^{\pm i\boldsymbol{D}\cdot\boldsymbol{R}_{mn}} e^{i\boldsymbol{q}\cdot\boldsymbol{R}_{mn}},$$
$$\gamma_{\boldsymbol{q}} \approx \sum_{m,n} e^{\pm i\boldsymbol{D}\cdot\boldsymbol{R}_{mn}} + i\sum_{m,n} \boldsymbol{q}\cdot\boldsymbol{R}_{mn} e^{\pm i\boldsymbol{D}\cdot\boldsymbol{R}_{mn}} - \frac{1}{2}\sum_{m,n} (\boldsymbol{q}\cdot\boldsymbol{R}_{mn})^2 e^{\pm i\boldsymbol{D}\cdot\boldsymbol{R}_{mn}},$$

enforcing the condition that $\gamma_{\pm\boldsymbol{D}} = 0$,

$$\gamma_{\boldsymbol{q}} \approx i\sum_{m,n} \boldsymbol{q}\cdot\boldsymbol{R}_{mn} e^{\pm i\boldsymbol{D}\cdot\boldsymbol{R}_{mn}} - \frac{1}{2}\sum_{m,n} (\boldsymbol{q}\cdot\boldsymbol{R}_{mn})^2 e^{\pm i\boldsymbol{D}\cdot\boldsymbol{R}_{mn}}. \tag{5.4}$$

[2]It should be noted that straining graphene to the point of Dirac cone merger may be impossible, but such a system could be manufactured or there are other materials that may exhibit similar behavior. This will be mentioned in more detial later, but see [6, 17] for more.

Inequivalent Dirac points $\pm\boldsymbol{D}$ are, in unstrained graphene, connected by a reciprocal lattice vector $\boldsymbol{G}_{uv}$, given, like $\boldsymbol{R}_{mn}$, most generally as a linear combination of the reciprocal lattice vectors $\boldsymbol{b}_i$ given by Eq. 1.3,

$$\boldsymbol{G}_{uv} = u\boldsymbol{b}_1 + v\boldsymbol{a}_2 \quad u, v \in \mathbb{Z}.$$

As previously explained, when inequivalent Dirac points merge, they do so at the midpoint between them, that is at $\boldsymbol{G}_{uv}/2$. So when two Dirac points merge,

$$\gamma_{\boldsymbol{q}} \approx i\sum_{m,n} \boldsymbol{q}\cdot\boldsymbol{R}_{mn} e^{\pm\frac{1}{2}i\boldsymbol{G}_{uv}\cdot\boldsymbol{R}_{mn}} - \frac{1}{2}\sum_{m,n}(\boldsymbol{q}\cdot\boldsymbol{R}_{mn})^2 e^{\pm\frac{1}{2}i\boldsymbol{G}_{uv}\cdot\boldsymbol{R}_{mn}}$$

through a simple application of the vectors $\boldsymbol{a}_i$ and $\boldsymbol{b}_i$,

$$\boldsymbol{G}_{uv}\cdot\boldsymbol{R}_{mn} = 2\pi(um - vn).$$

Substituting into $\gamma_{\boldsymbol{q}}$,

$$\gamma_{\boldsymbol{q}} \approx i\sum_{m,n} \boldsymbol{q}\cdot\boldsymbol{R}_{mn} e^{\pm i\pi(um-vn)} - \frac{1}{2}\sum_{m,n}(\boldsymbol{q}\cdot\boldsymbol{R}_{mn})^2 e^{\pm i\pi(um-vn)}$$
$$\gamma_{\boldsymbol{q}} \approx i\sum_{m,n} \boldsymbol{q}\cdot\boldsymbol{R}_{mn} (-1)^{(um-vn)} - \frac{1}{2}\sum_{m,n}(\boldsymbol{q}\cdot\boldsymbol{R}_{mn})^2 (-1)^{(um-vn)}.$$

The first sum, due to the definition of $\boldsymbol{a}_1$ and $\boldsymbol{a}_2$, contains no information about the zig-zag direction, since the sum is in the net-armchair direction.[3] This is why expanding to second-order in $\boldsymbol{q}$ was necessary, because when the Dirac points merge, a first-order expansion in $\boldsymbol{q}$ no longer contains all the needed information about the

[3]The sum actually, when t_{mn} the anisotropic lattice parameter is included when the energy is evaluated from $\gamma_{\boldsymbol{q}}$, is equal to the Fermi velocity, v. This term has been omitted for now but will be reintroduced.

band structure. So,

$$\gamma_{\boldsymbol{q}} \approx -iq_y - \frac{1}{2}\sum_{m,n}(\boldsymbol{q}\cdot\boldsymbol{R}_{mn})^2(-1)^{(um-vn)}$$
$$\gamma_{\boldsymbol{q}} \approx -iq_y - \frac{1}{2}\sum_{m,n}(q_x^2R_{mn,x}^2 + q_y^2R_{mn,y}^2 + q_xq_yR_{mn,x}R_{mn,y})(-1)^{(um-vn)},$$

since $q_y^2 \ll q_y$, and $q_yq_x \ll q_y$, terms involving these two factors can be neglected,

$$\gamma_{\boldsymbol{q}} \approx -iq_y - \frac{1}{2}q_x^2\sum_{m,n}R_{mn,x}^2(-1)^{(um-vn)}.$$

Now, as explained, for Dirac points to merge, the hopping parameter t must also depend on direction, so $t = t_{mn}$, and once again referencing Eq. 2.41,

$$\begin{aligned}
\epsilon_{\boldsymbol{q}} &= \pm|\gamma_{\boldsymbol{q}}t_{mn}| \\
&= \pm\sqrt{|\gamma_{\boldsymbol{q}}t_{mn}|^2} \\
&= \pm\sqrt{\left(-iq_yv - \frac{1}{2}q_x^2\sum_{m,n}t_{mn}R_{mn,x}^2(-1)^{(um-vn)}\right)\left(iq_yv - \frac{1}{2}q_x^2\sum_{m,n}t_{mn}R_{mn,x}^2(-1)^{(um-vn)}\right)} \\
&= \pm\sqrt{\left(\frac{1}{2}q_x^2\sum_{m,n}t_{mn}R_{mn,x}^2(-1)^{(um-vn)}\right)^2 + q_y^2v^2} \\
\epsilon_{\boldsymbol{q}} &= \pm\sqrt{\left(\frac{q_x^2}{2m^*}\right)^2 + q_y^2v^2}, \qquad (5.5)
\end{aligned}$$

where the effective mass m^* has been defined as

$$\frac{1}{m^*} = \sum_{m,n}t_{mn}R_{mn,x}^2(-1)^{(um-vn)}.$$

Equation 5.5 is very different from the familiar Dirac cone of graphene. The merged band structure has the very notable property of remaining linear along the armchair direction, but becoming quadratic along the zig-zag, the direction of strain in this

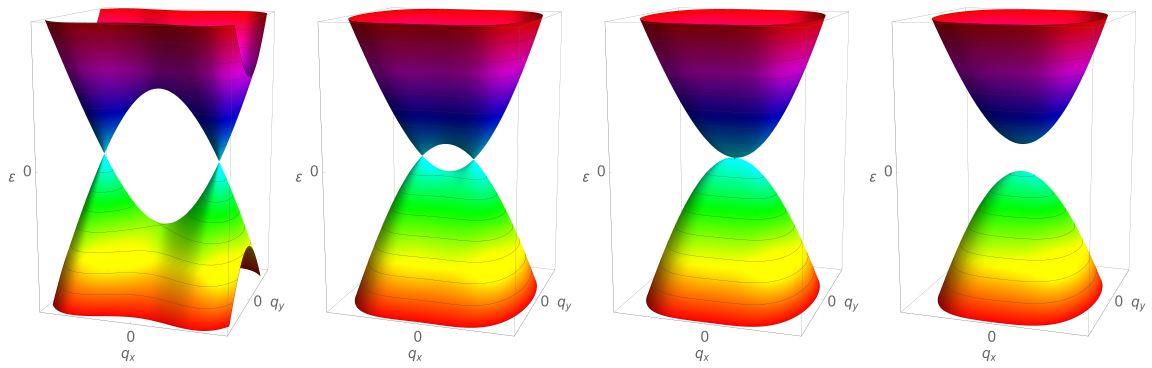

(a) (b) (c) (d)

Figure 5.1: The process of Dirac cone merging. Panel (a) shows $\Delta < 0$, two separate cones, moving to panel (b), Δ approaches zero and the cones have begun to merge. Panel (c) shows $\Delta = 0$, the fully merged, but still ungapped spectrum from Eq. 5.5. Finally panel (d) is the insulating band structure at some $\Delta > 0$.

case.[4] It was mentioned that $\gamma_{\pm \boldsymbol{D}}$ was defined to be zero, but this is not exactly the case. In actuality, since the energy actually goes as $t_{mn}\gamma_{\pm \boldsymbol{D}}$, and the hopping parameter is no longer isotropic, the energy at the Dirac point may not actually be zero but instead some finite energy Δ. Including this finite energy at the Dirac point, Eq. 5.5 must be modified,

$$\epsilon_{\boldsymbol{q}} = \pm\sqrt{\left(\Delta + \frac{q_x^2}{2m^*}\right)^2 + q_y^2 v^2}. \tag{5.6}$$

Variation of this parameter Δ can showcase the entire transition. When $\Delta < 0$ the structure appears as two Dirac cones separated by some distance. As Δ increases, approaching zero, the energy at $\boldsymbol{q} = 0$ also approaches zero, which appears as the cones moving closer together and merging until at $\Delta = 0$, the cones completely merge, and the energy structure returns to the form of Eq. 5.5. If Δ continues to increase such that it becomes greater than zero, a gap can actually form, meaning that graphene transitions from a metallic phase to an insulating one. The gradual increase of Δ is shown in the four panels of Fig. 5.1.

[4] In principle this can also be achieved by compressive "strain" in the armchair direction[17].

This is dramatically different from typical graphene, and indeed, strain of this magnitude may not be possible. However that does not mean this band structure is nonphysical, it could still be possible by an artificial lattice of cold atoms for example, arranged in a periodic potential in such a way that mimics the structure and electronic properties of graphene[6, 17]. Really then, it should be said that this band structure applies not to graphene, but to graphene-based systems. To gain any kind of understanding of such a system, the electronic properties must be investigated, beginning with screening response to an impurity.

5.2 Polarization and Charge Density for Merged Dirac Cones

The specific case of the insulating graphene will not be considered here, instead the polarization and charge density will be evaluated for the ungapped, merged energy spectrum shown in Fig. 5.1 (c). The procedure for this case is very similar to the previous case: calculate the polarization from the basic formula (Eq. 3.3), including the wavefunction overlap (Eq. 3.16), then integrate Eq. 4.1 to find the charge density around a Coulomb impurity. The procedure is the same with one very important exception: unlike the first case, there will be no finite chemical potential, so $\mu = 0$. An initial consequence of this change is that there is no sum over inter and intraband transitions since there are only interband transitions when $\mu = 0$. Instead the polarization is a fairly straightforward, but tedious calculation, and so will not be shown in great detail. Suffice to say that beginning with the general formula,

$$\Pi(\boldsymbol{q}) = -g_s g_v \int_0^\infty \frac{d^2k}{4\pi^2} \frac{1}{\epsilon_{\boldsymbol{k}} + \epsilon_{\boldsymbol{k}+\boldsymbol{q}}} \left[\frac{\epsilon_{\boldsymbol{k},x}\epsilon_{\boldsymbol{k}+\boldsymbol{q},x} + \epsilon_{\boldsymbol{k},y}\epsilon_{\boldsymbol{k}+\boldsymbol{q},y}}{\epsilon_{\boldsymbol{k}}\epsilon_{\boldsymbol{k}+\boldsymbol{q}}} \right], \tag{5.7}$$

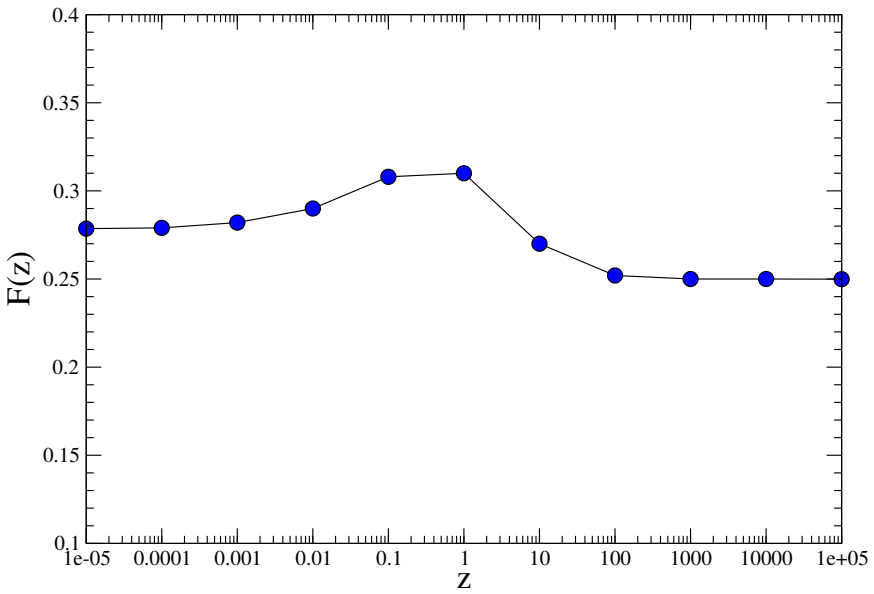

Figure 5.2: Log plot of the function $F(z)$. Variation in F is very minor: $F \approx 0.28$ at very small Z, and $F \approx 0.25$ at very large Z. The maximum value is a little greater than 0.3. Judging by the minor variation, the function $F(z)$ can effectively be considered a constant, F.

apply Eq. 5.5 to Eq. 5.2, and make the following change of variables,

$$Q_x = \left(1 + \frac{1}{z}\right)^{\frac{-1}{4}} \qquad Q_y = (1+z)^{\frac{-1}{2}}$$
$$p_x = \frac{k_x}{\sqrt{q}} \qquad p_y = \frac{k_y}{q},$$

where

$$z = \frac{q_x^2}{q_y^2 v^2 (2m^*)^2}.$$

Using these redefinitions Eq. can be reduced after a fair amount of algebra to be

$$\Pi(\boldsymbol{q}) = -g_s g_v \frac{F(z)}{4} \frac{\sqrt{2m^*}}{v} \left(\left(\frac{q_x^2}{2m^*} \right)^2 + q_y^2 v^2 \right)^{\frac{1}{4}}. \tag{5.8}$$

The function $F(z)$ is actually the remaining integral for the evaluation of $\Pi(\boldsymbol{q})$,

$$F(z) = \int \frac{d^2p}{\pi^2} \frac{1 - \frac{p_x^2(p_x+Q_x)^2 + p_y(p_y+Q_y)}{\sqrt{p_x^4+p_y^2}\sqrt{(p_x+Q_x)^4+(p_y+Q_y)^2}}}{\sqrt{p_x^4+p_y^2} + \sqrt{(p_x+Q_x)^4+(p_y+Q_y)^2}},$$

which as complicated as it may look actually can be numerically evaluated and is essentially equal to a constant, see the caption of Fig. 5.2 for more details. With a closed form for the polarization, consider, like before, a Coulomb impurity with the potential

$$V(\boldsymbol{q}) = \frac{2\pi e^2}{q},$$

and substitute into Eq. 4.1,

$$n(\boldsymbol{r}) = -Z g_s g_v \frac{F}{4}\frac{1}{v}\int_0^\infty \frac{d^2q}{4\pi^2} \frac{e^{i\boldsymbol{q}\cdot\boldsymbol{r}}\sqrt{2m^*}\left(\left(\frac{q_x^2}{2m^*}\right)^2 + q_y^2v^2\right)^{\frac{1}{4}}\frac{2\pi e^2}{q}}{1 + g_s g_v \frac{F}{4}\frac{\sqrt{2m^*}}{v}\left(\left(\frac{q_x^2}{2m^*}\right)^2 + q_y^2v^2\right)^{\frac{1}{4}}\frac{2\pi e^2}{q}}$$

let $\kappa = \frac{g_s g_v F}{4}$,

$$n(\boldsymbol{r}) = -Z\kappa\frac{2\pi e^2}{v}\int_0^\infty \frac{d^2q}{4\pi^2}\frac{1}{q}\frac{e^{i\boldsymbol{q}\cdot\boldsymbol{r}}\left(q_x^4 + (2m^*v)^2q_y^2\right)^{\frac{1}{4}}}{1 + \kappa\frac{2\pi e^2}{qv}\left(q_x^4 + (2m^*v)^2q_y^2\right)^{\frac{1}{4}}}.$$

In the denominator there is a factor of $\frac{e^2}{v}$ multiplying the e-e interaction term in the integral. This is of the same form as the value α in the previous case, but it is important to note that this is not the same α since the Fermi velocity is different in this case. Also, the rest of the constants, κ and 2π will be included in the definition for this new α. While knowing that the value is different from the previous case, this factor still plays the same role: that of an effective e-e interaction term. This same term, like in the finite chemical potential case, also acts as an overall prefactor to the integration. So, substitute

$$\alpha = \frac{2\pi\kappa e^2}{v}, \tag{5.9}$$

resulting in

$$n(\boldsymbol{r}) = -Z\alpha \int_0^\infty \frac{d^2q}{4\pi^2}\frac{1}{q}\frac{e^{i\boldsymbol{q}\cdot\boldsymbol{r}}\left(q_x^4 + (2m^*v)^2 q_y^2\right)^{\frac{1}{4}}}{1+\frac{\alpha}{q}\left(q_x^4 + (2m^*v)^2 q_y^2\right)^{\frac{1}{4}}}.$$

Finally, define $p = 2m^*v$ as the momentum in the system,

$$n(\boldsymbol{r}) = -Z\alpha \int_0^\infty \frac{d^2q}{4\pi^2}\frac{1}{q}\frac{e^{i\boldsymbol{q}\cdot\boldsymbol{r}}\left(q_x^4 + p^2 q_y^2\right)^{\frac{1}{4}}}{1+\frac{\alpha}{q}\left(q_x^4 + p^2 q_y^2\right)^{\frac{1}{4}}}, \tag{5.10}$$

and this integral becomes fully reduced. All that is left are integration variables and constants that characterize the system: momentum, e-e interaction strength, and position around the impurity site. This can be numerically evaluated directly, but the problem is that with Eq. 5.10 as it is there is no direct information that can be gleaned about the behavior of the screening response. The chemical potential is zero, so there is no reason to expect oscillations in the form of Friedel, or any screening distribution whatsoever. Part of the problem is that all of the dimensionality of the charge distribution is in the integral. By recasting Eq. 5.10 in dimensionless quantities it may be possible to at least gain some understanding of how the charge density depends on distance. Start by isolating the distance and the angular dependence by converting to polar coordinates,

$$n(\boldsymbol{r}) = -Z\alpha \int_0^\infty \int_0^{2\pi} \frac{dqd\phi}{4\pi^2}\frac{e^{iqr\cos(\phi-\varphi)}\left(q^4\cos^4\phi + p^2q^2\sin^2\phi\right)^{\frac{1}{4}}}{1+\frac{\alpha}{q}\left(q^4\cos^4\phi + p^2q^2\sin^2\phi\right)^{\frac{1}{4}}}, \tag{5.11}$$

where φ is the real-space angle above the zig-zag direction, and ϕ is the momentum-space angle. Now the factor qr in the exponential is dimensionless, so make the

substitution $x = qr$,

$$
\begin{aligned}
n(\boldsymbol{r}) &= -Z\alpha \int_0^\infty \int_0^{2\pi} \frac{dxd\phi}{4\pi^2} \frac{1}{r} \frac{e^{ix\cos(\phi-\varphi)} \left(\frac{x}{r}^4 \cos^4\phi + p^2 \frac{x}{r}^2 \sin^2\phi\right)^{\frac{1}{4}}}{1 + \frac{\alpha r}{x} \left(\frac{x}{r}^4 \cos^4\phi + p^2 \frac{x}{r}^2 \sin^2\phi\right)^{\frac{1}{4}}} \\
&= -Z\alpha \int_0^\infty \int_0^{2\pi} \frac{dxd\phi}{4\pi^2} \frac{1}{r} \frac{e^{ix\cos(\phi-\varphi)} \sqrt{\frac{p}{r}} \left(\frac{x^4}{p^2r^2} \cos^4\phi + x^2 \sin^2\phi\right)^{\frac{1}{4}}}{1 + \frac{\alpha r}{x} \sqrt{\frac{p}{r}} \left(\frac{x^4}{p^2r^2} \cos^4\phi + x^2 \sin^2\phi\right)^{\frac{1}{4}}} \\
&= -Z\alpha \int_0^\infty \int_0^{2\pi} \frac{dxd\phi}{4\pi^2} \frac{\sqrt{p}}{r^{\frac{3}{2}}} \frac{e^{ix\cos(\phi-\varphi)} \left(\frac{x^4}{p^2r^2} \cos^4\phi + x^2 \sin^2\phi\right)^{\frac{1}{4}}}{1 + \frac{\alpha}{x} \sqrt{pr} \left(\frac{x^4}{p^2r^2} \cos^4\phi + x^2 \sin^2\phi\right)^{\frac{1}{4}}} \\
n(\boldsymbol{r}) &= -Z\alpha \int_0^\infty \int_0^{2\pi} \frac{dxd\phi}{4\pi^2} \frac{p^2}{(pr)^{\frac{3}{2}}} \frac{e^{ix\cos(\phi-\varphi)} \left(\frac{x^4}{p^2r^2} \cos^4\phi + x^2 \sin^2\phi\right)^{\frac{1}{4}}}{1 + \frac{\alpha}{x} \sqrt{pr} \left(\frac{x^4}{p^2r^2} \cos^4\phi + x^2 \sin^2\phi\right)^{\frac{1}{4}}}.
\end{aligned}
$$

The momentum p has dimension of inverse length, so the product pr is also dimensionless. Call this value R, and define $p = L^{-1}$ as the characteristic length of the system and,

$$
n(R,\varphi) = -Z\alpha \frac{1}{L^2 R^{\frac{3}{2}}} \int_0^\infty \int_0^{2\pi} \frac{dxd\phi}{4\pi^2} \frac{e^{ix\cos(\phi-\varphi)} \left(\frac{x^4}{R^2} \cos^4\phi + x^2 \sin^2\phi\right)^{\frac{1}{4}}}{1 + \frac{\alpha}{x} \sqrt{R} \left(\frac{x^4}{R^2} \cos^4\phi + x^2 \sin^2\phi\right)^{\frac{1}{4}}}. \tag{5.12}
$$

Unfortunatley, Eq. 5.12 cannot be simplified any further, but significant progress has been made. By converting to dimensionless variables, all dimension of distance has been removed from the integrand and now resides in the characteristic length scale L. Charge density in a two-dimensional lattice should have dimension of inverse square distance, as Eq. 5.12 does. Also, the angular function and the radial function of the charge distribution has not been entirely decoupled, but some overall decay by $R^{-\frac{3}{2}}$ has appeared outside the integral. Even at zero chemical potential, there is indication that the polarization charge density may still follow a power-law decay with distance from an impurity charge.

To verify the existence of a power-law decay in the charge density, consider

not the explicit radial dependence of n, which appears to be highly coupled to the angular dependence, but instead consider the angularly-averaged asymptotic distance dependence. That is, how does the angularly-averaged charge density depend on distance at large values of R, which correspond to small q? Small values of q mean that $x^4 \ll x^2$, and so the sine terms in the integrand dominate over the cosine terms, so in the small-q limit,

$$n(R,\varphi) = -Z\alpha \frac{1}{L^2 R^{\frac{3}{2}}} \int_0^\infty \int_0^{2\pi} \frac{dx d\phi}{4\pi^2} \frac{e^{ix\cos(\phi-\varphi)}\sqrt{x\sin\phi}}{1+\frac{\alpha}{x}\sqrt{R}\sqrt{x\sin\phi}}, \tag{5.13}$$

the integral over φ can be evaluated from tables,

$$\begin{aligned} \bar{n}(R) &= \int_0^{2\pi} \frac{d\varphi}{2\pi} n(R,\varphi) \\ \bar{n}(R) &= -Z\alpha \frac{2}{L^2 R^{\frac{3}{2}}} \int_0^\infty \int_0^{\pi} \frac{dx d\phi}{(2\pi)^2} \frac{J_0(x)\sqrt{x}\sqrt{\sin\phi}}{1+\alpha\sqrt{\frac{R}{x}}\sqrt{\sin\phi}} \end{aligned} \tag{5.14}$$

this integral can be evaluated exactly using Mathematica by first expanding around large values of $\alpha\sqrt{\frac{R}{x}}$ and performing the integral over φ and then substitute into Eq. 5.14, and find that

$$L^2 \frac{\bar{n}(R)}{C} = \frac{5.48}{\alpha^2 R^{\frac{5}{2}}} - \frac{8\ln(\alpha\sqrt{R})}{\alpha^3 R^3} + O(R^{-\frac{7}{2}}), \quad \alpha\sqrt{R} \to \infty \tag{5.15}$$

where C is the set of constants $\frac{-2Z\alpha}{(2\pi)^2}$. At very large distances the angularly-averaged charge density decays as $R^{-\frac{5}{2}}$. Figure 5.3 shows a log-log plot of Eq. 5.15, this plot shows the deviation from the pure $R^{-\frac{5}{2}}$ decay at finite values of R. The deviations from an $R^{-\frac{5}{2}}$ decay diminish as R becomes large, and so this long-range tail seems valid. This is a very interesting result because in graphene, at zero chemical potential, one would not expect to observe long-range charge distributions, and yet such long-range behavior can be analytically extracted at zero chemical potential. Apart from

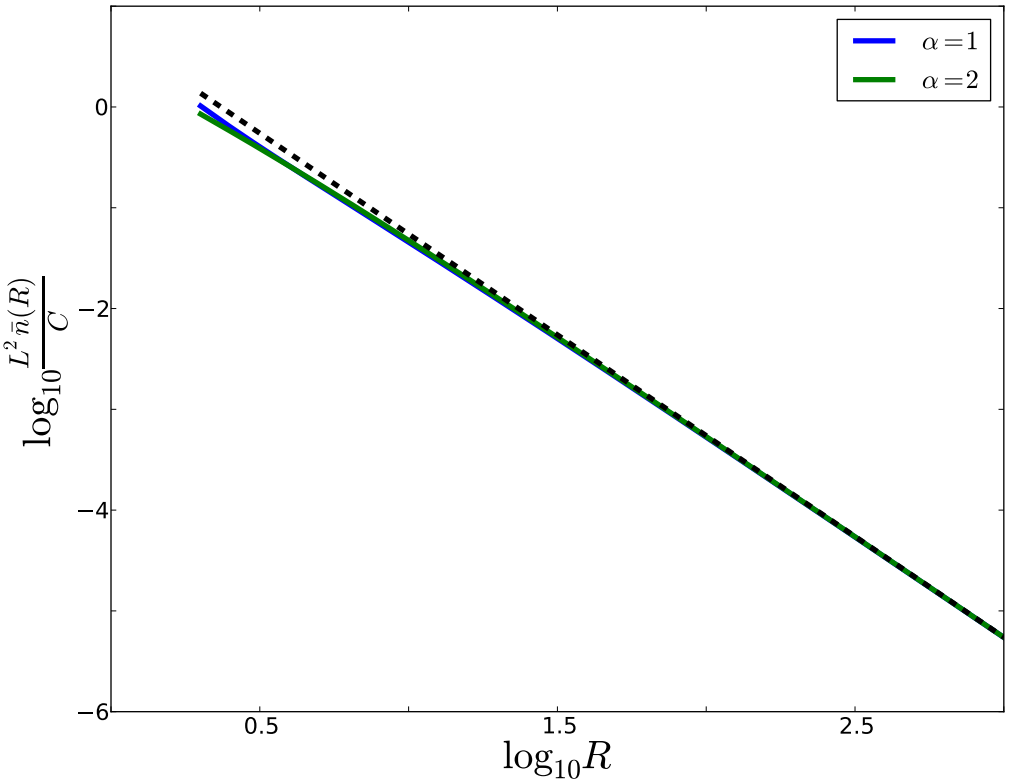

Figure 5.3: Log-log plot of Eq. 5.15 at two values of α. The black dotted line is a plot of the "pure" $R^{-\frac{5}{2}}$ given by the first term in Eq. 5.15. The green and blue plots include higher order terms and show some of the deviation from the $R^{-\frac{5}{2}}$ decay at smaller values of R. As R becomes large ($R \sim 1000$), the density approaches the "pure" $R^{-\frac{5}{2}}$ behavior.

this analytic insight, the only avenue for analysis of Eq. 5.12 is numerical evaluation. For the purposes of the evaluation, the density $n(R, \varphi)$ will be rescaled as

$$\widetilde{n}(R, \varphi) = \frac{n(R, \varphi)}{Z\alpha}. \tag{5.16}$$

Here there is no strain parameter to vary, rather the challenge is simply understanding the form of the charge distribution. With the average radial behavior at large distances understood, what remains is the angular behavior. Consider a distance at which the $R^{-\frac{5}{2}}$ has largely settled, and numerically evaluate the density over

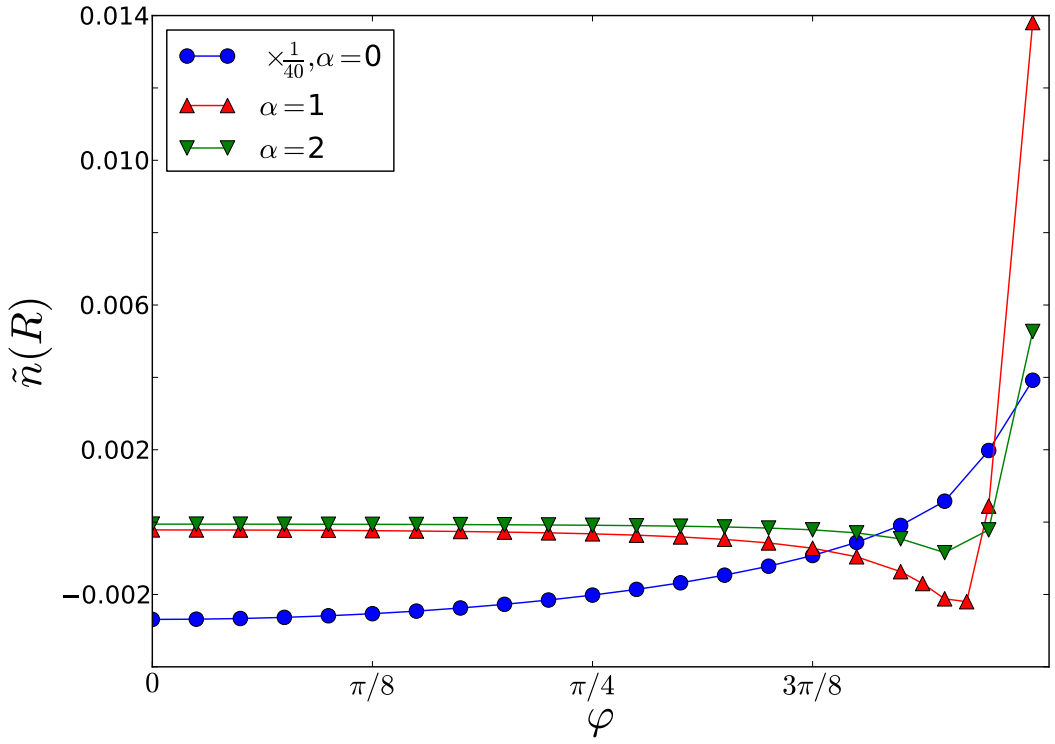

Figure 5.4: Plot showing the angular dependence of the polarization charge density at a distance $R = 1000$. This is an asymptotic distance scale, where the deviations from the $R^{-\frac{5}{2}}$ decay have begun to diminish. Three different values of α are plotted, and each shows similar behavior, most notably the appearance of both screening and anti-screening regions.

a range of angles. It turns out that for any distance the angular behavior is periodic over intervals of $\frac{\pi}{2}$, so each angular plot will be over the domain $\varphi = \left[0, \frac{\pi}{4}\right]$. First, $R = 1000$ is shown in Fig. 5.4.

Three values of α are plotted in Fig. 5.4, but the differences between them are relatively minor. The most important facet of note in the plot is that the charge density crosses zero. In typical screening there is no reason for the induced charge density to be positive in response to a positive impurity charge. This "anti-screening" effect is very unusual, and in this case dramatic. At $R = 1000$ the density, for some finite α, is close to zero for most of the region around the impurity. Close to $\varphi = \frac{\pi}{2}$ a the density drops gradually below zero before very sharply changing sign becoming

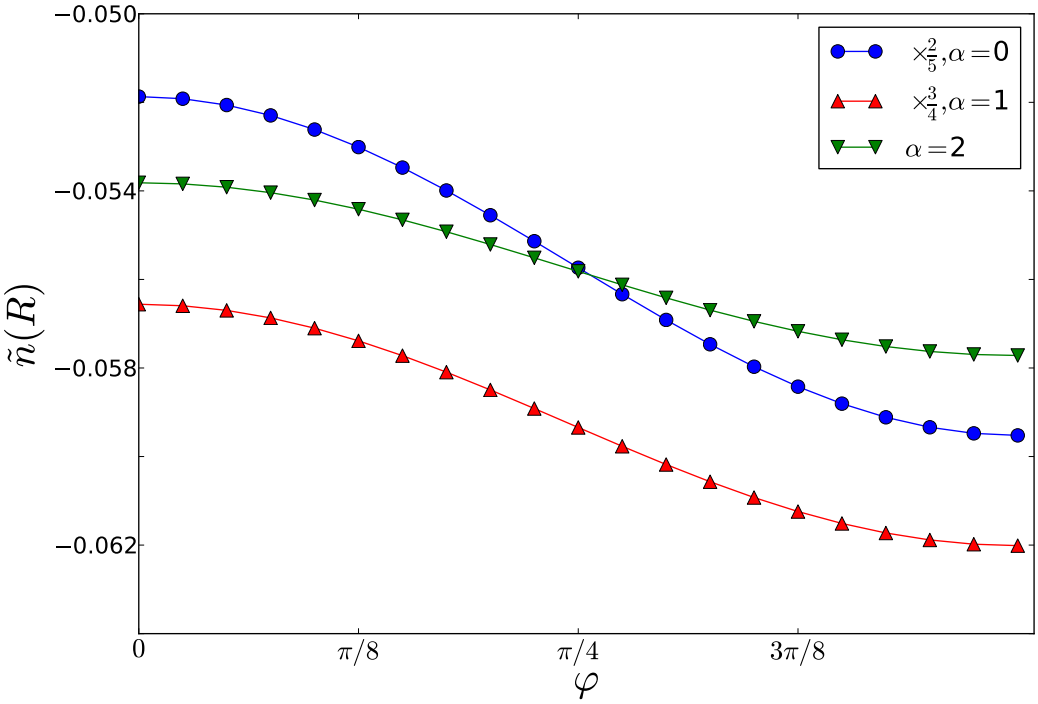

Figure 5.5: Plot showing the angular dependence of the polarization charge density at a distance $R = 0.1$. In contrast to the previous figure, this region is very close to the impurity charge. The behavior for all three values of α are very similar. There are no anti-screening effects observed at this distance, and the anisotropy of the lattice is well represented with the the density gradually altering between maximally and minimally negative along the zig-zag and armchair respectively.

maximally positive at $\varphi = \frac{\pi}{2}$ (the armchair direction), appearing to actually diverge along this direction. The plot does not actually include a point at $\varphi = \frac{\pi}{2}$ for this reason: the more precision is applied to the numerical integration the greater the peak at $\frac{\pi}{2}$ becomes, and so the value of the density along that direction appears to be undefined at these distances. Since protons do not move within the lattice, an infinite positive charge density implies a complete absence of electrons in this region.

In stark constrast to Fig. 5.4, the density very near to the impurity charge, $R = 0.1$ is shown in Fig. 5.5. At distances close to the impurity, the induced charge density behaves in a way almost completely counter to large distances. First of all there are no anti-screening effects at small distances, the density, for all three values

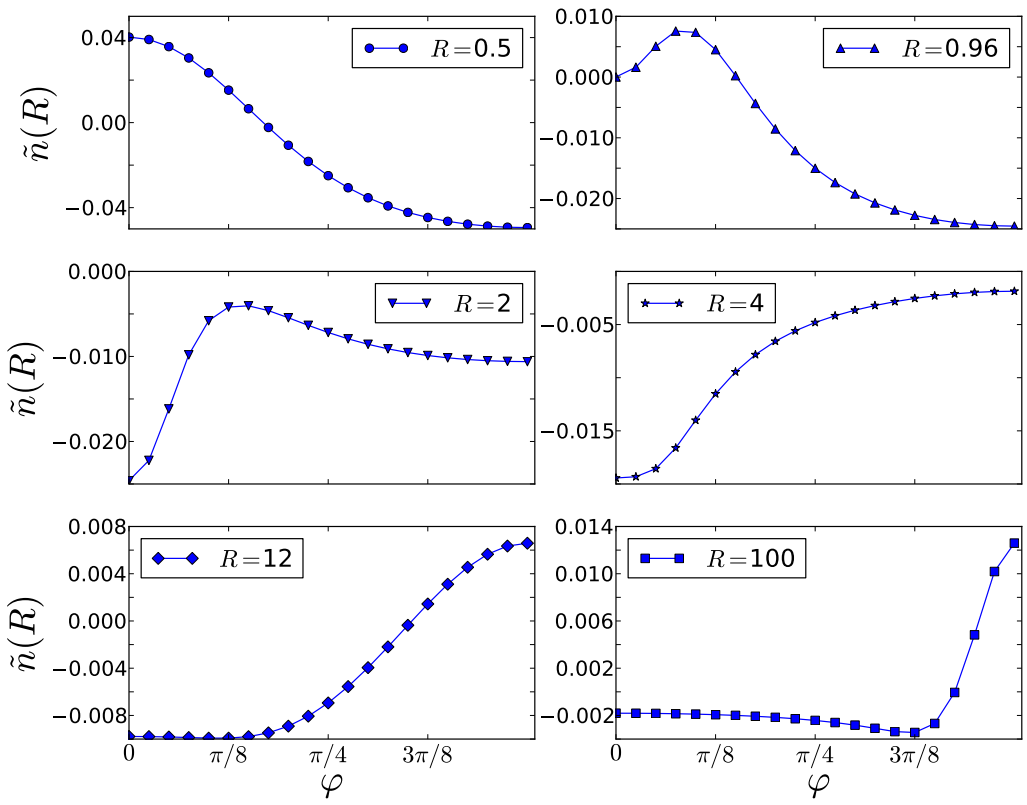

Figure 5.6: Six plots showing the six distance regimes each exhibiting distinct angular behaviors. Distances increase from top-left ($R = 0.5$), to bottom-right ($R = 100$), and between these two distances, the charge density transitions completely from the behavior observed at very small distances, $R = 0.1$ and very large distances $R = 1000$.

of α, are negative for all angles around the impurity. There are no singularities, or sudden shifts in the density, but rather the density is completely sinusoidal. At angles of 0 and π the density is closest to zero, while at $\frac{\pi}{2}$ and $\frac{3\pi}{2}$ the density becomes maximally negative. Conceptually this is expected, along the direction of strain there should be less electron motility and so the density of electrons is expectedly lower. With two such dramatically different angular distributions at small and large distances from the impurity, the next logical step is to investigate the transition between the two; the angular densities at intermediate distances.

There is no simple or systematic way to characterize how the density tran-

sitions between the behavior at $R = 0.1$ and at $R = 1000$. The radial and angular dependence of the charge density is not only difficult to decouple, but they appear to be so highly coupled that they cannot be separated. So the angular dependence was split into different distance regimes over which the general behavior remains unchanged. These behaviors range from that seen in Fig. 5.5 to that in 5.4, and the transition is not easily described. In total, six distinct distance regimes were identified, each shown in Fig. 5.6.

The top-left plot in Fig. 5.6 is for $R = 0.5$. This is still relatively close to the impurity, and the basic sinusoidal behavior is consistent with the $R = 0.1$ plot: the lower density of electrons is along the direction of strain while the greater density is along the perpendicular. At $R = 0.5$ there is already anti-screening effects in the distribution. Along the direction of strain, the charge density is now maximally *positive* rather than minimally negative. At $R = 0.96$ the sinusoidal behavior no longer exists. At this distance, the charge density at $\varphi = 0$ is equal to zero, which is significant, because beyond this distance the density at $\varphi = 0$ becomes negative. At a little less than $\frac{\pi}{8}$ a local maximum has appeared that did not exist at smaller distances. The behavior at angles beyond $\frac{\pi}{8}$ remains, aside from amplitude, essentially unchanged.

As distances increase to $R = 2$, the density at $\varphi = 0$ becomes increasingly negative, while the density at $\varphi = \frac{\pi}{2}$ decreases and the maxima at $\frac{\pi}{8}$ diminishes, and is now the only region of anti-screening in the distribution. At $R = 4$, the maxima near $\frac{\pi}{8}$ has vanished, and the maxima instead appears at $\frac{\pi}{2}$. The distribution is similar to the sinusoidal behavior at smaller distances, but with a phase shift of $\frac{\pi}{2}$: the maximally negative distribution is at $\varphi = 0$, and the minimally negative distribution is at $\frac{\pi}{2}$, there are no other extrema in the charge distribution. Significantly, within this distance regime the distribution has no anti-screening effects. At $R = 12$ the overall density has decreased, and $\frac{\pi}{2}$ is now a region of strong anti-screening. Also, while difficult to discern in Fig. 5.6, there is a local minima near $\frac{\pi}{8}$ at $R = 12$. Finally, at

$R = 100$ the angular distribution exhibits all of the same characteristics as $R = 1000$, so the transition of angular dependences is complete by $R = 100$.

In the case of extreme strain to the point of Dirac cone merger, the unique resultant energy spectrum yields a highly exotic charge distribution even at zero chemical potential. Normally, electrons in graphene cannot polarize at zero chemical potential, but when the lattice is deformed until the Dirac points merge, remarkably, long-range charge densities unrelated to Friedel-type physics are observed. Not only that, but the angular charge distributions, which are vary dramatically depending on distance, show regions of both screening and anti-screening. It should be noted that the total induced charge density still remains equal to the impurity charge that is being screened, and thus still satisfies the basic requirements of screening in metals.

Chapter 6

Conclusion

Graphene is one of the most remarkable materials ever known, and the more thoroughly its properties are known the more varied possible applications may become. Understanding any material truly begins by understanding how electrons behave within it, and a common way to probe that behavior is to observe the charge density response to a Coulomb impurity: a phenomenon known as screening. The polarization charge density of unmodified graphene has been well documented, but in any practical applications a piece of graphene will most likely be subject to mechanical strain. The polarization charge density for two types of uniaxial strain were thus studied: relatively weak strain (up to about 25%) along the armchair direction at finite chemical potential, and extreme strain along the zig-zag resulting in a Dirac cone merger.

In the first case, strain along the armchair direction resulted in changes to both the amplitude and frequency of the Friedel oscillations observed as a result of the finite chemical potential. In the direction of strain both the amplitude and period of oscillations dropped, as did the overall magnitude of the induced density. Since the lattice sites are more widely spaced under strain, the electrons cannot move as easily along the direction of strain, so this result was not unexpected. The more remarkable

result is that along the zig-zag direction (perpendicular to strain) the period does not change, but the amplitude of the oscillations increase compared to unstrained graphene. What makes this interesting is that, along the zig-zag direction, the lattice spacing hardly changes, and yet the charge density in response to an impurity charge does.

In the latter case, strain along the zig-zag shifts the locations of Dirac points. If shifted enough, eventually two inequivalent Dirac points will merge and the result is a new energy spectrum that remains linear along the armchair direction, but the structure in the zig-zag becomes quadratic with momentum. The resultant screening response produces long range charge distributions in spite of the chemical potential being zero; this result is very interesting since normal graphene, with a linear band structure in all directions, requires some finite chemical potential to polarize. The long-range radial behavior was shown to decay as $R^{-\frac{5}{2}}$, and the angular distribution was highly coupled to the radial. At various distance regimes different angular distributions were observed, many with both screening and anti-screening regions. Strain of this magnitude along the zig-zag is impossible with graphene, but this Dirac cone merger has been observed in several graphene-like systems.

These results would be very important to anyone studying or tying to apply graphene and graphene-like systems. Many applications of graphene and other two-dimensional materials are as ultra-thin conductors, and mechanical strain would be a natural consequence of physical applications. Understanding the electrical properties of graphene under strain is of critical importance to creating new technologies with graphene. The electrical properties of graphene can be studied under a variety of other conditions: screening response with edge effects, a substrate like Boron-Nitride, bilayer graphene, and magnetic field response to name a few. Graphene has been heavily studied over the last twelve years, and yet the potential for new understanding of this remarkable material is still very high.

Bibliography

[1] P. R. Wallace. The band theory of graphite. *Physical Review*, 71(9):622–634, 1947.

[2] K. S. Novoselov, A. K. Geim, S. V. Morozov, D. Jiang, Y. Zhang, S. V. Dubonos, I. V. Grigorieva, and A. A. Firsov. Electric field effect in atomically thin carbon films. *Science*, 306(5696):666–669, 2004.

[3] Class for Physics of the Royal Swedish Academy of Science. Scientific background on the Nobel prize in physics: Graphene. 2010.

[4] Linus Pauling and G. W. Wheland. The nature of the chemical bond v. the quantum-mechanical calculation of the resonance energy of benzene and naphthalene and the hydrocarbon free radicals. *American Journal of Chemical Physics*, 1:362, March 1933.

[5] Valeri N. Kotov, Bruno Uchoa, Vitor M. Pereira, F. Guinea, and A. H. Castro Neto. Electron-electron interactions in graphene: Current status and perspectives. *Reviews of Modern Physics*, 84:1067, 2012.

[6] G. Montambaux, F. Piéchon, J.-N. Fuchs, and M. O. Goerbig. A universal hamiltonian for motion and merging of Dirac points in a two-dimensional crystal. *European Physical Journal B*, 72:509–520, November 2009.

[7] Tsuneya Ando. Screening effect and impurity scattering in monolayer graphene. *Journal of the Phyical Society of Japan*, 75(7):074716, July 2006.

[8] A. H. Castro Neto, F. Guinea, N. M. R. Peres, K. S. Novoselov, and A. K. Geim. The electronic properties of graphene. *Reviews of Modern Physics*, 81(1):109–162, 2009.

[9] Mark O. Goerbig and Gilles Montambaux. Dirac fermions in condensed matter and beyond. *Séminaire Poincaré*, 10 2014.

[10] Charles Kittel. *Introduction to Solid State Physics*. John Wiley and Sons, 8th edition, 2005.

[11] Neil Ashcroft and David Mermin. *Solid State Physics*. W. B. Saunders Company, 1976.

[12] B. Wunsch, T. Stauber, F. Sols, and F. Guinea. Dynamical polarization of graphene at finite doping. *New J. Phys.*, 8:318, 2006.

[13] A. A. Shylau, S. M. Badalyan, F. M. Peeters, and A. P. Jauho. Electron polarization function and plasmons in metallic armchair graphene nanoribbons. *Phys. Rev. B 91, 205444, 29 May 2015*, 01 2015.

[14] K. Kanisawa, M. J. Butcher, H. Yamaguchi, and Y. Hirayama. Imaging of friedel oscillation patterns of two-dimensionally accumulated electrons at epitaxially grown inas(111) a surfaces. *Physical Review Letters*, 86(15):3384–3387, 2001.

[15] K. F. Riley, M. P. Hobson, and S. J. Bence. *Mathematical Methods for Physics and Engineering*. Cambridge University Press, 3rd edition, 2014.

[16] Seon-Myeong Choi, Seung-Hoon Jhi, and Young-Woo Son. Effects of strain on electronic properties of graphene. *Phys. Rev. B*, 81:081407(R), 2010.

[17] J. Feilhauer, W. Apel, and L. Schweitzer. Merging of the Dirac points in electronic artificial graphene. *Phys. Rev. B*, 92:245424, 2015.